

# **A Self-Sufficient RFID Sensor Tag based on Optically Transparent Antenna and Analog Front-End for the Integration in Metal Components**

Von der Fakultät für Elektrotechnik und Informatik  
der Gottfried Wilhelm Leibniz Universität Hannover  
zur Erlangung des akademischen Grades

Doktor-Ingenieur  
(abgekürzt: Dr.-Ing.)

genehmigte Dissertation

von Herrn  
Dipl.-Ing. Quang Huy Dao  
geboren am 27. November 1984  
in Thai Nguyen, Vietnam

1. Referent:

apl. Prof. Dr.-Ing. Bernd Geck

2. Referent:

Prof. Dr.-Ing. Ludger Overmeyer

Vorsitzender der Prüfungskommission:

Prof. Dr.-Ing. Holger Blume

Tag der Promotion:

13.07.2021

# Danksagung

Diese Dissertation entstand während meiner Tätigkeit als wissenschaftlicher Mitarbeiter am Institut für Hochfrequenztechnik und Funksysteme der Leibniz Universität Hannover. Ohne die Unterstützung von vielen Personen wäre diese Arbeit nicht möglich gewesen.

Mein besonderer Dank gilt apl. Prof. Dr.-Ing. Bernd Geck dafür, dass er mir die Möglichkeit zur Promotion gegeben hat und mein Doktorvater war. Die zahlreichen Diskussionen, wertvollen Rückmeldungen und Ratschläge haben mir bei meiner Forschung enorm geholfen.

Ich möchte mich auch bei Prof. Dr.-Ing. Ludger Overmeyer für seine Tätigkeit als Zweitgutachter und bei Prof. Dr.-Ing. Holger Blume für die Übernahme des Prüfungsvorsitzes bedanken. Zudem danke ich Prof. Dr.-Ing. Dirk Manteuffel für seine Unterstützung während der Endphase des Projektes.

Weiterhin danke ich besonders meine Bürokollegin Aline Friedrich, die mich stets mit Rat und Tat unterstützt hat. Ebenso gilt mein Dank an Herrn Bernard Lüers für seine hervorragende Engagement bei der Programmierung des Mikrocontrollers und der Leseinheit. Darüber hinaus danke ich Johannes Meyer, Christian Zietz, Christian Orlob, Hanno Raabe, Eckhard Denicke, Nikolai Peitzmeier, Steffen Probst, Lukas Berkelmann, Henning Hartmann und Timo Martinelli für die wertvollen Diskussionen und die gute, kollegiale Zusammenarbeit. Auch ein Dankeschön an die Kolleginnen und Kollegen vom Institut für Mikroproduktionstechnik, Institut für Transport- und Automatisierungstechnik und Laser Zentrum Hannover e.V. für die technologische Unterstützung bei der Herstellung des Transponders.

Ebenfalls möchte ich mich bei allen Studierenden bedanken, mit denen ich zusammenarbeiten konnte.

Außerdem bedanke ich mich noch bei meiner gesamten Familie, die mich stets in jeder Phase meiner Karriere unterstützt hat. Besonders schätze ich die enorme Liebe, Unterstützung, das Verständnis und die Geduld meiner Frau Thi Phuong Linh Vu.



# Kurzfassung

Die intelligente und vernetzte Produktion, auch bekannt unter dem Begriff „Industrie 4.0“, erfordert stets einen Austausch von Daten bzw. Sensordaten. Mit Unterstützung von integrierten, drahtlosen Kommunikationsmodulen soll eine Möglichkeit geschaffen werden, alle bauteilrelevanten Informationen während der Produktions- und Nutzungsphase auszutauschen und bereitzustellen. Für die Umsetzung dieser Vision wird ein miniaturisierter, energieautarkter Radio Frequency Identification (RFID) Transponder mit integrierter Sensorik für den Einsatz innerhalb metallischer Objekte implementiert.

Nach einer Einführung in das Funktionsprinzip eines RFID Systems folgt eine Beschreibung des gestapelten Aufbaukonzepts zu den zu entwickelten 24 GHz RFID Sensor Transponder. Hierbei ist eine optisch transparente Antenne und HF-Schaltung direkt auf eine Solarzelle platziert. Für diese Umsetzung werden sowohl optisch transparente Materialien als auch dünne Gitterleitungen aus Metall auf ihre optischen und elektrischen Eigenschaften untersucht. Die Entscheidung fällt eindeutig zugunsten von Gitterstrukturen aus. Untersuchungen von perforierten Mikrostreifenleitungen hinsichtlich des Zusammenhangs zwischen optischer Transparenz und charakteristischen Eigenschaften wie Einfügedämpfungen und Impedanzverhalten bilden die Grundlage für einen schnellen Designschritt von einer konventionellen zu einer optisch transparenten Analogeinheit.

Darauffolgend wird im Hauptteil dieser Arbeit Patchantennen sowie Modulator- und Demodulatorschaltungen im Detail diskutiert. Zunächst werden die Einflüsse der Gitterlinien und der Solarzelle auf die charakteristischen Antenneneigenschaften analysiert. Die aus Simulationen und Messungen gewonnenen Erkenntnisse werden genutzt, um eine optimierte, optisch transparente Antenne zu entwickeln. Analog zu der beschriebenen Vorgehensweise werden die diskreten HF-Schaltungen unter Berücksichtigung der Einbaumgebung entworfen und messtechnisch verifiziert. Ein innovatives Aufbaukonzept basierend auf ein spritzgegossener Schaltungsträger finden Anwendung, um die hochfrequente, niederfrequente und die energievorsorgende Einheit auf kompakte Weise zu integrieren. Für die Systemevaluierung ist eine Leseinheit entwickelt. Die Komponenten werden einzeln vorgestellt und diskutiert. Eine messtechnische

Bewertung des aufgebauten RFID-Systems bezüglich der zu erwartenden maximalen Kommunikationsreichweite, der Empfängerempfindlichkeit und der Betriebsdauer bei schwachem Umgebungslicht wird in einer Laborumgebung durchgeführt.

**Schlagwörter:** RFID Transponder, Antenne und HF-Schaltung, Gitterstruktur.

# Abstract

Intelligent and networked production, also known as "Industry 4.0", always requires an exchange of data or sensor data. With the aid of integrated wireless communication modules, it is possible to identify the components and to exchange and provide all component-relevant information during the production and application phase. In order to realize this vision, a miniaturized self-sufficient Radio Frequency Identification (RFID) tag with integrated sensor systems will be implemented for use within metallic objects.

An introduction to the functional principle of an RFID system is followed by a description of the stacked design concept for the 24 GHz RFID sensor tag to be developed. Here, an optically transparent antenna and RF circuit is placed directly on a solar cell. Optically transparent materials as well as thin metal grid lines are investigated regarding their optical and electrical properties. The decision is clearly in favor of grid structures. Investigations of meshed microstrip lines regarding the correlation between optical transparency and characteristic properties such as insertion loss and impedance value are the basis for a quick design step from a conventional to an optically transparent analog unit.

In the main part of this work patch antennas and modulator and demodulator circuits are discussed in detail. First, the influences of the grid lines and the solar cell on the antenna properties are investigated. The knowledge gained from simulations and measurements is used to develop an optimized, optically transparent antenna. In analogy to the described procedure, the discrete RF circuits are designed taking into account the installation conditions and verified by measurements. An innovative design concept based on a molded interconnect device is used to integrate the high frequency, low frequency and power supply unit in a compact manner. For the purpose of the overall evaluation, a reading unit is developed. The components are presented and discussed individually. A measurement-based evaluation of the entire RFID system with regard to the expected maximum communication range, receiver sensitivity and operating time in low ambient light is carried out under laboratory conditions.

**Keywords:** RFID Tag, Antenna and RF Circuit, Grid Line Structure.





# Contents

<b>Author's publications</b>	<b>xiii</b>
<b>Abbreviations and Symbols</b>	<b>xv</b>
<b>1 Introduction</b>	<b>1</b>
1.1 Objectives . . . . .	4
1.2 Outline . . . . .	5
<b>2 Radio Frequency Identification Sensor Tag</b>	<b>7</b>
2.1 Principle of an RFID System . . . . .	7
2.2 Operating Frequency . . . . .	8
2.3 Design Concept of the RFID Sensor Tag . . . . .	10
<b>3 Optically Transparent Transmission Lines</b>	<b>13</b>
3.1 Planar Transmission Lines . . . . .	13
3.2 Transparent Conductive Materials . . . . .	14
3.3 Microstrip Lines Based on Metal Grid Lines . . . . .	19
3.3.1 Determination of Propagation Constant and Characteristic Impedance . . . . .	20
3.3.2 Influence of Grid Lines on Characteristic Parameters . . . . .	22
3.3.2.1 Meshed Strip Lines over Solid Ground Plane . . . . .	24
3.3.2.2 Solid Strip Lines over Meshed Ground Plane . . . . .	27
3.3.2.3 Meshed Microstrip Lines . . . . .	27
3.4 Conclusion . . . . .	29
<b>4 Antenna and Analog Front-End Based on Metal Grid Lines</b>	<b>31</b>
4.1 Patch Antenna Design . . . . .	32
4.1.1 Impact of Grid Lines . . . . .	34
4.1.2 Circularly Polarized Patch Antenna . . . . .	39
4.1.3 Influence of a Solar Cell on Antenna Characteristics . . . . .	41
4.1.4 Final Antenna Layout . . . . .	45
4.1.5 Conclusion . . . . .	49

4.2	Discrete Circuit Design . . . . .	49
4.2.1	Modulator Unit . . . . .	49
4.2.1.1	Principle of the Backscatter Modulation . . . . .	50
4.2.1.2	Design Concept and Characteristics of the Modulator Circuit . . . . .	53
4.2.2	Demodulator Unit . . . . .	54
4.2.3	Modulator and Demodulator Unit - Reference Circuit . . . . .	59
4.2.4	Modulator and Demodulator Unit Based on Metal Grid Lines . . . . .	62
4.2.4.1	Circuit Designed for Verification . . . . .	63
4.2.4.2	Final Circuit . . . . .	66
4.2.5	Conclusion . . . . .	72
4.3	Fabrication Process . . . . .	73
4.4	Optical Transparency . . . . .	74
<b>5</b>	<b>RFID System</b> . . . . .	<b>77</b>
5.1	RFID Sensor Tag . . . . .	77
5.1.1	Baseband Unit . . . . .	78
5.1.1.1	Current Consumption of the MCU . . . . .	80
5.1.2	Solar Cell . . . . .	82
5.1.3	Energy Storage and Operating Time . . . . .	85
5.1.4	Realization of the Baseband Unit on a 3D-MID . . . . .	88
5.1.5	Assembly of the Tag . . . . .	90
5.1.6	Conclusion . . . . .	91
5.2	Reader Unit . . . . .	92
5.2.1	Analog unit . . . . .	93
5.2.1.1	Local Oscillator . . . . .	94
5.2.1.2	Absorptive SPST Switch . . . . .	94
5.2.1.3	Frequency Multiplier . . . . .	94
5.2.1.4	Power Divider . . . . .	95
5.2.1.5	Antennas . . . . .	95
5.2.1.6	IQ Receiver . . . . .	97
5.2.1.7	Operational Amplifier . . . . .	99
5.2.1.8	Realization of the Analog Unit . . . . .	102
5.2.2	Digital unit . . . . .	103
5.2.3	Communication Protocol . . . . .	104
5.2.4	Conclusion . . . . .	106

5.3	Evaluation of the RFID System . . . . .	107
5.3.1	Sensitivity of the Reader . . . . .	107
5.3.2	Sensitivity of the Tag . . . . .	108
5.3.3	Conclusion . . . . .	110
<b>6</b>	<b>Summary and Results</b>	<b>111</b>
	<b>Bibliography</b>	<b>115</b>



## Author's publications

The following work contains materials and text passages based on the following publications and contributions authored or co-authored by the author.

- [QHD1] Q. H. Dao, L. Grundmann, and B. Geck, "Optically Transparent 24 GHz Analog Front-End Based on Meshed Microstrip Lines for the Integration in a Self-Sufficient RFID Sensor Tag," *IEEE Journal of Radio Frequency Identification*, vol. 4, no. 2, pp. 83–92, 2020.
- [QHD2] Q. H. Dao, R. Tchuigoua, B. Geck, D. Manteuffel, P. von Witzendorff, and L. Overmeyer, "Optically transparent patch antennas based on silver nanowires for mm-wave applications," in *2017 IEEE International Symposium on Antennas and Propagation USNC/URSI National Radio Science Meeting*, July 2017, pp. 2189–2190.
- [QHD3] Q. H. Dao, A. Skubacz-Feucht, B. Lueers, P. von Witzendorff, C. von der Ahe, L. Overmeyer, and B. Geck, "Novel design concept of an optoelectronic integrated RF communication module," in *3rd International Conference on System-Integrated Intelligence: New Challenges for Product and Production Engineering*, vol. 26, 2016, pp. 245–251. [Online]. Available: <http://www.sciencedirect.com/science/article/pii/S2212017316303802>
- [QHD4] Q. H. Dao, B. Lueers, T. T. Ngo, and B. Geck, "An optically transparent analog frontend for a solar powered 24 GHz RFID transponder," in *2016 IEEE MTT-S International Microwave Symposium (IMS)*, 2016.
- [QHD5] Q. H. Dao, T. J. Cherogony, and B. Geck, "Optically transparent and circularly polarized patch antenna for k-band applications," in *2016 German Microwave Conference (GeMiC)*, 2016, pp. 247–250.
- [QHD6] Q. H. Dao, R. Braun, and B. Geck, "Design and investigation of meshed patch antennas for applications at 24 GHz," in *2015 European Microwave Conference (EuMC)*, 2015, pp. 1499–1502.

## Co-authored:

- [QHD7] B. Denkena and T. Mörke, Eds., *Cyber-Physical and Gentle Intelligent Systems in Manufacturing and Life Cycle*. Elsevier, 2017. [Online]. Available: <https://linkinghub.elsevier.com/retrieve/pii/C20160003741>
- [QHD8] J. Meyer, Q. H. Dao, and B. Geck, "24 GHz RFID communication system for product lifecycle applications," in *2nd International Conference on System-Integrated Intelligence: Challenges for Product and Production Engineering*, vol. 15, 2014, pp. 369–375. [Online]. Available: <http://www.sciencedirect.com/science/article/pii/S2212017314002060>
- [QHD9] J. Meyer, Q. H. Dao, and B. Geck, "Design of a 24 GHz analog frontend for an optically powered RFID transponder for the integration into metallic components," in *2013 European Microwave Conference*, 2013, pp. 1531–1534.

# Abbreviations and Symbols

## Abbreviations

3D-MID	Three-dimensional Molded Interconnect Device
A/D	Analog Digital
AC/DC	Alternating Current/Direct Current
ADC	Analog to Digital Converter
ADS	Advanced Design System (Software from PathWave Design)
AgNWs	Silver Nanowires
AR	Axial Ratio
ASK	Amplitude Shift Keying
BGA	Ball Grid Array
CAD	Computer-Aided Design
CPW	Coplanar Waveguide
CRC	Collaborative Research Centre
DC	Direct Current
DUT	Device Under Test
E-field	Electric field
EIRP	Equivalent Isotropically Radiated Power
EM	Electromagnetic
E-pHEMT	Enhancement Mode Pseudomorphic High Electron Mobility Transistor
ERP	Effective Radiated Power
FPGA	Field Programmable Gate Array
GND	Ground, ground plane
GSG	Ground Signal Ground
GUI	Graphical User Interface
HEMT	High Electron Mobility Transistor
HF	High Frequency
HFSS	High Frequency Structure Simulator (commercial tool from Ansys)
HPF	High Pass Filter
I <sup>2</sup> C	Inter-Integrated Circuit

I-channel	In-phase channel
IC	Integrated Circuit
ID	IDentification
IQ	In-phase, Quadrature
ISM	Industrial Scientific and Medical
ITO	Indium Tin Oxide
LDS	Laser Direct Structuring
LGA	Land Grid Array
LNA	Low Noise Amplifier
LO	Local Oscillator
LTCC	Low Temperature Cofired Ceramics
MCU	Microcontroller
MID	Molded Interconnect Device
NIST	National Institute of Standards and Technology
MMIC	Monolithic Microwave Integrated Circuits
MoM	Method of Moments
MSL	Microstrip line
PC	Personal Computer
PCB	Printed Circuit Board
PCI	Peripheral Component Interconnect
PLL	Phase Lock Loop
Q-channel	Quadrature channel
RCS	Radar Cross Section
RF	Radio Frequency
RFID	Radio Frequency Identification
RHCP	Right Hand Circular Polarization
S-parameter	Scattering parameter
SMD	Surface Mount Device
SPST	Single Pole Single Throw switch
TEM	Transverse Electromagnetic Mode
TLR	Thru Line Reflect
TTL	Transistor-Transistor Logic
UHF	Ultra High Frequency
UV	Ultraviolet

## Symbols

$A_e$	Effective aperture
-------	--------------------



---

$C$	Capacitor
$c$	Speed of light in vacuum
$C_j$	Junction capacitance
$C_P$	Parasitic capacitance of a diode
$D$	Diode
$d$	Distance
$d_{max}$	Maximum distance
$d_{R, max}$	Maximum communication distance of the reader
$d_{T, max}$	Maximum communication distance of the tag
$f$	Frequency
$f_r$	Resonance frequency
$G$	Antenna gain
$G_{dipol}$	Gain of a dipol antenna
$G_{meas}$	Measured antenna gain
$G_p$	Peak gain of a patch antenna
$G_{p,sc}$	Peak gain of a patch antenna on a solar cell
$G_{p,solid}$	Peak gain of a solid patch antenna
$G_R$	Antenna gain of the reader
$G_{rx}$	Gain of the received antenna of the reader
$G_{sim}$	Simulated antenna gain
$G_{Tag}$	Antenna gain of the tag
$G_{tx}$	Gain of the transmitted antenna of the reader
$g$	Gap
$g_x$	Gap between grid lines oriented in x-direction
$g_y$	Gap between grid lines oriented in y-direction
$h$	Height
$h_{sub}$	Height of a substrate
$I$	Current
$I_F$	Forward current of a diode
$I_{GS}$	Gate source current
$I_S$	Saturation current of a diode
$I_{SC}$	Short-circuit current
$I_{SolarCell}$	Current of a solar cell
$L$	Loss factor in free space
$l$	Length
$l_f$	Length of the feed line
$l_{GND}$	Length of the ground plane
$L_P$	Parasitic inductance of a diode

$l_{Patch}$	Length of the patch
$MF_A$	$MeshFactor_A$ , ratio of the metal-filled area to the total area
$MF_x$	$MeshFactor_x$ , area covered with metal in x-direction
$MF_y$	$MeshFactor_y$ , area covered with metal in y-direction
$n_x$	Number of grid lines oriented in x-direction
$n_{x,GND}$	Number of grid lines oriented in x-direction on ground plane
$n_y$	Number of grid lines oriented in y-direction
$n_{y,GND}$	Number of grid lines oriented in y-direction on ground plane
$P_{GS}$	Power consumption of the transistor by applying $V_{GS}$
$P_{in}$	Input power
$P_{Reader, min}$	Sensitivity of the reader, minimum detectable input power
$P_{Tag}$	Power at the tag
$P_{Tag, min}$	Sensitivity of the tag, minimum detectable input power
$P_{Tx}$	Transmitted power of the reader
$R_L$	Load resistance
$R_S$	Losses in the terminals of the diode
$R_V$	Video resistance
$S_{11}$	Input reflection coefficient
$T$	Optical transmittance
$t$	Thickness
$w$	Width
$w_f$	Width of the feed line
$U$	Voltage
$U_g$	Voltage of the source
$V_{Cap}$	Voltage across a supercapacitor
$V_{cc}$	Supply voltage
$V_D$	Voltage across a diode
$V_{DS}$	Drain source voltage
$V_F$	Forward voltage of a diode
$V_{GS}$	Gate source voltage
$V_{in}$	Input Voltage
$V_{OC}$	Open-circuit voltage
$V_{out}$	Output Voltage
$V_{SolarCell}$	Voltage of a solar cell
$y_p$	Position of the probe feed in y-direction
$w_{ms}$	Width of a microstrip line
$w_x$	Width of a grid line oriented in x-direction
$w_{x,GND}$	Width of a grid line oriented in x-direction on ground plane

---

$w_y$	Width of a grid line oriented in y-direction
$w_{y,GND}$	Width of a grid line oriented in y-direction on ground plane
$Z$	Impedance
$Z_A$	Impedance of the antenna
$Z_{Coax}$	Characteristic impedance of a coaxial probe
$Z_e$	Load impedance
$Z_g$	Source impedance
$Z_{ref}$	Reference Impedance
$Z_0$	Characteristic impedance
$Z_1$	Impedance at state 1 (mismatched state)
$Z_2$	Impedance at state 2 (matched state)
$\alpha$	Real part of the propagation constant (attenuation constant)
$\beta$	Imaginary part of the propagation constant (phase constant)
$\beta_0$	Phase constant in free space
$\Gamma$	Input reflection coefficient
$\Gamma_1$	Input reflection coefficient at mismatched state
$\Gamma_2$	Input reflection coefficient at matched state
$\gamma$	Propagation constant
$\gamma_D$	Sensitivity of a diode including parasitic parameters
$\gamma_s$	Sensitivity of a diode
$\Delta l$	Length of a truncated edge
$\Delta\Gamma$	Differential reflection coefficient
$\tan \delta$	Loss tangent
$\epsilon'_r$	Permittivity
$\vartheta$	Angle in degree
$\lambda$	Wavelength
$\lambda_g$	Guided wavelength
$\rho$	Specific electrical resistance
$\sigma$	Radar cross section
$\sigma_0$	Static backscatter
$\sigma_m$	Modulated backscatter
$\sigma_{Cu}$	Electrical conductivity of Copper
$\sigma_{ITO}$	Electrical conductivity of Indium Tin Oxide
$\sigma_{SC}$	Electrical conductivity of a photovoltaic layer (solar cell)
$\sigma_{AgNWs}$	Electrical conductivity of Silver Nanowires
$\varphi$	Angle in degree



Intelligent devices and objects that network and communicate with each other, also known under the term Internet of Things (IoT), are part of our private and professional lives - from personal wearables to products that are used within smart cities [1] or industrial environments [2]. Industrial applications often require integrated wireless communication systems, e.g. "Industry 4.0". Thus, suitable intelligent wireless communication modules are needed to exchange data with each other and during its life cycle in an efficient way. Depending on the application, such modules have to meet different requirements. These include, for example: identifiability, integrability on/in almost any objects, ability to collect, process and store data, etc..

Regarding the term identifiability Radio Frequency IDentification (RFID) technology [3] is already established in the private and industrial market. Typically, an RFID system consists of a reader, which acts as an active device, and a tag, usually a passive device, with its unique ID number. The tag consists of an antenna, an analog circuit and a digital unit and is attached to the object to be identified. The advantages of the RFID technology include in particular the wireless and energy-efficient data transmission, which is the result of the backscatter communication principle. The areas of application include for example identification of persons, animals and objects, supply chain management, anti-counterfeiting of products or cashless payment systems. A special application is the identification of metallic components such as casting parts [4], structural steel products [5], tools [6] or medical devices and surgical instruments [7]. For these applications, the antenna must be specially adapted to metallic surroundings, which leads to an additional challenge in designing the tag. This is because conventional tag antennas e.g. dipole antennas which can be found in common tags, show a significant decrease in their radiation efficiency in such an environment. There are commercial passive tags for integration on/in non-metal and metal objects in the HF (high frequency) and UHF (ultra-high frequency) range, but the functionality is limited to simple identification by the unique ID number [8–10]. If additional memory is needed for user data, these tags typically offer a memory size of about 512 bits.

In the field of networked manufacturing and self-organizing processes all related data, e.g. design and process parameters, load information of the component can be stored on the tag in addition to a central database to enable an adaptive manufacturing planning, a monitoring of production steps and an online process-monitoring [11]. To meet these requirements the tag must provide sufficient memory space (>1 kB), an option for sensor integration and a bidirectional communication to exchange data with a reader unit. The data e.g. temperature and acceleration values gathered from integrated sensor systems can be accessed at any time for analysis in order to improve the manufacturing process and to enhance the product quality [12].

In order to realize the aforementioned vision of an intelligent and networked production, an RFID sensor tag was researched within the interdisciplinary Collaborative Research Centre 653 entitled "Gentelligent components in their lifecycle - Utilization of inheritable component information in product engineering", which has been funded since 2005 [13]. One of the challenging tasks is the combination of RFID tags and metal objects. For a safe and durable mechanical integration, it is preferable to place the tag in instead of on the component. This is because in a harsh production environment the tag can be easily damaged, for example by external mechanical forces. This can be caused both during a processing step within the production and in the later application area.

In the first funding period (2005 – 2009) a passive RFID tag operating in the 5.8 GHz Industrial Scientific and Medical (ISM) band was developed [14]. The tag is powered by the electromagnetic (EM) field and a unidirectional communication range of 22 cm was achieved. The design concept required a drill hole with a diameter of 20 mm and a length of 49 mm in the metal component, which acts as both a circular waveguide and an aperture antenna. However, a large drill hole reduces the mechanical stability of the component and thus limits the area of application. In order to overcome this limitation, the size of the tag should be reduced. Since the antenna size depends on the operation frequency, the use of the next higher license-free ISM frequency band at 24 GHz is a promising approach. A disadvantage of the 24 GHz operating frequency compared to lower frequency is the higher free space path loss [15], which results in lower available rectified supply voltage (at a fixed distance) to power the tag.

In order to solve the challenge of power supply and communication range, a design concept of a semi-passive RFID tag was used in the second funding period (2009 – 2013) [16]. The 24 GHz RFID tag is placed in a drill hole with a diameter of 8 mm and a length of 26 mm. Compared to the tag realized in the

first funding period, a reduction in the overall size was achieved. The tag consists of an aperture antenna (antenna gain of 4.4 dBi), a modulator and demodulator circuit, a microcontroller and a data memory chip. These units are arranged sequentially and aligned along the drill hole. The tag is powered by a solar cell that is aligned transverse to the drill hole. A hybrid waveguide has been developed which fulfills two functions: a defined guidance of light to the solar cell and the transmission of the RF data signal. A bidirectional data exchange was achieved with a communication range of approx. 0.5 m. The fabricated tag could be verified by experiments as sufficient for the application described above.

Passive RFID tags (operating frequency at 24 GHz) presented in [17–19] are in the overall dimension less than  $3.74 \text{ mm} \times 1.86 \text{ mm}$ , but the achievable communication distance is in the range of few centimeters. In this case, a dipole antenna is realized on the chip that includes RF, memory, and digital components. These results show that the size of the tag can be further reduced, but to the disadvantage of aspects such as large communication range, sufficient power supply and flexible connection of sensors. To meet the vision of the project, the approach of a semi-passive tag is still promising. Furthermore, the tag miniaturization aspect is always important. Since the area of application of the 24 GHz RFID tag is essentially defined by the physical dimensions, a further reduction of the overall volume, in particular of the geometric length of 26 mm of the hybrid waveguide achieved so far in the second funding period, is to be striven for. Based on the knowledge gained, an innovative design approach is investigated in this work. The focus is on increasing the degree of integration between optical and electrical components.

In this work, the concept of a semi-passive RFID tag based on a solar cell is pursued. A battery-less solution is deliberately chosen, since a battery limits the lifetime of the tag. In order to provide sufficient energy for the digital circuit and especially for the sensor systems, it is obvious to use a solar cell with a high efficiency and a large optical aperture. An increase in the size of a solar cell is not arbitrarily possible and contradicts the goal of a miniaturized tag. Thus, a reduction of the space usage can be achieved by a placement of a planar antenna and RF circuit on the solar cell instead next to it. This leads to a stacked assembly concept and requires an optically transparent analog front-end in order to reduce the shading of the solar cell underneath. This leads to a further challenge in the design of the optically transparent RF circuit while simultaneously increasing the sensitivity achieved so far (in the second

funding period). It is well-known that the sensitivity contributes significantly to an increase in the communication range. For this reason, both the optically transparent antenna and the modulator and demodulator circuit to be designed must be optimized to ensure a communication distance greater than 0.5 m. This can in turn extend the application area of the RFID sensor tag.

In short, the main challenge in the development of the antenna and analog front-end is to identify and quantify all interactions between the optical and electrical components. An optimum between the best possible energy generation and the highest possible efficiency of the RF structures must be found. The following key requirements for a miniaturized RFID sensor tag can be derived from the aforementioned description and the achieved system parameters from the second funding period:

- Lowest possible overall dimensions
- Can be integrated in metallic objects
- Includes data processing unit, data storage and flexible sensor connectivity
- Longest possible lifetime with energy self-sufficient operation
- Largest possible operating range with the reader unit ( $> 0.5$  m)
- Bidirectional communication
- Circularly polarized antenna with a gain value of approx. 4 dBi

In addition to the research and development of an RFID sensor tag, a reader unit is also to be implemented. It is needed for the evaluation of the tag and for the communication and data exchange. The requirements on the reader are a broad coverage area by using antennas with a wide field of view as well as a high receiver sensitivity for a largest possible communication range.

## 1.1 Objectives

The main focus of this work were derived from the previously defined requirements for the RFID system, especially the sensor tag. These objectives are:

- Design and development of an optically transparent antenna and analog front-end.



- Realization of a miniaturized, self-sufficient RFID sensor tag which can be integrated in metallic components.
- Implementation of an RFID reader unit for the communication and data exchange with the sensor tag.

## 1.2 Outline

This work is divided in six Chapters, beginning with an introduction in Chapter 1.

The following Chapter 2 describes the composition and the principle of an RFID system in general. Here, the chosen operating frequency and the corresponding limitations on the tag are discussed. Subsequently, a design concept of an RFID sensor tag that is to be realized is presented. This provides an overview of the components to be investigated.

Chapter 3 deals with the characteristics of optically transparent transmission lines. For this purpose, transmission lines to be considered are first presented. Some promising optically transparent and electrically conductive materials are characterized regarding its optical and electrical properties. Afterwards, an alternative way to achieve an optically transparent microstrip line based on grid lines made of conventional metals is examined. The characteristic impedance and propagation constant of microstrip lines with different transparency are studied in detail. The knowledge obtained should be used to simplify the design step from an opaque circuit to an optically transparent circuit.

Chapter 4 describes the design of a patch antenna and an analog front-end, which are an important part of the RFID tag. At first, the final layout of both units is shown to give an overview of the RF structures. Next, the investigations on meshed patch antennas are presented. The influences of the grid lines as well as the solar cell underneath on the antenna characteristics are addressed. With the knowledge gained from simulations and measurements, an optimized antenna is designed and its characteristics are discussed. Afterwards, the analog front-end consisting of a modulator and demodulator unit is investigated. A non-transparent reference circuit is designed followed by a design transfer of this circuit to an optically transparent analog front-end. The obtained characteristics are discussed in detail. Furthermore, a verification of the simulated results are carried out by a measurement. The last two sections deal with the used fabrication process to obtain the antenna and the analog front-end based on metal grid lines and an optical simulation to determine the transparency of the whole unit.

Chapter 5 presents the developed RFID system in detail. First, the digital unit of the sensor tag is described. It consists mainly of a microcontroller, a triaxial acceleration sensor and a simple power harvester. The properties of each unit are discussed in detail. Furthermore, the circuit of the digital unit is realized on a three-dimensional molded interconnect device. Thus, the used technology and the assembly process of the tag is described. In order to verify the functionality of the fabricated RFID sensor tag, a reader unit and a defined communication protocol are needed. Hence, the utilized RF components of the analog unit and the digital unit with the implemented communication procedure are presented. The last section deals with the evaluation of the developed RFID system considering the sensitivity of the reader as well as the tag and the related maximum communication range.

Chapter 6 summarizes the main findings of this work.

# Radio Frequency Identification Sensor Tag

The communication system to be realized in this work is based on backscatter communication, a technology that is widely used in Radio Frequency Identification (RFID) applications. In addition to the identification functionality, the providing and storage of data, sensors should be integrated in the tag to obtain an RFID sensor tag. Sec. 2.1 describes the main components and the basic characteristics of an RFID system. Afterwards, a discussion on the selected frequency band and the associated limitations is carried out in Sec. 2.2. Sec. 2.3 deals with the design concept of the RFID sensor tag. Hereby, a modular approach is discussed.

## 2.1 Principle of an RFID System

Radio Frequency Identification, also known under the abbreviation RFID, is an electronic, wireless technology for the identification of objects, persons or animals. In general, all RFID systems consist of two main components: a tag that is integrated on/in an object to be identified by means of a unique ID number and a reader unit that reads the data from the tag and optionally transmits data to the tag. For the storage of the data commercially available tags have a small memory in the range of some kB integrated [8–10].

In order to expand the scope of function of a tag an additional sensor can be

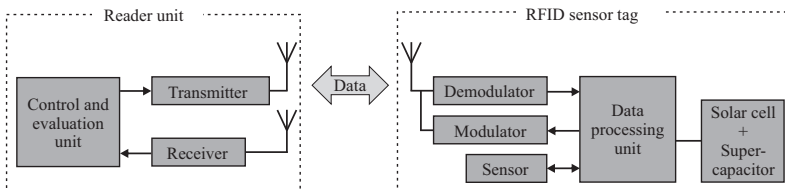


Figure 2.1 Block diagram of an RFID system consisting of a reader unit and a self-sufficient RFID sensor tag.

used. Thus, an RFID sensor tag can be obtained. A block diagram of the RFID sensor tag system developed in this work is depicted in Fig. 2.1. The reader consists of a control and evaluation unit that is connected with a transmitter and a receiver. The wireless communication e.g. request/storage of data from/to the tag is carried out via the respective antenna. The tag can be divided into the following units: antenna, demodulator, modulator, data processing unit (microcontroller), sensor and power supply (solar cell and supercapacitor). In this work, the data transmission from the tag to the reader is realized via the well-known backscatter modulation principle based on Amplitude Shift Keying (ASK). The described configuration (power supply and backscatter modulation) is referred to as semi-passive tag [3]. The main advantage compared to active tags is that no energy is required for generating the RF signal. Thus, the operating time can be increased. A design approach based on the concept of passive RFID tag is difficult to realize since the gathered energy from the electromagnetic (EM) field generated by the reader is not sufficient to power both the data processing unit and the sensor. Furthermore, a continuous data logging without the reader unit is not possible.

## 2.2 Operating Frequency

In addition to the classification of tags according to the power supply, RFID systems can also be classified according to their used coupling mechanism between the reader unit and the tag. These include inductive near-field coupling and electromagnetic far-field coupling. Far-field coupled systems usually have a higher communication range and a higher data rate. In this work, the sensor tag should operate in far-field region. For this reason, the frequency ranges and the maximum permissible radiated power will be discussed in the following.

The Bundesnetzagentur [20] is responsible for the frequency regulation in Germany. It ensures that different wireless applications do not interfere with each other. Table 2.1 depicts the permitted frequency bands for RFID applications. The abbreviations ERP and EIRP stand for equivalent radiated power of a half-wave dipole antenna and equivalent isotropic radiated power of a theoretical isotropic antenna, respectively. The relation between these two definitions can be given as follows:

$$EIRP = G_{dipol} \cdot ERP = 1.64 \cdot ERP. \quad (2.1)$$

The factor 1.64 is the antenna gain of an ideal half-wave dipole antenna compared to the isotropic radiator. The equivalent isotropic radiated power of a reader

Frequency range (MHz)	Maximum permissible radiated power (W)
865 - 868	2 (ERP)
2446 - 2454	0.5 (EIRP)

Table 2.1 Frequency bands for radio applications for identification purposes according to the Bundesnetzagentur [21].

Frequency range (GHz)	Maximum permissible radiated power (mW)
2.400 - 2.483	10 (EIRP)
5.725 - 5.875	25 (EIRP)
24.00 - 24.25	100 (EIRP)
61.0 - 61.5	100 (EIRP)

Table 2.2 Several frequency bands (ISM bands) for the use by short range radio applications for non-specified applications according to the Bundesnetzagentur [21].

corresponds to the product of the transmitted power and the antenna gain value in the main beam direction.

Moreover, there are license-free frequency bands for Industrial, Scientific and Medical (ISM) applications that are available worldwide. Any application can be operated in the respective ISM band. The allowed radiated power is regulated by the individual country. The maximum permissible radiated power for several ISM bands is shown in Table 2.2. These values are valid for non-specific short-range devices operating in Germany.

In this work, the 24 GHz ISM band is used because in this case the size of the antenna is smaller compared to an antenna operating at 5.8 GHz or 2.4 GHz. Thus, the overall dimension of the tag is not only defined by the antenna. The 61 GHz ISM band was not chosen because the design and implementation of the tag and the reader unit with discrete RF components is more complex than the realization at 24 GHz. In addition, it is very difficult to find suitable commercially available RF components or RF modules to implement a cost-effective reader. Furthermore, the communication distance depends, among other things, on the selected operating frequency. For an application scenario with a distance of  $d = 1$  m and an operating frequency of 24 GHz, the free-space loss factor  $L$  is

calculated as follows [22]:

$$L = 10 \log_{10} \left( \left( \frac{4\pi df}{c} \right)^2 \right) \text{ dB} = -60 \text{ dB}, \quad (2.2)$$

where  $c$  is the speed of light in vacuum. Using the 61 GHz ISM band the free space path loss factor would be approx.  $-68$  dB. In this case, the sensitivity value of the tag should feature additional  $-8$  dB in order to achieve the same communication distance compared to the implementation at 24 GHz. This would lead to an even greater challenge in designing the RF circuit.

### 2.3 Design Concept of the RFID Sensor Tag

Based on the specification for the RFID sensor tag described in the introduction of this work, a design concept is developed which will be described in the following. The key components of a tag are shown in Fig. 2.1.

The main focus is on the realization of a miniaturized, self-sufficient sensor tag which can be integrated in as many different metallic components as possible. The integration in an object can be realized e.g. by a small milled pocket. Fig. 2.2 shows some possible application examples. The design concept of the



Figure 2.2 Photograph of possible application examples: sensor tag integrated in metallic parts.

RFID sensor tag developed is depicted in Fig. 2.3. The exploded view shows the highly integrated multilayer structure consisting of four main parts. The overall volume is  $13\text{ mm} \times 13\text{ mm} \times 4\text{ mm}$ . In order to design a compact tag a three-dimensional molded interconnect device (3D-MID) [23] is used as a housing and circuit carrier simultaneously. In this way, the number of parts can be reduced. By means of the laser direct structuring (LDS) process [23], electronic conducting paths can be realized directly on the surface of the plastic part (see Sec. 5.1.4). Thus, on both side of the MID housing and on the inner walls there are conductor tracks for the electrical connection of the solar cell and the RF circuit as well as the baseband unit.

The baseband unit is placed on the back side of the MID housing. The electrical connection between the top and the bottom layer is done by through hole vias. This production step can be realized completely within the LDS process. Hereby, the laser drills through the plastic part and at the subsequent metallization process copper deposits in the hole. In this way, a reliable connection can be achieved. The digital unit consists of an ultra-low power microcontroller, a triaxial acceleration sensor for a continuous process monitoring of load parameters as well as several surface-mount devices (SMD) for the circuitry. All electrical components are soldered on the MID housing using a reflow soldering process. A diode and a supercapacitor as part of the energy harvesting concept

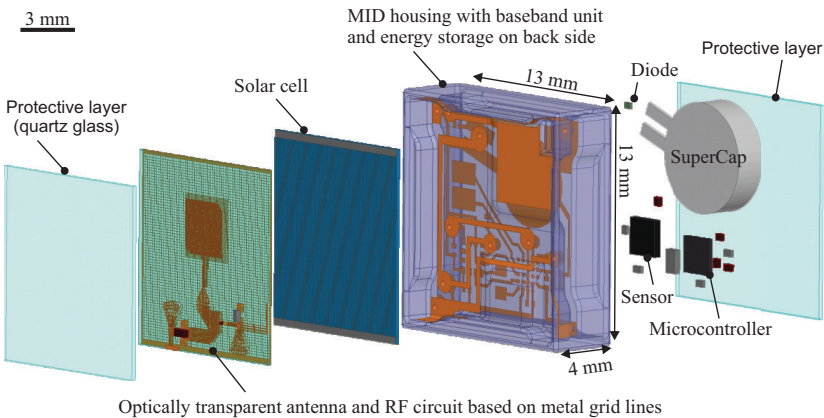


Figure 2.3 Exploded view of the developed self-sufficient RFID sensor tag.

are placed on the back side while the solar cell is on the top side of the 3D-MID component. In this design concept, the size of the selected commercially available solar cell [24] determines mainly the shape, the length and the width of the tag. The entire back panel area of the single metamorphic solar cell providing the positive voltage is fully adhered to the 3D-MID component. Thus, a reliable mechanical connection is realized. The interconnection between the front-side (ground connections) of the solar cell, also known as busbars, and the conductor tracks on the side walls of the 3D-MID is also done by conductive adhesive.

For the wireless communication, an antenna and an analog front-end are needed. In order to obtain a compact sensor tag these units are arranged on top of the solar cell instead of next to it. In this case, the antenna and the RF circuit are placed on the same layer. If these components are arranged on different layers, e.g. the RF circuit is on the back side of the 3D-MID, the design of the RF interconnection would be more complex. Furthermore, a longer transmission line between both elements would cause a higher insertion loss. RF circuits are often realized in printed circuit board (PCB) technology because of the simple manufacturing process. A common type of transmission lines is the microstrip line consisting of an electrically conducting strip separated from a ground plane by a dielectric substrate. Since the RF circuit is to be designed with microstrip lines, a concept based on a patch antenna is preferred. In this case, the feed line can be designed in a simple way. Additionally, a patch antenna meets the pre-defined specifications of the antenna: functionality in metallic environment, a minimum antenna gain value of at least  $G \geq 4$  dBi and the capability to transmit circularly polarized waves. One of the main challenges is to design an antenna as well as an analog front-end with the highest possible transparency value in order to minimize the shading effect on the solar cell. Thus, suitable materials with optimal optical and electrical properties need to be studied.

To protect the RFID sensor tag against environmental impact such as dust, dirt, etc. a protective layer is used on both the top and back sides. Especially the top layer should fulfill requirements such as high optical transparency and resistance against environmental influences.

In the following chapters, each unit is presented and discussed individually.



# Optically Transparent Transmission Lines

In order to realize the concept of the RFID sensor tag, investigations on electrically conductive and simultaneously optically transparent materials are needed. First, Sec. 3.1 briefly presents planar transmission lines that are used in this work. A discussion on some promising materials is given in Sec. 3.2. Here, the investigated materials are characterized on the optical and electrical properties. Sec. 3.3 deals with an alternative way to achieve an optically transparent transmission line based on conventional metals. The properties of microstrip lines made of metal grid lines are analyzed in terms of characteristic impedance and propagation constant. At the end of this chapter a brief conclusion is given.

## 3.1 Planar Transmission Lines

The commonly used planar transmission lines that can be easily fabricated on printed circuit boards (PCBs) include microstrip line and coplanar waveguide. A cross section view of both type of transmission lines is shown in Fig. 3.1. The substrate with a relative dielectric constant  $\epsilon_r$  is usually optically opaque. Since the PCB is to be placed on top of a solar cell for later application, the carrier material must ideally have a high optical transparency. Thus, a suitable approach is the use of glass as substrate. Fig. 3.1a shows a microstrip line consisting of a strip line with a line width  $w$  and a ground plane. The dominant mode is the quasi-TEM mode (transverse electromagnetic field mode). A coplanar

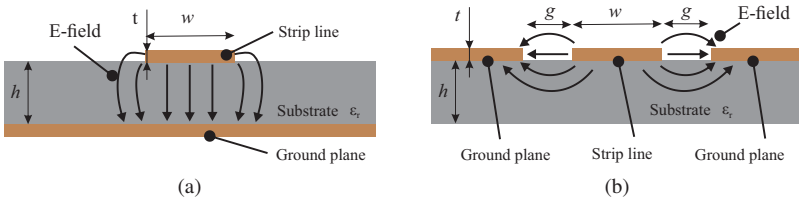


Figure 3.1 Cross section view of (a) a microstrip line (MSL) and (b) a coplanar waveguide (CPW).

waveguide (CPW) consists of a strip line with a line width  $w$  and a ground plane. Both components are on the same plane. The strip line and the ground plane are separated by a gap  $g$ . Fig. 3.1b depicts the electric field lines of the even mode of the CPW. In the following, both presented transmission lines are utilized for the characterization of optical and electrical materials.

## 3.2 Transparent Conductive Materials

Optically transparent and electrically conductive materials are widely used in well-known applications such as photovoltaics, displays and touch screens. Materials include for example graphene thin films, carbon nanotube networks, transparent conducting oxide and metal nanowire networks. There are two promising materials with low surface resistance that can be used for the fabrication of the antenna: Indium Tin Oxide (ITO) [25] and silver nanowires (AgNWs) [26]. In case of ITO this material can be deposited e.g. on quartz glass by a radio frequency (RF) sputtering process. In this work, the coating

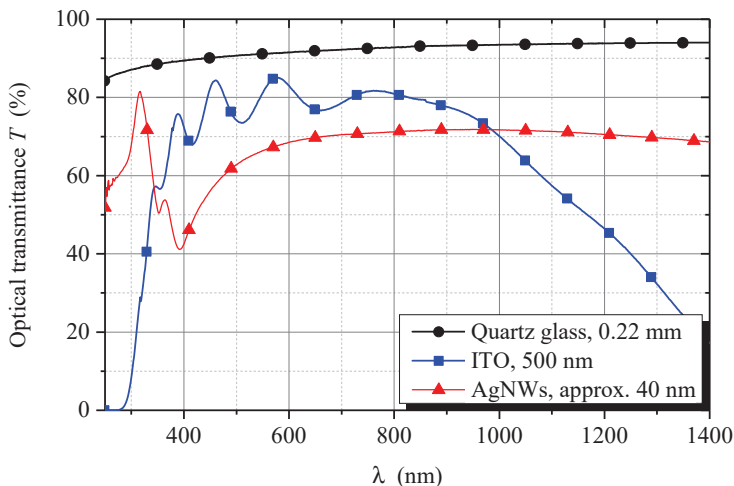


Figure 3.2 Transmittance of optically transparent and electrically conductive materials as well as the transmittance of quartz glass.

procedure is done by an external service provider (Fraunhofer IST). The optical and electrical properties vary depending on special techniques and methods e.g. gases, pressure and temperature used. The coating thickness can be controlled by the deposition time. Fig. 3.2 depicts the optical transmittance as a function of the wavelength for the used quartz glass with a thickness of 0.22 mm and the material ITO with a thickness of 500 nm. The measurements are done with a spectrometer Lambda 900 by the project partner Laser Zentrum Hannover e.V.. The highest conductivity values of ITO given in literature are in the range of  $\sigma \approx 0.5 \text{ MS/m}$  up to  $\sigma \approx 1 \text{ MS/m}$ . The electrical characterization of this material used is presented in the section after next.

In [27] it is found out that AgNWs is one of the best materials offering good optical properties. The conductivity value is higher compared to ITO and it strongly depends among other things on the geometry of the wires, the coating thickness and the methods used to improve the electrical properties [28, 29]. In this work, AgNWs named ECOS HC [30] from RAS AG with a mean diameter of  $0.04 \mu\text{m}$  and a mean length of  $15 \mu\text{m}$  are used for investigation. The production steps of a coating are as follows: The 3% silver nanowires (dispersed in ethylenglycol) are dispersed in isopropyl alcohol (mixing ratio 1:2). Subsequently, the solvent is coated on quartz glass by means of a spin coating process (process parameter: acceleration = 2000 rpm/s, speed = 800 rpm and total duration = 20 s). After this production step, the coating is tempered on a heating plate at  $200^\circ\text{C}$  for 6 minutes. In this way, an optical transmission of  $T = 67.9\%$  at a wavelength of  $\lambda = 550 \text{ nm}$  is achieved for a single AgNWs coating

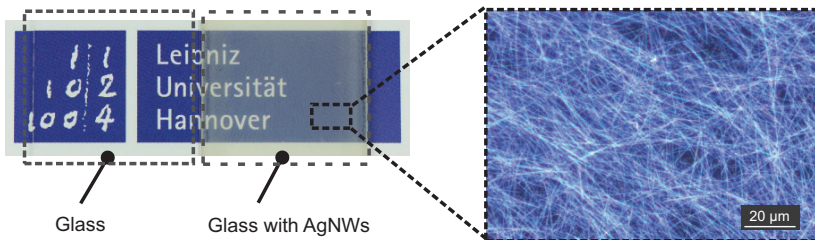
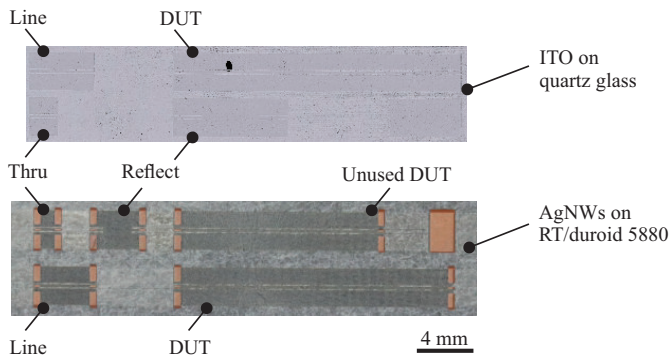


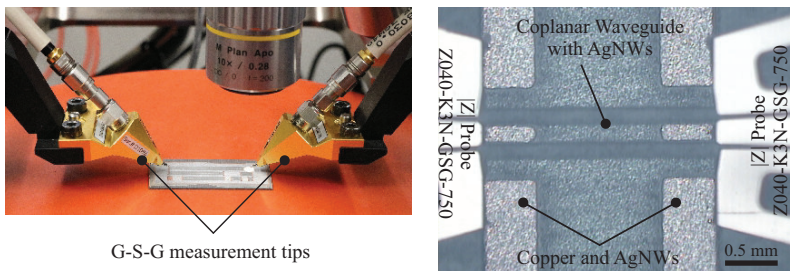
Figure 3.3 Photograph of a glass substrate and a glass substrate with an AgNWs coating (logo of the university in the background) and microscopic image of a single AgNWs coating with 67.9% optical transmission at 550 nm.

with a mean thickness of approx. 40 nm. The wave-dependent transparency values are shown in Fig. 3.2. A photograph and a microscopic image of the realized AgNWs coating can be seen in Fig. 3.3.

Once optical properties of the two presented materials have been determined, their electrical properties are investigated in the following. The parameter specific electrical resistance  $\rho$  can be used for an evaluation. In general, the parameter  $\rho$  can be determined by a four-point resistivity measurement [31]. Another method to determine the conductivity  $\sigma$  in the high frequency range is the measurement of the insertion loss of transmission lines. In the second step, the line can be modeled in detail in a simulation software. By variation of the



(a) Photographs of the fabricated CPW transmission lines with different materials.

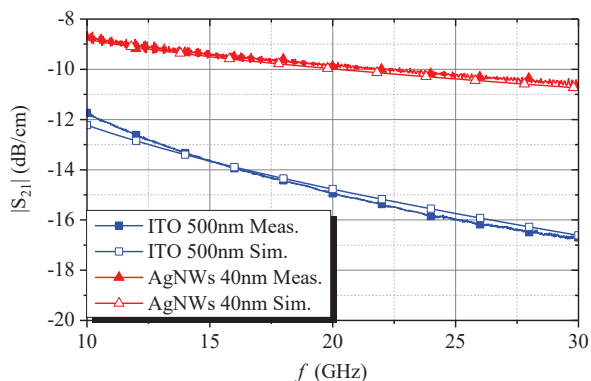


(b) Photograph of the measurement setup and detailed view of the calibration standard line 'Thru' and both measurement tips. [QHD2]

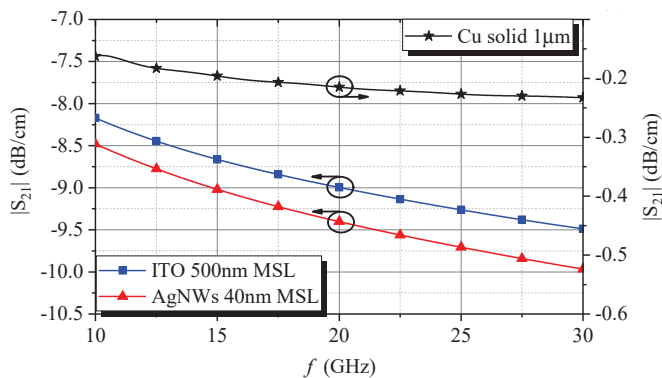
Figure 3.4 Photograph of test structures and measurement setup.

unknown parameter  $\sigma$  an agreement between measurement result and simulation result can be achieved. In this way, the specific resistance can be calculated by knowing the insertion losses of the lossy lines, the dielectric parameters of the substrate and the coating thickness. For these purposes, coplanar waveguide (CPW) transmission lines are utilized due to a simple measurement setup with common Ground-Signal-Ground (G-S-G) measuring tips. The photographs of the fabricated transmission lines are depicted in Fig. 3.4a. In both cases, the transmission line geometry is created by laser ablation. The upper half of the figure shows the transmission lines made of ITO on quartz glass with a thickness of  $h_{\text{sub}} = 0.22$  mm. Due to the in-house fabrication process, the lines made of AgNWs are realized on the RT/duroid 5880 laminate with a thickness of  $h_{\text{sub}} = 0.5$  mm (see lower half of Fig. 3.4a). This carrier material is much easier to handle than thin quartz glass. Fig. 3.4b depicts the measurement setup of a CPW line with one measuring tip on the left hand side and one tip on the right hand side. The copper pads are used only for measurement purposes, otherwise the measuring tips damage the AgNW coating.

In order to determine the propagation constant of the DUTs correctly a TLR (Thru-Line-Reflect) calibration procedure is used. Additionally, the software StatistiCAL from NIST (National Institute of Standards and Technology) is utilized to minimize the measurement uncertainty caused by each measuring step [32]. For this purpose, each transmission line is measured at least three times. The measured results of the CPW transmission lines fabricated with ITO (curve marked with filled squares) and AgNWs (curve marked with filled triangles) are shown in Fig. 3.5a. Here, it should be noted that the lines are realized on different substrates with different thickness and geometry. Modelling the DUTs in a full-wave simulation software Ansys HFSS 17.2 with a conductivity of  $\sigma_{\text{ITO}} = 0.5$  MS/m and  $\sigma_{\text{AgNWs}} = 7$  MS/m results in a good agreement between simulation and measurement (see curves marked with unfilled squares and triangles). Here, the constant coating thickness is assigned as two-sided layered impedance boundaries. By knowing the conductivity value of the investigated materials it is possible to evaluate the insertion loss of other transmission lines e.g. microstrip lines by means of simulation. Fig. 3.5b shows that the insertion loss of the MSL modeled with ITO is  $|S_{21}| = 9.2$  dB/cm and AgNWs is  $|S_{21}| = 9.6$  dB/cm at 24 GHz. Conductors made of AgNWs have higher conductivity value compared to ITO but due to the thinner layer thickness of 40 nm, which is much lower than the skin depth, the MSL designed with AgNWs causes a higher insertion loss than the MSL modeled with ITO. For comparison a conventional MSL with 1  $\mu\text{m}$  thick annealed copper ( $\sigma_{\text{Cu}} = 58$  MS/m) layer has



(a) Simulated and measured results for coplanar waveguide transmission line. Material ITO on quartz glass and AgNWs on RT/duroid 5880 laminate. Line width and gap are slightly different for both DUTs.



(b) Simulated results for microstrip lines ( $Z_0 = 50 \Omega$ ) on quartz glass with a thickness of 0.22 mm.

Figure 3.5 Insertion loss of transmission lines with different electrically conductive materials.

an insertion loss of  $|S_{21}| = 0.2 \text{ dB/cm}$ . The results show that MSL consisting of ITO or AgNWs has significantly higher insertion losses compared to MSL made of conventional metal e.g. copper. This is due to the higher specific resistance values of transparent conductive materials. In the case of an RFID sensor tag, the lower conductivity in turn leads to lower antenna efficiency and higher

insertion losses on the transmission line to the demodulator unit. This leads to a reduction in the achievable communication range, which is undesirable.

An alternative way to obtain both high optical transparency and high conductivity values is the use of grid lines made of conventional metal e.g. annealed copper. Depending on the layout of the grid structures, the thickness of the layer and the material itself the obtained possible sheet resistance is much lower than the value of AgNWs [33]. Several publications e.g. [34–36] have shown that using metal grid lines is a promising approach to realize optically transparent patch antennas and RF circuits.

### 3.3 Microstrip Lines Based on Metal Grid Lines

RF circuits are often implemented on printed circuit board (PCB) using microstrip lines because of the simple fabrication process. The characteristic properties e.g. the impedance and the propagation constant of such transmission lines are well described [56]. When designing optically transparent circuits based on conventional metal (e.g. copper), one approach is to remove some metal area from both the strip line and the ground plane in order to achieve a certain transparency.

In 1983, Rubin and Bertoni [37] carried out investigations on the propagation of waves along an array of conductive strips placed above a periodically perforated ground plane. The purpose of these holes was the realization of interconnections between PCB layers. Different studies on perforated ground planes as well as meshed microstrip lines are listed in Table 3.1. A further motivation for the investigation of a perforation in ground planes of transmission lines is the use of Low Temperature Cofired Ceramics (LTCC) substrates and the applications





Configuration 1	Configuration 2	Configuration 3	Configuration 4
			
[37–42]	[42–46]	[40, 47–52]	[46, 53–55]

Table 3.1 Several studies on perforated ground plane (configuration 1-3) and meshed strip line (configuration 4).

in monolithic microwave integrated circuits (MMICs). Publications listed in the first column of Table 3.1 deal with a configuration where no perforation is allowed directly underneath the strip line. Configuration 2 has a variety of holes in the ground plane. In contrast, the configuration 3 has no metallic area underneath the strip line. In configuration 4 the strip line is perforated while the ground plane is solid.

In order to achieve an optically transparent microstrip line with adequate electrical properties a combination of configuration 2 and configuration 4 is used in this work. A similar configuration has already been utilized in [35], but to the author's best knowledge there cannot be found detailed investigations on the influences of metal grid lines on characteristic parameters of microstrip lines consisting of a meshed strip line as well as a meshed ground plane. Thus, a rule of thumb for the design process or the development step from a non-transparent RF structure to a grid structure would be desirable. At the end of this section, one of the questions to be answered is: How should the grid structure be designed in terms of the area filled with metal in order to obtain the similar impedance value compared to a conventional microstrip line (MSL) with the same outer dimensions? In this way, the design step from a conventional RF circuit to an RF circuit made of grid lines would be significantly simplified. The propagation constant caused by different mesh configurations is also discussed.

### 3.3.1 Determination of Propagation Constant and Characteristic Impedance

The characteristic impedance  $Z_0$  of a microstrip line can be calculated using the approximation formula if the ratio of the line width  $w$  and substrate height  $h$  applies  $w/h \geq 1$  [57]:

$$Z_0 = \frac{120\pi}{\sqrt{\epsilon_{r,eff}}} \left[ \frac{w_e}{h} + 1.393 + 0.667 \ln \left( \frac{w_e}{h} + 1.444 \right) \right]^{-1} \quad (3.1)$$

where

$$\frac{w_e}{h} = \frac{w}{h} + \frac{1.25 t}{\pi h} \left( 1 + \ln \left( \frac{2 h}{t} \right) \right) \quad (3.2)$$

and

$$\epsilon_{r,eff} = \frac{\epsilon_r + 1}{2} + \frac{\epsilon_r - 1}{2} \left( 1 + \frac{12 h}{w} \right)^{-0.5} - \left( \frac{\epsilon_r - 1}{4.6} \frac{t}{h \sqrt{\frac{w}{h}}} \right). \quad (3.3)$$



In addition, the equation Eq. 3.2 applies to  $w/h \geq 1/(2\pi)$ . The parameter  $t$  is the thickness of the metallization. For another ratio of  $w/h$ , other equations must be used. It can be seen that the characteristic impedance  $Z_0$  depends on the dimensions of the microstrip line and the used substrate. The results for  $Z_0$  and  $\epsilon_{r,eff}$  are correct to within 2 percent for the following sets of parameters  $0 \leq t/h \leq 0.2$ ,  $0.1 \leq w/h \leq 20$  and  $\epsilon_r \leq 16$  [57]. A similar approximation formula for a meshed microstrip line could not be found in the literature.

In general, using the basic transmission line theory the determination of the characteristic impedance  $Z_0$  of a transmission line can be explained with reference to the equivalent circuit diagram (see Fig. 3.6). The input impedance of a transmission line can be expressed as follows [58]:

$$Z_a = Z_0 \frac{Z_e + Z_0 \tanh(\gamma l)}{Z_0 + Z_e \tanh(\gamma l)} \quad (3.4)$$

where  $Z_e$  is the load impedance,  $\gamma$  is the propagation constant and  $l$  is the length of the line. At the position  $x = 0$  the input reflection coefficient is:

$$\Gamma = \frac{Z_a - Z_g}{Z_a + Z_g} \quad (3.5)$$

where  $Z_g$  is the source impedance. By substituting equation 3.4 in equation 3.5, the characteristic impedance  $Z_0$  can be determined as follows:

$$Z_0 = -\frac{Z_e(\Gamma - 1) + Z_g(\Gamma + 1)}{2(\Gamma - 1) \tanh(\gamma l)} \pm \frac{\sqrt{(\Gamma(Z_e + Z_g) - Z_e + Z_g)^2 - 4Z_e Z_g(\Gamma^2 - 1) \tanh^2(\gamma l)}}{2(\Gamma - 1) \tanh(\gamma l)}, \quad (3.6)$$

The propagation constant  $\gamma$  can be calculated from the simulated or measured forward transmission of the transmission line if  $Z_0 = Z_e = Z_g$ :

$$S_{21} = e^{-\gamma l} \quad (3.7)$$

$$\gamma = \alpha + j\beta = \frac{-\ln |S_{21}|}{l} + j \frac{2\pi n - \arg(S_{21})}{l}, \quad n \in \mathbb{N} \quad (3.8)$$

Here  $n$  corresponds to the integer multiple of the wavelength. In the case where  $Z_0$  is unequal  $Z_g$  and  $Z_e$ , which is commonly the case of the meshed microstrip

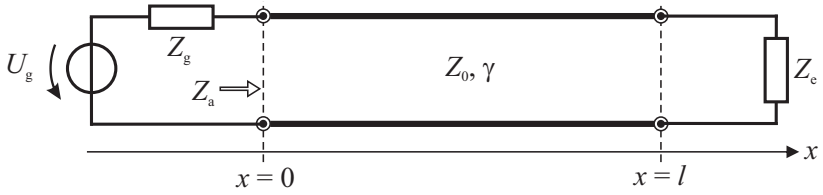


Figure 3.6 Equivalent circuit of a transmission line with termination and generator.

line, the propagation constant  $\gamma$  cannot be calculated according to Eq. 3.7. Thus, a different calculation method must be applied.

Reynoso-Hernandez proposed a method for determining the complex propagation constant of transmission lines with unknown impedance [59]. This method is based on the wave cascading matrix expression of a transmission line having any characteristic impedance. Hence, it is applicable for reflecting and nonreflecting transmission lines. In this work, the line under test is embedded between two sections of microstrip lines with a characteristic impedance value of  $Z_0 = 50 \Omega$ . By knowing the scattering parameters of two lines having the same characteristic impedance but different lengths, the propagation constant  $\gamma$  can be calculated. With this knowledge, the unknown impedance of the transmission line can be determined in the next step. Using Eq. 3.6 the expression  $\tanh(\gamma l)$  is zero if  $\text{Im}\{\gamma l\} = n\pi$  (or  $l = n\frac{\lambda}{2}$ ) and the attenuation constant  $\alpha = 0$ . Thus,  $Z_0$  cannot be calculated correctly in the frequency ranges, in which the length of the investigated line is close to an integer multiple of half the wavelength. Therefore, the computation approach and the calculation equations proposed in [60] is utilized in the following investigations. For the calculation of  $Z_0$  a knowledge of the S-parameter as well as the propagation constant of two transmission lines having the same characteristic impedance and propagation constant, but different lengths is necessary. Therefore, two meshed microstrip lines are modeled in a full wave simulation software to compute the needed S-parameter. A detailed configuration of the meshed MSL is described hereafter.

### 3.3.2 Influence of Grid Lines on Characteristic Parameters

The determination of the characteristic impedance  $Z_0$  of meshed microstrip lines becomes increasingly difficult with increasing complexity of the structure. The less metallic area of a meshed microstrip line (MSL) is present the higher is

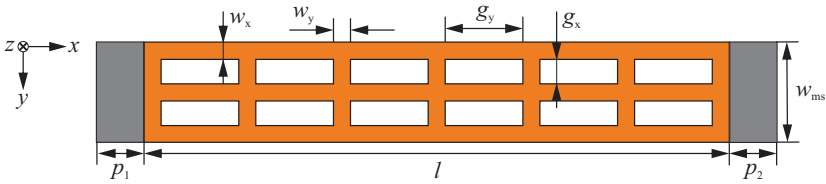


Figure 3.7 Layout of a meshed MSL with the length  $l$ , number of grid lines  $n_x = 3$ ,  $n_y = 7$  and additional parts  $p_1 = p_2 = 0.25$  mm in order to ensure the excitation of the fundamental mode in the software Ansys HFSS. [QHD1]

the deviation from the electromagnetic field distribution of a conventional MSL. Therefore, a line impedance  $Z_0$  of an MSL based on grid lines is determined in this work. It should be mentioned here that a constant characteristic impedance is assumed for the meshed MSL.

Fig. 3.7 depicts the layout of a meshed microstrip line with its geometric parameters. In order to study fundamental influences of the grid geometry on the characteristic electrical properties of the MSL and to keep the design process as simple as possible, grid structures with uniform gaps in x-direction and y-direction are investigated. Hence, three parameters can be defined as follows:

$$MeshFactor_x = \frac{n_y \cdot w_y}{l} \quad (3.9)$$

$$MeshFactor_y = \frac{n_x \cdot w_x}{w_{ms}} \quad (3.10)$$

$$MeshFactor_A = MeshFactor_x + MeshFactor_y - \frac{w_y \cdot w_x \cdot n_y \cdot n_x}{l \cdot w_{ms}} \quad (3.11)$$

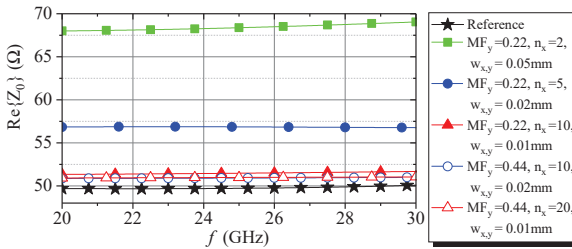
$MeshFactor_x$  ( $MF_x$ ) and  $MeshFactor_y$  ( $MF_y$ ) represent the filling factor (area covered with metal) in a particular direction in space, while  $MeshFactor_A$  ( $MF_A$ ) is the ratio of the filled area to the total area of a conventional MSL with identical outer dimensions. The transparency  $T$  can be calculated by  $1 - MeshFactor_A$  without taking into account physical phenomena such as reflection, diffraction, etc..

In the following, the investigations of meshed MSLs are carried out based on simulation models. Here, quartz glass with a thickness of  $h_{sub} = 0.22$  mm

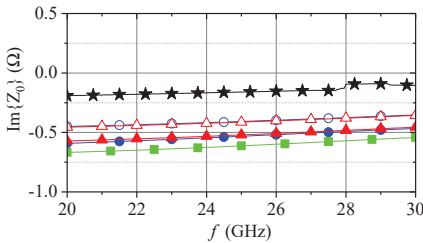
is utilized since it will be used as carrier material for the analog front-end. Its dielectric parameters  $\epsilon'_r = 3.81$  and  $\tan \delta = 0.0004$  at  $f = 24$  GHz are determined by an open resonator measurement method. The open resonator used is the Model 600T from Damaskos, Inc [61]. Based on these material properties, the dimension of a conventional MSL results in a line width of  $w_{\text{ms}} = 0.46$  mm for a line impedance of  $Z_0 = 50 \Omega$  at  $f = 24$  GHz. In this case, the imaginary part of  $Z_0$  can be neglected. The width of the substrate is set to  $w_{\text{sub}} = 5$  mm which is greater than  $10 \cdot w_{\text{ms}}$ . In order to ensure an excitation of the fundamental microstrip line mode at both ports in the simulation software Ansys HFSS, a small part of a conventional microstrip line is added at the beginning and the end of the line (see Fig. 3.7,  $p_1$  and  $p_2$ ). The length of the first meshed MSL is defined as  $l_1 = 2$  mm in order to avoid long simulation times. The second line can have any different length but the grid spacing should be maintained. Thus, this length is set to  $l_2 = 2 l_1 - w_y$ . It should be mentioned that the length of both lines is less than one wavelength, but the chosen length has no influence on the result. The conductive layer is modeled as two-sided layered impedance boundaries with a conductivity of  $\sigma = 58$  MS/m (annealed copper) and a thickness of  $t = 1 \mu\text{m}$  that is approx. 2.4 times larger than the skin depth.

### 3.3.2.1 Meshed Strip Lines over Solid Ground Plane

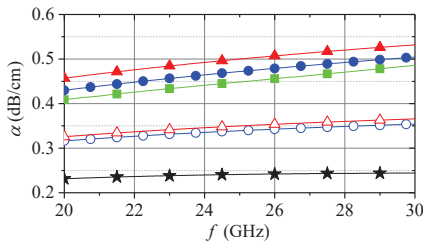
First, the influences of meshing the strip lines over a solid ground plane are investigated. Fig. 3.8a and 3.8b show the characteristic impedance determined by the calculation method described in [60]. Three different grid line width  $w_x$  and  $w_y$  (0.05 mm, 0.02 mm and 0.01 mm) with several *MeshFactor* are studied but to keep the diagram clear, only configurations with low *MeshFactor* are shown. Furthermore, they represent the main findings. At first, the influence of grid lines in  $x$ -direction is studied. In the following, the values for  $n_y$  (e.g.  $n_y = 3$ ,  $g_y \approx 0.076 \lambda_0$  at  $f = 24$  GHz) refer to the meshed microstrip lines with the length of  $l_1 = 2$  mm. For comparison, both curves marked with stars depict the impedance of a conventional  $50 \Omega$  microstrip line. Using a *MeshFactor<sub>y</sub>* of  $MF_y = 0.22$  with a grid line width of  $w_{x,y} = 0.05$  mm and  $w_{x,y} = 0.02$  mm the real part of the impedance is roughly  $68 \Omega$  and  $57 \Omega$ , respectively. These higher characteristic impedance values are caused by the structure (in this case: four-wire arrangement) that has a high even mode impedance. In order to obtain a meshed  $50 \Omega$  microstrip line additional grid lines can be used while keeping the width  $w_{\text{ms}}$  constant (decrease of the gap  $g_x$ ). Increasing the width  $w_{\text{ms}}$  would also reduce the impedance, but this would lead to a larger space consumption on



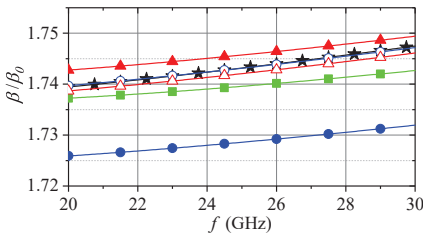
(a) Real part of the characteristic impedance.



(b) Imaginary part of the characteristic impedance.



(c) Attenuation constant.



(d) Normalized phase constant.

Figure 3.8 Simulated characteristic properties of the meshed microstrip lines ( $n_y = 3$ ) with conventional ground plane. Legend applies to all graphs. [QHD1]

the circuit board. The curve marked with unfilled circles depicts the impedance of a configuration with  $MF_y = 0.44$ . In this case, the real part of the characteristic impedance is  $\text{Re}\{Z_0\} \approx 50 \Omega$ . To increase the transparency, a smaller grid line width of e.g.  $w_{x,y} = 0.01$  mm can be used and the impedance is still preserved (see curves marked with filled and unfilled triangles). For all configurations investigated, the imaginary part of the impedance is nearly zero.

Fig. 3.8c shows the real part of the propagation constant. A conventional MSL (identical dielectric material and outer dimensions) has an attenuation value of  $\alpha = 0.24$  dB/cm at  $f = 24$  GHz. It can be observed that the thinner the grid line width the higher the attenuation constant. This dependency is caused by the metallic losses. A doubling of the parameter  $MF_y$  from  $MF_y = 0.22$  to  $MF_y = 0.44$  leads to a decrease of the attenuation value by the factor of approx. 1.4. Obviously, an further increase in  $MF_y$  results in a lower attenuation constant which converges to the value of a conventional microstrip line. Fig. 3.8d depicts the phase constant  $\beta$  normalized to the phase constant in free space  $\beta_0$ . It can be noted that the imaginary part of the propagation constant of the meshed microstrip lines does not show significant deviation from the values of the reference line.

Fig. 3.9 depicts the influence of grid lines perpendicular to the direction of wave propagation in the first instance. The configuration with a grid line width of  $w_{x,y} = 0.02$  mm was selected as an example. An increase of the parameter  $n_y$  by a factor of ten and thus an increase of the  $MeshFactor_A$  from  $MF_A = 0.24$  to

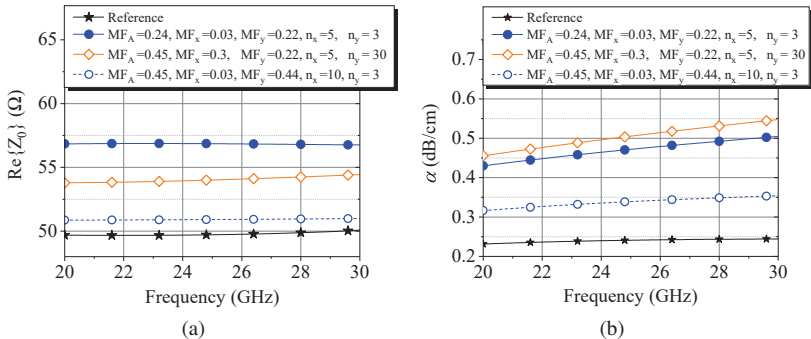


Figure 3.9 Comparison of the influence of grid lines perpendicular and parallel to the direction of wave propagation for configurations with  $w_{x,y} = 0.02$  mm. (a) Real part of the characteristic impedance. (b) Attenuation constant. [QHD1]

$MF_A = 0.45$  leads to a decrease of the real part of the characteristic impedance by 5.3 % (cf. curves marked with filled circles and rhombuses). Meanwhile, no reduction of the attenuation values can be achieved. In order to compare these results with the previous investigations of the grid lines arranged parallel to the direction of wave propagation the curves with unfilled circles from Fig. 3.8 are plotted again in Fig. 3.9. Comparing both curves with the same *MeshFactor*<sub>A</sub> of  $MF_A = 0.45$  it can be concluded that using a large number of grid lines perpendicular to the direction of wave propagation is an inefficient way to lower both the characteristic impedance as well as the attenuation constant.

### 3.3.2.2 Solid Strip Lines over Meshed Ground Plane

In analogy to the previous section, the influences of meshing the ground plane are investigated while the strip line is solid (cf. configuration 2 in Table 3.1). In this case, a periodic structure consisting of grid lines in  $x$ - and  $y$ -direction is applied (cf. Fig. 3.7). The outcomes indicate similar tendencies and characteristics as for the meshed strip line over a solid ground plane (see 3.3.2.1). Thus, the results obtained are not presented in detail. It was also found out in [42–45, 47, 49–51] that the smaller the gap between adjacent grid lines (higher values of  $MF_A$ ) the lower the real part of  $Z_0$ .

### 3.3.2.3 Meshed Microstrip Lines

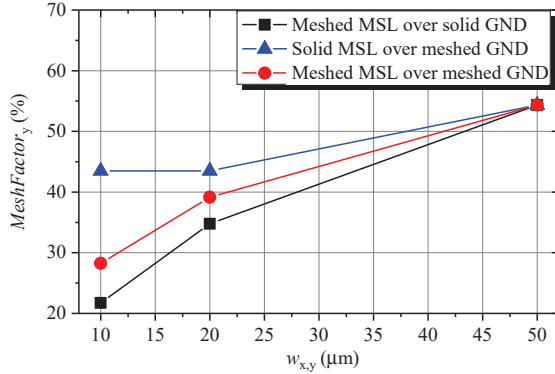
In this investigation, the same grid structure is applied to both the meshed MSL and the meshed GND. Hence, the grid lines on the top layer are located exactly above the grid lines on the bottom layer resulting in a higher transparency value compared to the case of misalignment between both layers. When developing RF circuits using microstrip line technology, the typical design flow is based on an analytical description of a conventional line segment, for example an MSL. Therefore, it is important to know the characteristic impedance  $Z_0$  and the propagation constant  $\gamma$  of the individual microstrip line section. Thus, there is an interest in knowing the relationship between both parameter mentioned and the minimum *MeshFactor*<sub>A</sub> of a meshed MSL in order to imitate a conventional MSL with the same outer dimensions. Correcting the impedance value by increasing the width  $w_{ms}$  would result in a low optical transparency and a higher space consumption for the whole RF circuit.

In order to obtain a clear overview all configurations from the investigations are selected which fulfill the following condition within the considered frequency

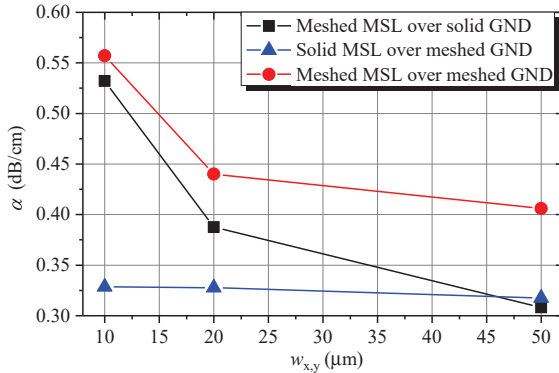
range:

$$50 \Omega \leq \operatorname{Re}\{Z_0\} \leq 52.5 \Omega. \quad (3.12)$$

This corresponds to a maximum deviation of 5% from the impedance value of a conventional microstrip line with  $Z_0 = 50 \Omega$ . Fig. 3.10a depicts those values of  $\text{MeshFactor}_y$  as a function of the grid line width  $w_{x,y}$  for three different configurations. The figure of merit  $MF_y$  is selected since investigations carried



(a)



(b)

Figure 3.10 (a)  $\text{MeshFactor}_y$  ( $MF_y$ ) as a function of the grid line width  $w_{x,y}$  in order to imitate the impedance value  $Z_0$  (up to +5% deviation) of a conventional MSL with identical dimension  $w_{\text{ms}}$  and (b) the corresponding attenuation constants.  $n_y = 3$  for all configurations. [QHD1]



out previously show that grid lines parallel to the direction of wave propagation have the highest impact on the impedance as well as the attenuation constant. Here, the parameter  $MF_y$  refers to the width  $w_{ms}$ . The corresponding attenuation constants are shown in Fig. 3.10b. In conclusion, using a small grid line width in the range of  $w_{x,y} \approx 0.01$  mm is the most efficient way to imitate the impedance of a conventional MSL. But in contrast the attenuation constant increases with a decrease of the  $MeshFactor_y$ . Concerning the phase constant  $\beta$  it can be stated that the deviation from the value of the reference line is very small. Therefore, these results are not shown.

The investigations in this section only refer to a  $50\ \Omega$  microstrip line on a specific substrate material. The minimum  $MeshFactor_y$  cannot be applied directly to a microstrip line with another characteristic impedance value or to a  $50\ \Omega$  microstrip line on any RF laminate. Nevertheless, these values can be used as a starting point for the design of the grid structure even if other line impedances are used in the circuit. In the next step, a further optimization process of the grid structure of an RF circuit is necessary. In addition, the relationship between the direction of wave propagation and the orientation of the grid lines should be considered. The grid lines should be oriented to the electric current direction of the desired fundamental mode. The described design procedure simplifies the conversion of an opaque circuit into a meshed circuit without changing the outer geometry of a line section.

### 3.4 Conclusion

The main results of the investigations of optically transparent materials are:

- Optically transparent materials such as Indium Tin Oxide (ITO) or silver nanowires (AgNWs) have a low conductivity value compared to conventional metal e.g. copper. This in turn leads to higher insertion losses of a transmission line. For comparison, at 24 GHz the insertion loss  $|S_{21}|$  of an investigated microstrip line made of ITO, AgNWs and metal grid lines are  $|S_{21}| = 9.2$  dB/cm,  $|S_{21}| = 9.6$  dB/cm and  $|S_{21}| = 0.5$  dB/cm, respectively. Thus, RF circuits and antennas should be designed with grid line structures to achieve both optical transparency and efficiency as high as possible.
- Different grid line width and spacing between the grid structures are studied concerning the propagation constant and the characteristic impedance

of the microstrip line. The orientation of the grid lines should be arranged parallel to the electric current direction in order to imitate the characteristics of a conventional (non-transparent) microstrip line in the best possible way.

- For a specific configuration of a microstrip line with a given permittivity and geometric dimensions, the area filled with metal in a particular direction in space ( $MeshFactor_x$ ,  $MeshFactor_y$ ) as a function of the grid line width is determined. The minimum  $MeshFactor_y$  is used as a starting point for the design of a meshed circuit. Thus, the design step from a conventional circuit to a circuit with grid structures can be simplified.

# Antenna and Analog Front-End Based on Metal Grid Lines

Based on the findings of the characteristic impedance and propagation constant of meshed microstrip lines discussed in Sec.3.3, an antenna and an analog front-end are designed in this chapter. Both units are an important part that significantly determines the properties of the tag. Depending on the application scenario, there are different requirements on the antenna design as well as the RF circuit. In this work, both units should allow an integrability in metallic objects and an ease of integration on a commercially available solar cell without influencing it significantly. Regarding the antenna, there are multiple approaches for a combination of optical power supply and wireless data transmission. One possibility is the use of slot antennas, which are directly integrated in a solar panel [62–66]. Here, a modification of the solar panel is necessary. Another approach is to place an optically transparent patch antenna on the solar panel [67–69]. In this case, the patch antenna should not shade the underlying solar cell significantly to ensure its functionality. The latter approach is considered in this work. Furthermore, the RF connection between the antenna and the analog front-end should have low losses and be designed as simple as possible. For this reason, the antenna and the analog front-end is positioned on the same layer to keep the length of the transmission line to a minimum. Thus, investigations on optically transparent antenna and analog front-end are needed. In this work, a circularly polarized square patch antenna is utilized which is fed by a microstrip line as well as a modulator and demodulator circuit. The final layout is shown in Fig. 4.1. The top layer is depicted on the left-hand side while the ground plane is illustrated on the right-hand side. In order to develop this structure the properties of the antenna as well as the RF circuit are studied separately.

Sec. 4.1 deals with the design of meshed patch antennas. The influences of the grid lines on the antenna characteristics are discussed. The impact of the solar cell on the antenna properties are studied too. With the knowledge gained from simulations and measurements an optimized antenna is designed. The developed meshed antenna structure and its characteristics are presented at the end of this section followed by a short conclusion.

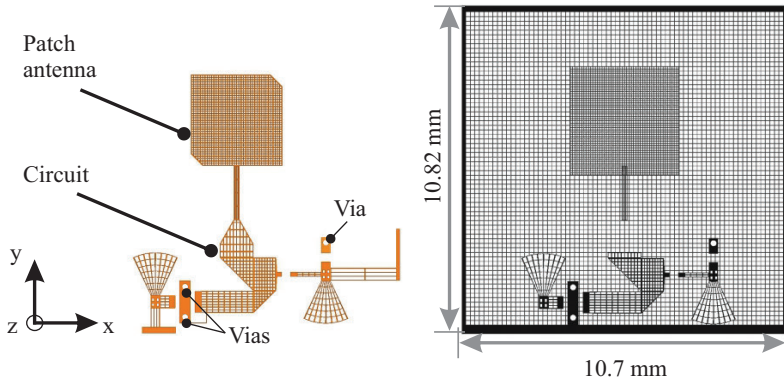


Figure 4.1 Layout of the designed analog front-end based on metal grid lines. Top (left) and bottom (right, GND) layer. [QHD1]

The next Sec. 4.2 presents the development of the analog front-end. In the first step, the concept of the modulator and demodulator unit is introduced. Afterwards, a reference circuit consisting of a modulator and demodulator circuit is designed. It will be used as a starting point for the development of an optically transparent circuit based on metal grid lines. The characteristics of the designed circuits are presented and discussed in the respective subsections. A brief conclusion of the achieved results is given at the end of this section.

The last two sections Sec. 4.3 and Sec. 4.4 deal with the used fabrication process to obtain the antenna and the analog front-end and a possibility to determine the optical transparency of the whole unit.

## 4.1 Patch Antenna Design

The patch antenna is commonly referred to as microstrip antenna. Its advantage lies mostly on the easy, low cost and low profile fabrication on a printed circuit board. Other advantages include the possibility of automated mass production, high mechanical stability and small size. An example of a patch antenna fed by a coaxial feed is shown in Fig. 4.2. A patch antenna generally consists of an arbitrarily shaped metallic conductor arranged on a grounded dielectric laminate. The length  $l_{Patch}$  of the resonant radiator should be approximately  $l_{Patch} = \lambda_g/2$  whereby  $\lambda_g$  is the guided wavelength taking into considerations

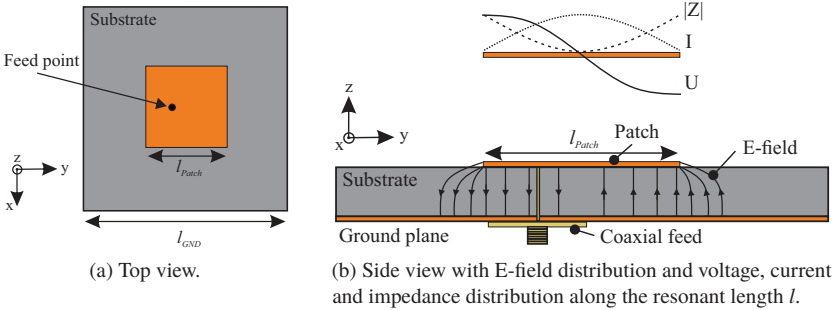


Figure 4.2 Structure of a square patch antenna

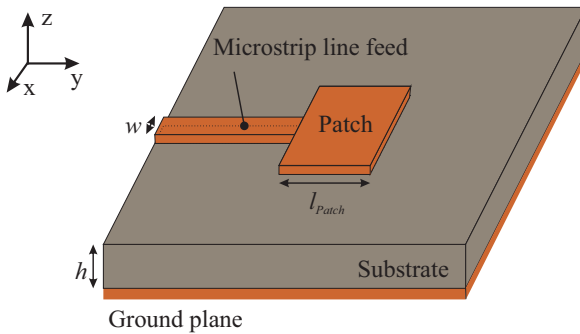


Figure 4.3 3D model of a patch antenna fed by a microstrip line.

the surrounding environment of the antenna. Fig. 4.2b depicts the side view of a patch antenna including the electric field. The voltage, current and impedance distribution along the resonant length  $l$  are also shown. It can be noted, that the impedance  $|Z|$  has the maximum values at the edges of the patch and a minimum value at the center of the patch. Using the coaxial feed method the inner conductor is connected to the radiating patch whilst the outer conductor is connected to the ground plane. Its advantage lies on a simple impedance matching method and low spurious radiation of the feed. The location of the feed point is determined for a given mode in order to achieve a best impedance match.

Other feeding methods are proximity-coupled feed and aperture-coupled

feed [22]. The main drawback of these methods is the need of a multilayer design. This in turn leads to a higher complexity in the technological feasibility, such as additional effort in the structuring of the conductive lines and the mechanical connection of the glass substrates as well as an exact alignment of the layers to each other. Furthermore, the optical transparency of the arrangement decreases, which has a negative effect on the energy yield of the underlying solar cell. A promising feeding method suitable for the design concept of the RFID sensor tag is the microstrip line feed. In this case, a microstrip line is directly connected at a radiating edge of the antenna (see Fig. 4.3). The impedance matching can be realized by the variation of the line width  $w$  or by an impedance matching network based on the microstrip line technology. Here, radiation effects produced by discontinuities in microstrip line is expected, which could have a negative influence on the radiation characteristics of the antenna. Nevertheless, this feeding method is used because of the simple realization of the signal routing between RF circuit and antenna.

#### 4.1.1 Impact of Grid Lines

In order to design an optically transparent patch antenna based on metal grid lines, its impact on the antenna characteristics is studied. An own preliminary investigation has been carried out in [QHD6]. The results have shown that the grid lines should be oriented to the electric current direction of the desired resonant mode. This finding confirms the guideline, which is also documented in the literature [67, 70]. In the following, an investigation is carried out for a patch antenna operating at 24 GHz. Additionally, the metal losses are taken into account.

Fig. 4.4 depicts the geometries of a meshed square patch and the top view of an example configuration of a conventional (solid) patch over meshed ground plane. In analogy to the investigation of the meshed microstrip lines (see subsection 3.3.2 and Fig. 3.7), the square patch as well as the ground plane are divided in strips orientated in  $x$ - and  $y$ -direction. The parameters  $w_{x,y}$  and  $g_{x,y}$  are grid line width and grid spacing, respectively. The following investigations are carried out using the 3D full-wave simulator software Ansys HFSS. The geometrical outer dimension of the radiating square patch is fixed to  $l_p = 3.03$  mm while the length of square ground plane is  $l_{\text{GND}} = 10$  mm. In this case, quartz glass ( $\epsilon'_r = 3.81$  and  $\tan \delta = 0.0004$  at 24 GHz) with a thickness of 0.22 mm is used. As in Sec. 3.3.2, the grid lines are modeled as two-sided layered impedance boundaries with a conductivity of 58 MS/m (annealed copper) and a thickness

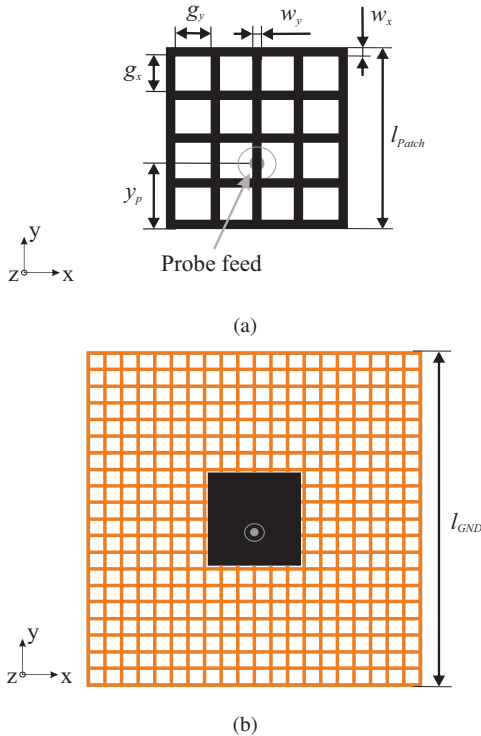


Figure 4.4 (a): Dimensions of a meshed square patch with  $n_{x,y} = 5$ . (b): An example configuration of a conventional patch (black colored) over meshed ground plane (orange colored) with  $n_{x,y} = 21$ .

of  $1 \mu\text{m}$ . For these fundamental studies a coaxial probe with a characteristic impedance of  $Z_{Coax} = 50 \Omega$  is used to feed the antenna.

First, the radiating element of the microstrip patch antenna is meshed. The number of grid lines  $n_x = n_y$  is fixed, since the antenna to be finally designed should provide a circular polarization. The line width is varied in an interval from  $w_x = w_y = \frac{l_{Patch}}{n_{x,y}}$  ( $MeshFactor_A = 1$ ) down to  $w_{x,y} = 0.01 \text{ mm}$ . Several variations of the grid number  $n_{x,y}$  are studied but to keep the diagram clear three configurations representing the main findings are shown. Fig. 4.5a and 4.5b depict the influence of the grid line width on meshed patch antennas over solid ground plane. The resonance frequency  $f_r$  and the resulting bandwidth

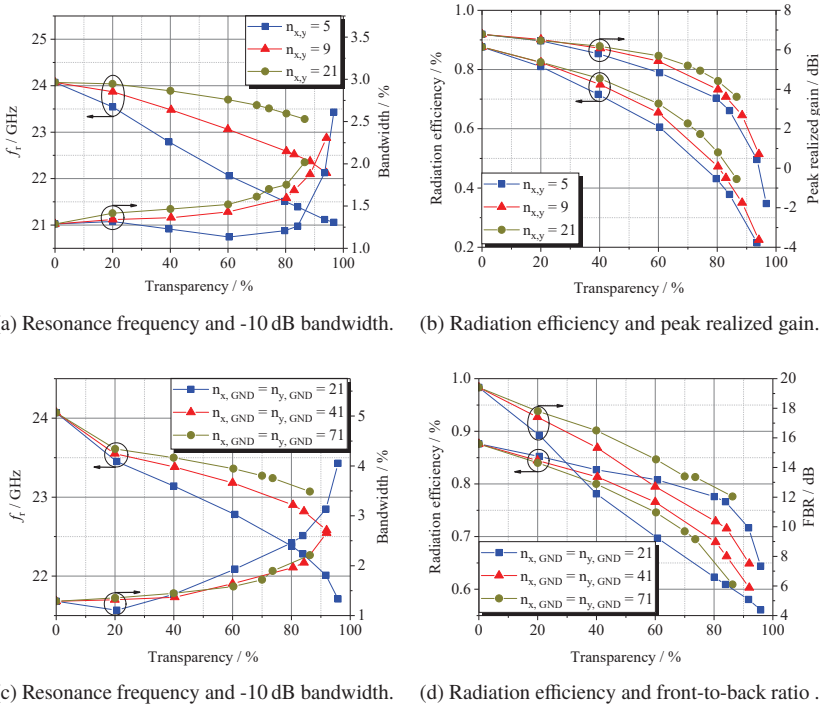


Figure 4.5 Influence of the grid line width on antenna characteristics as a function of transparency ( $1 - MeshFactor_A$ ), (a) - (b): meshed patch over solid GND, (c) - (d): solid patch over meshed GND

(input reflection coefficient  $|S_{11}| \leq -10$  dB) are shown in Fig. 4.5a. It can be seen that the smaller the grid line width the lower is the resonance frequency. This effect is even greater when the number of grid lines is smaller. The reason for this characteristic can be explained by a detailed analysis of the current density distribution on the patch surface (see Fig. 4.6a-4.6b). The plots of the current density distribution show that the currents flow along both vertical and horizontal lines. Thus, it results in longer current paths (from the lower to the upper radiating edges) and the resonance frequency is lower compared to a solid patch if the width of the grid line is decreased (for the same number of grid lines) or if the number of grid lines is reduced (for the same grid line width). This



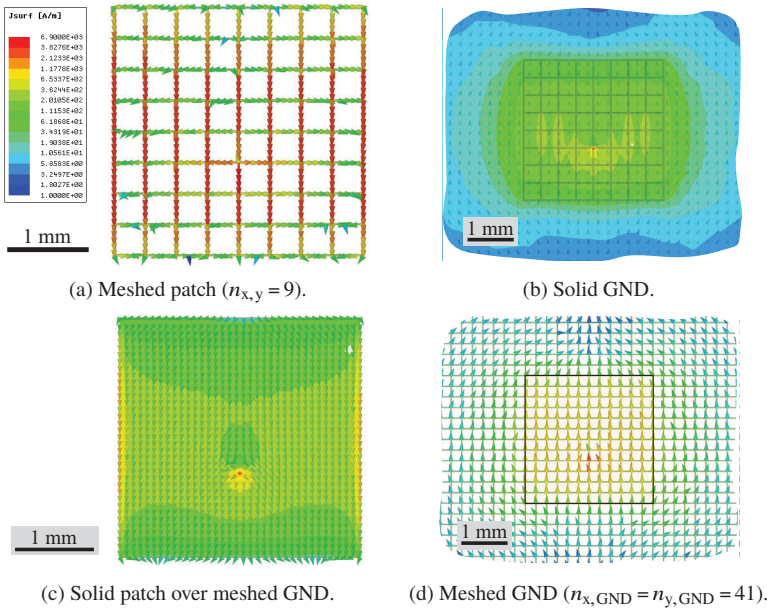


Figure 4.6 Current density distribution of (a) - (b): meshed patch over solid GND and (c) - (d): solid patch over meshed GND. Color scaling applies to all figures.

finding shows that the overall dimension of a meshed antenna can be reduced for a given operating frequency. Furthermore, it can be observed that the bandwidth is increasing for most configurations. This characteristic can be explained by considering the radiation efficiency of the antenna (see Fig. 4.5b). The smaller the grid line width, the lower the radiation efficiency. The increasing metal losses of the antenna lead to an increase in bandwidth. By meshing the patch, both the radiation efficiency and the peak realized gain decrease.

In the second step, the patch is modeled as solid in order to study the effects caused by meshing the ground plane on the antenna characteristics. In analogy to the previous investigation simulation results of three different configurations are shown in Fig. 4.5c and 4.5d. Again, the number of grid lines  $n_{x,GND} = n_{y,GND}$  is fixed and the line width is varied in an interval from  $w_{x,GND} = w_{y,GND} = \frac{l_{GND}}{n_{x,GND}; y,GND}$  ( $MeshFactor_A = 1$ ) down to  $w_{x,y} = 0.01$  mm.

As expected, the resonance frequency decreases and the bandwidth increases

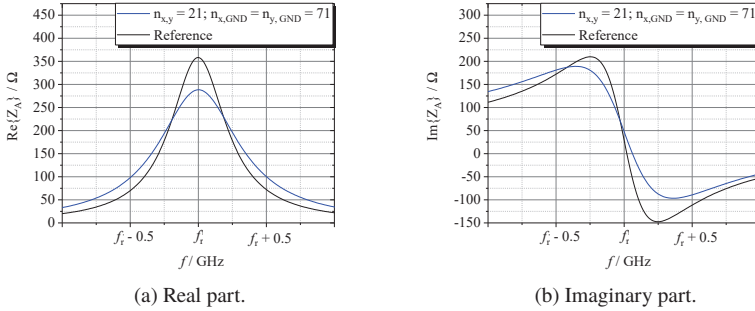


Figure 4.7 Antenna impedance  $Z_A$  as a function of the frequency for an example configuration. Feed point at a radiating edge.

with increasing spacing between grid lines. This correlation is more pronounced the less number of grid lines are used. The radiation efficiency decreases with decreasing  $\text{MeshFactor}_A$  due to losses caused by the grid structure. Furthermore, a change of the value of the front-to-back ratio (FBR) can be noted. A grid that is not close-meshed leads to a radiation to the back of the patch antenna and thus reduces the antenna gain value. In the latter design of the RFID sensor tag, a solar cell is located on the back of the antenna. For this reason, the influence of the solar cell on the antenna characteristics is studied in more detail in section 4.1.3.

In order to obtain comparable simulation results the position of the probe feed  $y_p$  (cf. Fig. 4.4a) is varied in each configuration to achieve a good impedance matching ( $|S_{11}| \leq -20$  dB). It is found that an increase of the transparency leads to a lower input resistance, which has to be compensated by different feed point positions. For this reason, the antenna impedance  $Z_A$  is considered. Fig. 4.7 depicts the real part and the imaginary part of an example configuration of a meshed patch antenna as a function of frequency. The impedance values of a conventional patch antenna with the same dimensions are plotted in the same graph. Here, both antennas are fed at the edge using a lumped port. It can be observed that the real part of the impedance of the meshed antenna is 20 % lower than the value of a conventional patch antenna at the resonance frequency  $f_r$ . Hence, feeding a meshed patch antenna by using a microstrip line is simpler compared to a conventional patch antenna due to the lower antenna impedance. In this case, the microstrip line could be connected directly to one edge of the

patch for impedance matching. A higher impedance value of a microstrip line requires a smaller line width (assuming that all other parameters remain the same), which can lead to a challenging demand on the fabrication process.

### 4.1.2 Circularly Polarized Patch Antenna

By definition, the electric field vector represents the polarization of an electromagnetic wave [71]. The general type of polarization is elliptical polarization, i.e. the end point of the electric field strength vector moves along an ellipse. If the vector only moves along a line, this is referred to as linear polarization. A linear polarized wave can again be divided into two cases. If a wave has only one E-field component that is parallel to the earth's surface, it is polarized horizontally. Vertical polarization occurs when the electric field vector is perpendicular to the earth's surface. Another special form of elliptical polarization is circular polarization. Here, the vector of the electric field strength rotates in a circle along the direction of propagation. An important parameter to describe the quality of the polarization is the axial ratio (AR). The axial ratio describes the dependence of the co-polar component of the electric field - the desired type of polarization - to the cross-polar component, which is orthogonal to it. In case of linear polarization, the axial ratio value is infinite or zero. If an axial ratio is unity, a perfect circular polarization is achieved.

There are many possibilities to design circularly polarized patch antennas. In general, there is need to generate two different modes of equal magnitude and  $90^\circ$  out of phase from each other. An antenna is said to be circularly polarized if, in a particular direction in the far zone, the field is circularly polarized at a certain

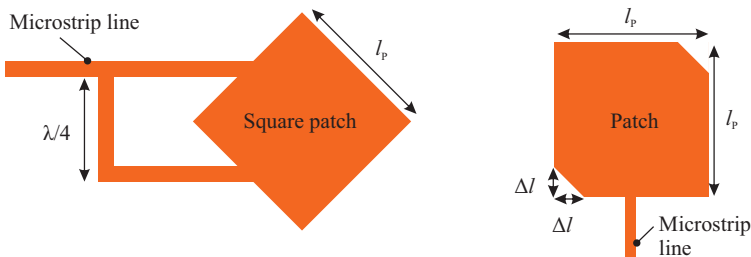
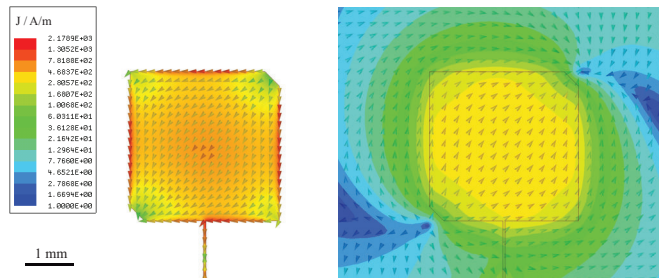


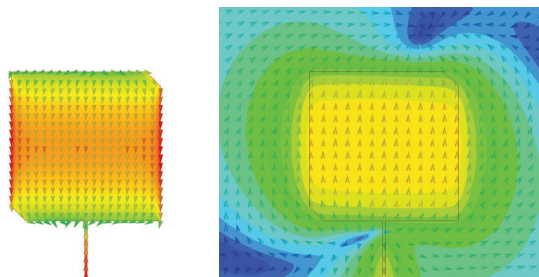
Figure 4.8 Two example methods for generating circular polarization with a single patch antenna. Left: Square patch fed at adjacent edges. Right: Square patch with truncated corners fed by a single microstrip line.

frequency. In order to obtain circular polarization two common methods can be applied to a single patch: dual feed method and single feed method with shape modifications. An example of such arrangement is shown in Fig. 4.8. On the left hand side, a square patch antenna is fed at adjacent edges by two microstrip lines. The dual feed method excites two orthogonal modes using separate feeds and ensuring a  $90^\circ$  phase difference between the modes by incorporating a  $90^\circ$  phase shift within one of the feed lines.

The other possibility is using a single feed to generate two orthogonal modes. Therefore, a perturbation segment such as a slot or other truncated segment methods can be utilized [72]. In this work single fed truncated corners patch antennas (see Fig. 4.8 right) are investigated because of its simple feeding method.



(a) Phase value of  $0^\circ$  at excitation port, left: radiating patch, right: ground plane.



(b) Phase value of  $45^\circ$  at excitation port, left: radiating patch, right: ground plane.

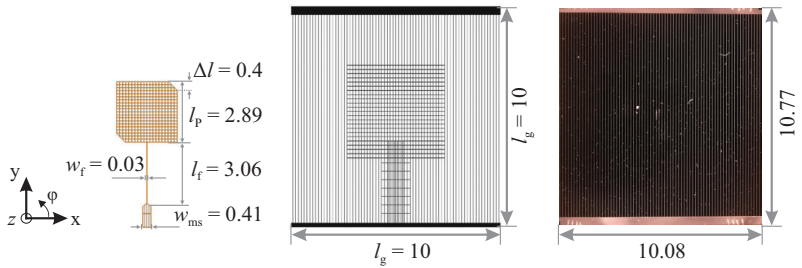
Figure 4.9 Current density distribution of an RHCP patch antenna fed by a microstrip line. Color scaling applies to all figures.

In this case, the lower left corner and the upper right corner are truncated to obtain right hand circular polarization (RHCP). Here, the electric field vector of the traveling wave rotates in a right-hand sense in relation to the direction of propagation. This behavior can be seen from the current density distribution that is depicted in Fig. 4.9. Two states are shown for clarification purposes: phase value of  $0^\circ$  and  $45^\circ$  at the excitation port .

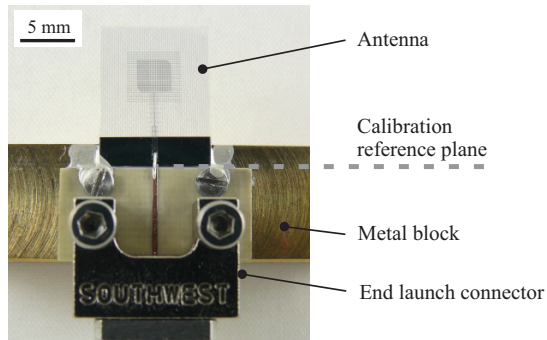
In a preliminary study published in [QHD5], a circularly polarized patch antenna consisting of grid lines was investigated. The truncated corner patch antenna is fed by a microstrip line. This study included an evaluation of the antenna impedance and the influence of misalignment (translation and rotation) between the top and bottom layer on the antenna characteristics. The simulated and measured results indicated a promising approach. A slight misalignment during the fabrication process will not influence the antenna performances significantly. Thus, an optically transparent square patch antenna with truncated corners fed by a single microstrip line is investigated in the following.

### 4.1.3 Influence of a Solar Cell on Antenna Characteristics

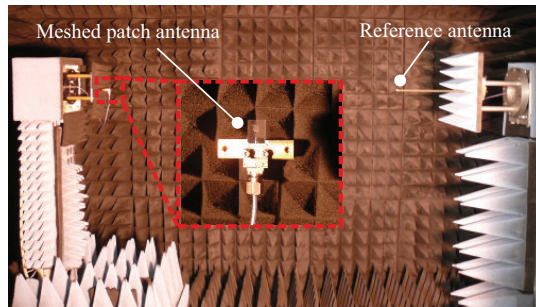
Patch antennas made of metal grid lines are already studied e.g. in [34–36] and they show a suitable performance to fulfill the requirements of the integration in a compact RFID sensor tag. When positioning a meshed patch antenna on a commercial solar cell the layer composition of the solar cell should be well known, since the solar cell has an impact on the antenna characteristics as shown in [67, 73]. In this work, a triple junction solar cell [24] from Spectrolab is used which is shown in Fig. 4.10a on the right. From the bottom to the top it consists of a metal backing layer, photovoltaic layer and electrode fingers (parallel lines oriented in  $y$ -direction) made of silver. Since the pitch and the width of the fingers is about 0.14 mm and  $10\ \mu\text{m}$ , respectively, the vertical grid lines of the meshed ground plane are first designed with the same geometry. The corresponding  $MeshFactor_{x,GND}$  is  $MF_{x,GND} = 0.073$ . Hence, it can be figured out whether the fingers of the solar cell (see bottom layer in Fig. 4.10a, grid lines in  $y$ -direction) can be used as part of the antenna ground plane. If yes, the grid lines in  $y$ -direction can be omitted and therefore only grid lines in  $x$ -direction need to be structured on the glass substrate. This would increase the transparency of the RF unit, which is desirable. Due to the high field strength in the area of the patch, additional horizontal grid lines are added to the ground plane in the region under the radiating element (see Fig. 4.10a, right). The gap between these horizontal grid lines is set to 0.18 mm and the grid line width



(a) Left: top layer. Center: bottom layer. Right: photograph of the solar cell. All dimensions in mm.



(b) Antenna mounted on a metal block for measurement purposes.



(c) Measurement setup in an anechoic chamber.

Figure 4.10 Layout and photograph of the realized meshed patch antenna as well as a photograph of the used solar cell.

is 0.02 mm. In order to excite the two orthogonal modes in the best possible way, the grid structure of the patch should be symmetrical. Here, an equal pitch of 0.124 mm and a grid line width of 0.02 mm are chosen. These geometries are selected to achieve an antenna gain value better than 3 dBi. Furthermore, it should be mentioned that this antenna is used as a test structure to investigate the influence of the solar cell. Thus, the grid structures are chosen differently to identify unwanted impacts. The antenna is fed by a meshed microstrip line with a line width of  $w_{ms} = 0.41$  mm and a second microstrip line with  $w_f = 0.03$  mm. The latter is for impedance matching between the antenna and a  $50\ \Omega$  microstrip line, which is needed for measurement purposes. In the area underneath the meshed microstrip line, the grid line gap in  $y$ -direction is 0.07 mm while the spacing between the grid lines in  $x$ -direction is 0.4 mm. Fig. 4.10b shows a photograph of the fabricated antenna and the auxiliary construction. This setup is used for measurement purposes. The  $50\ \Omega$  microstrip line of the antenna is connected with the  $50\ \Omega$  microstrip line of a PCB (Rogers Corporation 4003C, 0.2 mm thickness) via conductive adhesive while the end launch connector is attached on the PCB. A TLR calibration process is utilized for the S-parameter measurement.

Fig. 4.11 depicts the comparison of simulation and measurement results. As can be seen from Fig. 4.11a a resonance frequency shift of 0.16 GHz occurs between the simulated and measured results for an antenna without solar cell on the back side. This corresponds to a deviation of 0.7%. By mounting the solar cell on the back of the antenna the measured resonance frequency is shifted by 0.29 GHz. Based on this knowledge and further simulation of the antenna with the solar cell, the conductivity of the photovoltaic layer can be assumed to be  $\sigma_{sc} = 10\ \text{kS/m}$  (to obtain the same frequency shift). Furthermore, it can be observed that the presence of the solar cell leads to a resonance frequency shift to higher frequencies. This behavior is already known from Sec. 4.1.1 since the fingers on top of the solar cell lead to a reduction of the pitch of the resulting meshed GND if the fingers are not perfectly aligned with the ground grid lines of the antenna during the assembly procedure. The axial ratio curves show a shift of the minimum value, too (see Fig. 4.11c). The antenna has a lowest measured axial ratio value of 1.2 dB at 24.36 GHz. If a solar cell is present on the back side, a measured minimum value of 2.8 dB is obtained at 24.9 GHz. In terms of the antenna gain the radiation pattern are evaluated at the frequency with the lowest axial ratio value. The corresponding input reflection coefficients  $|S_{11}|$  are lower than -10 dB. Fig. 4.11b shows the radiation pattern for both evaluated cutting planes at  $\varphi = 0^\circ$  and  $\varphi = 90^\circ$ . At  $\vartheta = 0^\circ$  the simulated and measured

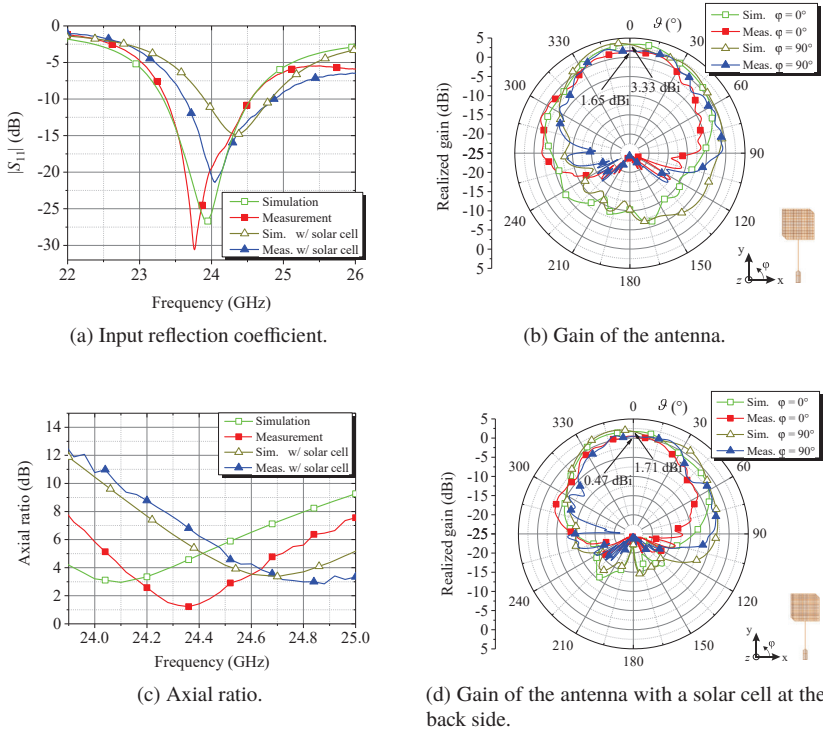


Figure 4.11 Comparison between simulation and measurement results of a meshed RHCP patch antenna.

realized gain is  $G_{sim} = 3.33$  dBi and  $G_{meas} = 1.65$  dBi, respectively. On the one hand, this difference is probably due to measurement uncertainties of the antenna measurement technique used. Based on empirical values, this has a deviation of approx. 1 dB. On the other hand, the electrical connection between the microstrip lines on different RF substrate cannot be remodeled exactly as in reality. However, a good agreement of the radiation pattern can be achieved for the forward half space ( $-90^\circ \leq \vartheta \leq +90^\circ$ ). The high deviation for an angular range  $90^\circ < \vartheta < 270^\circ$  is due to the measurement technique used in the anechoic chamber. This allows an exact determination of the radiation pattern only in the forward half space. The influence of the solar cell on the realized gain



values is shown in Fig. 4.11d. At the main direction ( $\vartheta = 0^\circ$ ) the measured gain value decreases by 1.2 dB to 0.47 dB. Modeling the photovoltaic layer with a conductivity of  $\sigma_{sc} = 10 \text{ kS/m}$  results in an adequate agreement between simulation and measurement. The associated radiation efficiency is 50 % and 33 % for the simulation model without and with the solar cell at the back of the antenna, respectively. If the photovoltaic layer has a conductivity value such as 2 kS/m (for example in low ambient light), it would lead to a radiation efficiency of 31 % and a gain reduction of roughly 0.2 dB.

The presented findings and results on patch antennas are the basis for designing an optimal antenna for the sensor tag. In the following, the final antenna layout is discussed.

#### 4.1.4 Final Antenna Layout

The meshed patch antenna presented in Sec. 4.1.3 is designed for the investigation of the influence of the solar cell on antenna characteristics. In order to increase the radiation efficiency and the antenna gain, the pitch of the grid structure should be decreased but at the same time, the transparency should be as high as possible. The goal is to develop an antenna with a gain value of at least 4 dBi to fulfill the specification of the application. Thus, a compromise has to be found between antenna properties and optical transparency.

At first, a non-transparent circularly polarized patch antenna is designed on quartz glass ( $\epsilon_r' = 3.81$  and  $\tan \delta = 0.0004$  at 24 GHz) with a thickness of 0.22 mm. This antenna is fed by a microstrip line and the maximum achievable antenna gain value is  $G_{p,\text{solid}} = 6.4 \text{ dBi}$  at a radiation efficiency of 85 %. These values are for reference. In the next step, this structure is modified to an optically transparent antenna. The final layout of the developed circularly polarized patch antenna as well as the geometrical parameters are depicted in Fig. 4.12. The top layer is shown on the upper part while the bottom layer (GND) is on the lower part. Since the pitch and the width of the fingers of the solar cell is about  $g_{2,\text{GND}} = 0.14 \text{ mm}$  and  $w_{1,\text{GND}} = 10 \text{ }\mu\text{m}$ , respectively, the meshed ground plane area around the radiating element is designed with the same geometry in  $x$ - and  $y$ -direction. If the grid lines in  $x$ -direction is perfectly aligned with the fingers these grid lines would not shade the solar cell underneath. The highest field strength is expected around the area underneath the patch. For this reason, the pitch  $g_{1,\text{GND}}$  is assigned to be  $g_{1,\text{GND}} = 0.06 \text{ mm}$  ( $\sim 0.005 \lambda_0$ ). The grid line width of the ground plane is  $w_{1,\text{GND}} = 0.01 \text{ mm}$ . The patch itself has an alternating grid line width of  $w_{p,1} = 0.01 \text{ mm}$  and  $w_{p,2} = 0.02 \text{ mm}$ . This

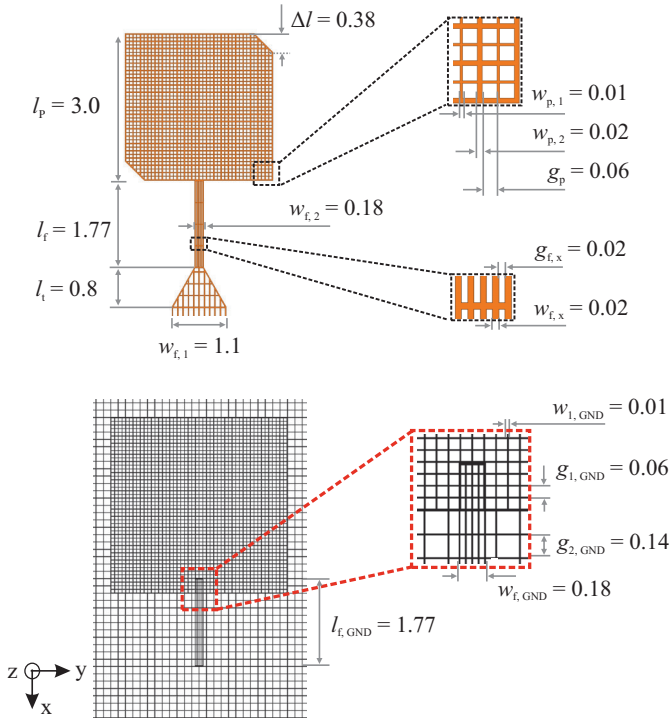
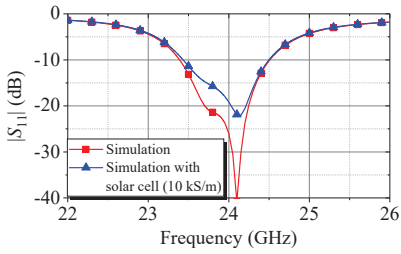


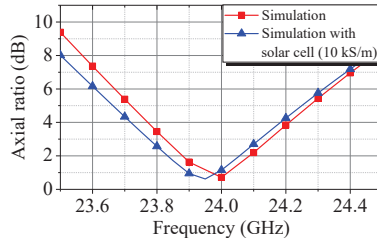
Figure 4.12 Layout and detailed view of the meshed patch antenna. Upper half: top layer. Lower half: a part of the bottom layer (cf. Fig. 4.1). All dimensions in millimeter. [QHD1]

structure was designed with different line widths because it was found out that grid line width in the range of 0.01 mm cause higher conductor losses (see Sec. 3.3.2) which result in lower antenna efficiency. The averaged *MeshFactor* of the patch is  $MF_{x,y} \approx 0.2$ . The meshed microstrip feed line consists of two different sections with the length  $l_t$  and  $l_f$  in order to provide an impedance matching between the patch antenna and the  $30\Omega$  feed line section with the width  $w_{f,1}$ . The reason for using this impedance value will be discussed in Sec. 4.2.3. Furthermore, the feed line is optimized in terms of low insertion losses. Thus, the section  $l_f$  has a *MeshFactor<sub>y</sub>* of  $MF_y = 0.5$ .

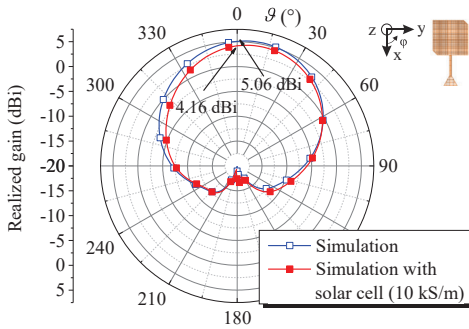
The input reflection coefficient and the axial ratio of the antenna are depicted



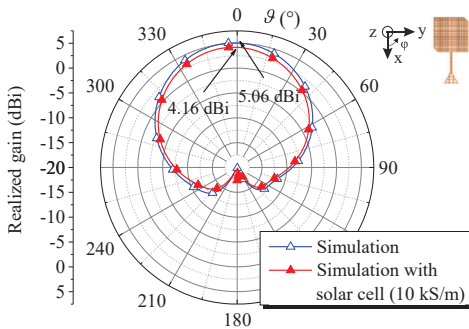
(a) Input reflection coefficient. [QHD1]



(b) Axial ratio. [QHD1]



(c) Radiation pattern for the cut plane  $\varphi = 0^\circ$ . Operating frequency  $f = 24.05$  GHz.



(d) Radiation pattern for the cut plane  $\varphi = 90^\circ$ . Operating frequency  $f = 24.05$  GHz.

Figure 4.13 Simulation results of the circularly polarized patch antenna (final layout).

in Fig. 4.13a and 4.13b. The curves marked with squares and triangles represent the results numerically calculated without and with a solar cell on the bottom side of the antenna, respectively. The comparison between these two cases shows that the solar cell has a minor influence on these antenna characteristics. This is because the ground plane is designed with a sufficiently dense mesh in this case (c.f. 4.1.3). At a frequency of  $f = 24$  GHz the simulated results show an input reflection coefficient of  $|S_{11}| = -19$  dB and an axial ratio of  $AR = 1.1$  dB. The radiation pattern for both cutting planes at  $\varphi = 0^\circ$  and  $\varphi = 90^\circ$  are shown in Fig. 4.13c and 4.13d. In this case the operating frequency is  $f = 24.05$  GHz. For a setup without and with a solar cell the antenna peak gain value achieved is  $G_p = 5.2$  dBi (59 % radiation efficiency) and  $G_{p,sc} = 4.4$  dBi (49 % radiation efficiency), respectively. These values are obtained at the cutting plane  $\varphi = 0^\circ$  and an angle of  $\vartheta = 15^\circ$ . The reason for this squint angle is the feed line that influences the radiation characteristic. In case of the solar cell placed on the back of the antenna, the half power beam width for the cutting plane  $\varphi = 0^\circ$  and  $\varphi = 90^\circ$  are  $76^\circ$  and  $86^\circ$ , respectively. Furthermore, it can be noted that the antenna does not radiate as much to the rear as in the configuration presented in Sec. 4.1.3. In summary, it can be stated that the presented antenna performances meet the specifications of the project. Therefore, this meshed patch antenna is suitable for the integration with an analog front-end.

The following Table 4.1 summarizes the main characteristics of the developed meshed patch antenna arranged on the used solar cell.

Characteristic	Value
Input reflection coefficient	< -20 dB
Peak realized gain	4.4 dBi
Half power beam width (E-plane & H-plane)	$78^\circ$
Axial ratio	< 2 dB
Radiation efficiency	49 %

Table 4.1 Simulated main characteristics (at 24.05 GHz) of the optically transparent RHCP patch antenna arranged on the used solar cell.

### 4.1.5 Conclusion

The most important results of the investigation on the meshed patch antenna are:

- Compared to a conventional patch antenna, meshing the patch antenna results in a decrease of the resonance frequency, the gain, the radiation efficiency, the front-to-back ratio and the antenna impedance.
- In general, the grid lines should be aligned with the direction of the electrical current of the desired resonance mode, which is important for patch antennas. In the case of a circularly polarized patch antenna, the grid lines should be evenly distributed in horizontal and vertical direction.
- Depending on the application requirements, a compromise between antenna characteristics and optical transparency needs to be found.

## 4.2 Discrete Circuit Design

For an exchange of data between a reader and a sensor tag a well-developed analog front-end is needed, especially for the tag. Here, the analog front-end consists of a modulator and a demodulator unit. Commercial modulators and demodulators as well as Monolithic Microwave Integrated Circuits (MMICs) are not suitable, considering the given integration scenario and the limited availability of the DC power. Thus, the analog front-end must be designed according to the specific application requirements.

At first, the concept of the modulator unit is discussed. It bases on the principle of the backscatter modulation. Afterwards, subsection 4.2.2 deals with the design of the demodulator circuit. The characteristics of each unit obtained by a simulation software are shown. The key parameters to be evaluated are input reflection coefficients and output voltage of the demodulated signal. A verification of the simulated results of an optically transparent analog front-end is carried out. The achieved characteristics of this circuit are presented and compared with its opaque counterpart. A brief conclusion is provided at the end of this section.

### 4.2.1 Modulator Unit

As stated in Sec. 2.1, a semi-passive tag does not have its own RF transmitting unit. Therefore, the tag must modulate and backscatter the signal emitted by

the reader unit. In order to achieve that, the tag varies its radar cross section (RCS). The following section explains how the tag can change its RCS value in order to generate a backscattered amplitude modulated signal.

#### 4.2.1.1 Principle of the Backscatter Modulation

A simple schematic description of the principle of the backscatter modulation is shown in Figure 4.14. In this case, the reader unit transmits a continuous wave. This signal arrives at the tag and can now either be absorbed or reflected. This means that the reflected power is modulated in its amplitude. This process can be realized e.g. by a switch. By applying a control signal to the switch, it is possible to obtain two impedance states:

$$Z_1 = R_1 + jX_1 \quad (4.1)$$

and

$$Z_2 = R_2 + jX_2. \quad (4.2)$$

The impedance of the antenna is

$$Z_a = R_a + jX_a. \quad (4.3)$$

The reflection coefficient can be calculated as follows:

$$\Gamma_{1,2} = \frac{Z_{1,2} - Z_a^*}{Z_{1,2} + Z_a}. \quad (4.4)$$

Fig. 4.15 depicts two possible states  $\Gamma_{1,2}$  of the tag. The reflection coefficient  $\Gamma$  is a complex number and can therefore be any value within the shown smith

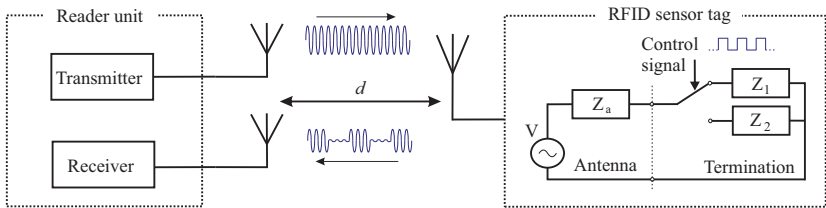


Figure 4.14 Block diagram of the principle of backscatter modulation.

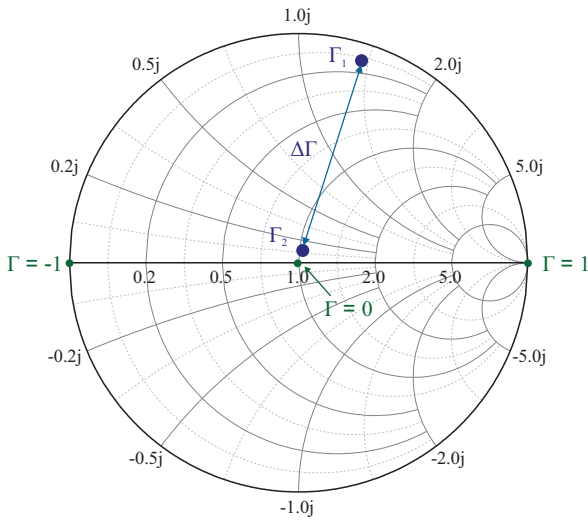


Figure 4.15 Smith diagram with two possible reflection states of the tag for real antenna impedance.

diagram. In case of  $Z_2 = Z_a^*$  the reflection coefficient  $\Gamma_2$  is zero. Thus, the entire power of the electromagnetic wave is ideally absorbed. In practical implementation,  $\Gamma_2$  can only be approx. zero. Therefore, the reader detects a small voltage amplitude, and in terms of data bits this can be interpreted as a "0". At the second state  $Z_1 \neq Z_a^*$ . Ideally, the incoming wave is completely reflected and  $|\Gamma_1|$  can be -1 or 1. Consequently, the reader will detect a "1". However, the amount of power that will be received by the reader depends on many factors. To understand the possibilities and limitations of a modulated, backscattered channel, some basic formulas are discussed in the following. The power transmission can be described with the link budget equation. The available power  $P_{Tag}$  at the tag can be calculated as follows:

$$P_{Tag} = A_e \frac{G_{Tx} P_{Tx}}{4\pi d^2}. \tag{4.5}$$

Here,  $d$  is the distance between tag and reader (see Fig. 4.14).  $P_{Tx}$  is the transmit power and  $G_{Tx}$  is the gain of the transmit antenna of the reader. The effective

aperture  $A_e$  can be expressed by the following equation:

$$A_e = \frac{G_{Tag} \lambda^2}{4\pi} \Delta\Gamma. \quad (4.6)$$

Here,  $G_{Tag}$  is the antenna gain of the tag. The parameter  $\Delta\Gamma$  is the differential reflection coefficient of the tag and is defined as [74]:

$$\Delta\Gamma = p_1 \left(1 - |\Gamma_1|^2\right) + p_2 \left(1 - |\Gamma_2|^2\right). \quad (4.7)$$

Both parameters  $p_1$  and  $p_2$  indicate the dwell time in the respective state. For the assumption that both states exist and occur equally frequently,  $p_1 = p_2 = 0.5$ . Thus, Eq. (4.6) can be expressed as follows:

$$A_e = \frac{G_{Tag} \lambda^2}{4\pi} \left(1 - \frac{1}{2} [|\Gamma_1|^2 + |\Gamma_2|^2]\right). \quad (4.8)$$

The radar cross section is defined according to [75]:

$$\sigma = \sigma_0 + \sigma_m = \frac{G_{Tag}^2 \lambda^2}{4\pi} \left|1 - \frac{1}{2} (\Gamma_1 + \Gamma_2)\right|^2 + \frac{G_{Tag}^2 \lambda^2}{4\pi} \left|\frac{1}{2} (\Gamma_1 - \Gamma_2)\right|^2. \quad (4.9)$$

Here, the parameter  $\sigma_0$  is the static backscatter at the carrier frequency and the expression  $\sigma_m$  describes the modulated backscatter containing the transmitted information. The available received power  $P_{rx}$  at the reader unit can be calculated according to the following expression [74]:

$$P_{rx} = \sigma \frac{\lambda^2 P_{tx} G_{tx} G_{rx}}{(4\pi)^3 d^4}. \quad (4.10)$$

From the radar equation Eq. (4.10) it can be seen that the received power  $P_{rx}$  depends on the available transmission power  $P_{tx}$ , the distance  $d$  between the reader and the tag, the operating frequency  $f$  or the wavelength  $\lambda$  of the system, the effective aperture  $A_e$ , the radar cross section  $\sigma$ , as well as the gain  $G_{tx}$  and  $G_{rx}$  of the antennas at the reader. This shows that the higher the parameter  $\sigma$  or the difference between the two reflection states, the higher the power level at the reader at a fixed distance or the transmission range of the system.



### 4.2.1.2 Design Concept and Characteristics of the Modulator Circuit

In order to generate two different reflection states  $\Gamma_1$  and  $\Gamma_2$  a modulator unit is needed. Such a configuration for an RFID tag is shown in Fig. 4.16. The used modulator is arranged in a shunt configuration to the demodulator and both are connected to a microcontroller (MCU). Here, the modulator consists of a transistor that can be considered as a switch. By applying a voltage  $V_{GS}$  at the gate terminal, the impedance of the transistor and thus, the impedance of the whole circuit can be changed. In [16] such a circuit topology using an Enhancement Mode Pseudomorphic High Electron Mobility Transistor (E-pHEMT) has been investigated in detail. The study shows that an E-pHEMT is best suited for an RFID tag since it has a high switching speed and a low power consumption. An additional advantage is the low supply voltage lower than 1 V. The used transistor in [16] and in this work is a commercially available transistor named VMMK-1225 from Avago Technologies [76]. This component can be used for applications between 0.5 GHz and 26 GHz. The manufacturer provides a simulation model that can be used for the design process.

In [16] the relationship between the characteristics of the transistor as a function of the applied voltages has already been investigated. It was found out that for a voltage  $V_{GS} \geq 0.7$  V the input reflection coefficient  $\Gamma_2$  did not change significantly. Thus, the applied voltage  $V_{GS}$  should be limited, since a higher voltage level causes a higher gate source current  $I_{GS}$  that results in an increased power loss. The current consumption of the used E-pHEMT at different gate source voltage is shown in Tab. 4.2. The measured results are obtained using a B2912A Precision Source/Measure Unit from Keysight Technologies, Inc.. Hereby, the 4-wire measurement capability is utilized.

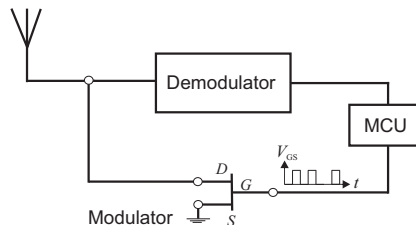


Figure 4.16 Schematic configuration of a transistor as a modulator unit in parallel configuration to the demodulator unit.

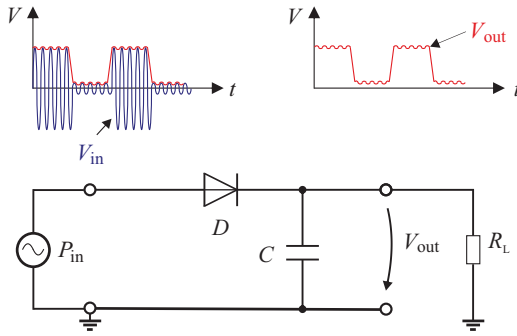
Gate Source Voltage	Gate Source Current	Power Consumption
$V_{GS}$ (V)	$I_{GS}$ ( $\mu$ A)	$P_{GS}$ ( $\mu$ W)
0.6	0.8	0.48
0.7	9.1	6.37
0.8	77	61.6
0.9	478	430.2
1.0	2144	2144

Table 4.2 Measured current consumption of the E-pHEMT VMMK-1225 at different gate source voltage using a 4-wire measurement method. Drain not connected ( $V_{DS} = 0$  V).

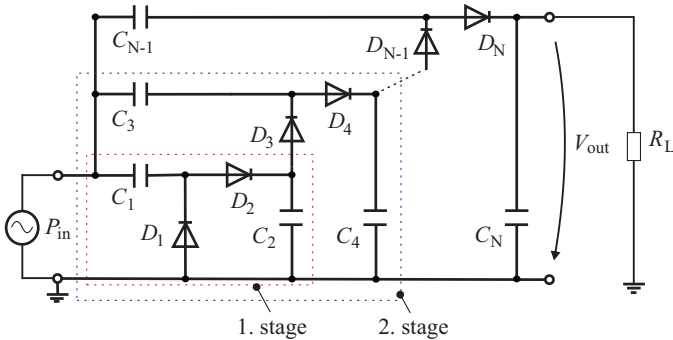
At a gate source voltage of  $V_{GS} = 0.7$  V the gate source current is  $I_{GS} = 9.1$   $\mu$ A. Assuming that the two reflection states  $\Gamma_1$  ( $V_{GS} = 0.7$  V) and  $\Gamma_2$  ( $V_{GS} = 0$  V) have the same probability of occurrence, the average power consumption of the transistor can be specified as  $P_{GS} = 3.19$   $\mu$ W.

## 4.2.2 Demodulator Unit

In the case of communication from the reader to the tag, the received signal must be demodulated. The demodulator unit is a circuit part that demodulates the high frequency signal of the reader unit. The resulting base band signal is routed to a microcontroller (MCU). The arrangement of this unit with respect to other circuit components is shown in Fig. 4.16. Typically, in RFID tags an envelope demodulator circuit is used, since amplitude shift keying (ASK) is utilized [3]. This technique is also applied in this work. A simple envelope demodulator (half-wave demodulator) consisting of a Schottky diode ( $D$ ) and a capacitor  $C$  is shown in Fig. 4.17a. Here,  $R_L$  is the load resistance. This circuit demodulates an amplitude modulated high frequency signal  $V_{in}$  with a carrier frequency of 24 GHz. The desired base band signal  $V_{out}$  corresponds to the data signal transmitted by the reader. In order to increase  $V_{out}$  and thus the communication distance of the whole system, a voltage multiplier circuit could be used. As shown in Fig. 4.17b the first stage (full-wave envelope demodulator) consists of two diodes and two capacitors representing a voltage doubler. Ideally, this topology generates a double output voltage in comparison to a half-wave envelope demodulator. Furthermore, additional stages (N-stages) can be used



(a) Half-wave envelope demodulator.



(b) Example of a voltage multiplier circuit. Full-wave envelope demodulator with N stages.

Figure 4.17 Simplified equivalent circuit diagrams of a demodulator circuit. [QHD1]

for an enhancement of the voltage level [77, 78]. In this work, the advantage of cascading with regard to the achievable output voltage has to be considered by means of numerical simulation. However, some disadvantages compared to the half-wave envelope demodulator can already be listed:

- Increased number of discrete components
- Increased use of layout space for circuit design
- Increased complexity in the design process

Another important aspect for the design of the demodulator circuit is the appropriate selection of components. The efficiency of such a circuit depends strongly on the sensitivity of the used diode. The overall sensitivity  $\gamma_D$  of a diode is defined by the ratio of the output voltage to the input power:

$$\gamma_D = \frac{V_{out}}{P_{in}}. \quad (4.11)$$

A small signal model of a Schottky diode is shown in Fig. 4.18 by the dashed box. The resistor  $R_S$  represents the losses in the terminals of the diode.  $R_V$  is the video resistance, where the RF power is converted in voltage. All RF signals should pass through this resistance to achieve the highest possible output voltage. The parameter  $C_j$  is the parasitic junction capacitance. Within the square law detection region (region where  $V_{out}$  is proportional to  $P_{in}$  at low input power levels lower than -20 dBm) and assuming an ideal impedance matching between the antenna and the detector the voltage sensitivity  $\gamma_s$  can be given by [3]:

$$\gamma_s = \frac{0.52}{I_S(1 + \omega^2 C_j^2 R_S R_V)(1 + \frac{R_V}{R_L})}. \quad (4.12)$$

Here,  $I_S$  is the saturation current of the diode and  $R_L$  is the load resistance. In this work, the demodulator is connected to an integrated comparator unit of the microcontroller. Ideally, the load resistance is infinite. Thus, the Eq. 4.12 can be rewritten to:

$$\gamma_s = \frac{0.52}{I_S(1 + \omega^2 C_j^2 R_S R_V)}. \quad (4.13)$$

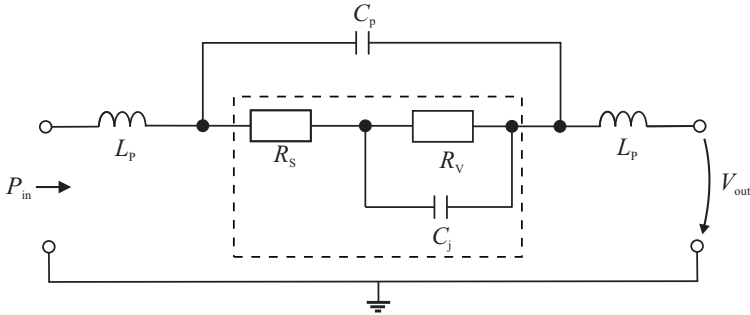


Figure 4.18 Small signal model of a Schottky diode.

From the equation 4.13 it can be noted that the higher the operation frequency the lower the sensitivity value. At a fixed frequency, the junction capacitance has higher impact on the voltage sensitivity compared to other parameters. Therefore,  $C_j$  is the most important characteristic of the diode that has to be as low as possible in order to maximize  $\gamma_s$ .

In addition to the discussed parameters, the package of the diode has also an impact on the sensitivity value that is not included in equation 4.12. Hence, the small signal model has to be extended by the parasitic capacitance  $C_p$  and the parasitic inductance  $L_p$  of the package. In this case, Eq. 4.11 can be used for further evaluation.

In order to select a diode that is suitable for the RFID application, its characteristic parameters should be compared carefully. Table 4.3 shows some diodes from the company Broadcom Limited (formerly Avago Technologies) and Virginia Diodes Inc., which have promising electrical properties. It can be noted that the HSCH-9161 has better characteristic compared to the HSMS-285x due to lower parasitic inductance and capacitance. Although not all parameters are given in the data sheet for the SKD-VDI-FLCH-002 diode, it can initially be seen that the capacitance  $C_j$  is lower than for the HSCH-9161. The latter two diodes are now examined in terms of the sensitivity  $\gamma_D$  by numerical simulation using Keysight Advanced Design Systems (ADS 2009). For this purpose, simulation models provided by the manufacturer were utilized.

Fig. 4.19a depicts the simulated DC output voltage as a function of the

	HSMS-285x [79]	HSCH-9161 [80]		SKD-VDI-FLCH-002 [81]
		D1	D2	
Package	SOT-23	Beamlead		Chip
$L_p$ (nH)	2	0.3	0.3	-
$C_p$ (pF)	0.08	0.011	0.011	-
$C_j$ (pF)	0.18	0.03	0.03	0.025
$R_s$ ( $\Omega$ )	25	50	10	-
$R_{v,\min}$ (k $\Omega$ )	9	2.45	2.49	2.5
$R_{v,\max}$ (k $\Omega$ )	-	7.45	7.49	6.5

Table 4.3 SPICE parameter of several Schottky diodes from Broadcom Limited and Virginia Diodes Inc..

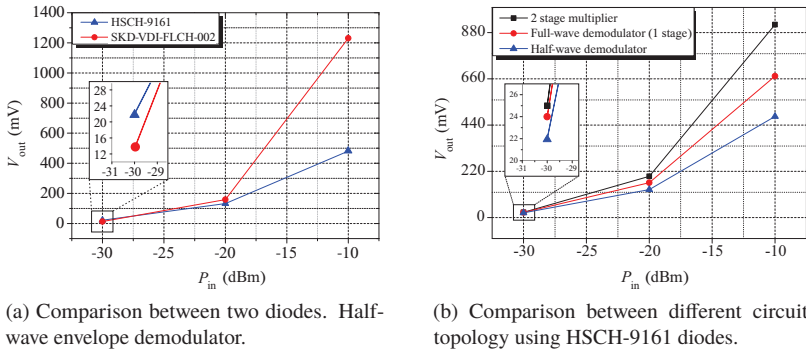


Figure 4.19 Simulation results of the overall sensitivity. Output voltage as a function of the input power at 24 GHz. [QHD1]

input power (24 GHz continuous wave signal) of two half-wave envelope demodulators (cf. Fig. 4.17a), each with a different zero bias Schottky diode (Keysight HSCH-9161 and Virginia Diodes Inc. SKD-VDI-FLCH-002). In the following preliminary investigations, an impedance matching is carried out for each circuit. The output capacitance is  $C = 0.3$  pF and the load resistance is  $R_L = 1$  M $\Omega$ . The higher the output voltage, the larger the communication distance between the reader and the tag. It can be noted that at an input power of higher than  $-20$  dBm the SKD-VDI-FLCH-002 has a higher voltage sensitivity. However, at an input power of  $P_{in} = -30$  dBm the circuit with the HSCH-9161 provides a higher output voltage. Thus, the HSCH-9161 diode is selected for further investigations of using voltage multiplier circuits as shown in Fig. 4.19b. It should be evaluated by which factor the output voltage can be increased.

The simulation results of three different circuit topologies are depicted in Fig. 4.19b. At  $-10$  dBm input power the output voltage  $V_{out}$  of the two stage voltage multiplier circuit is 91 % higher than the output voltage of the half-wave envelope demodulator circuit but at  $P_{in} = -30$  dBm an increase of just 13 % can be obtained. At lower  $P_{in}$  the power losses in each diode play a more dominant role. Furthermore, the expected higher output voltage will be reduced further once the losses of the transmission lines on a printed circuit board (PCB) are taken into account. Considering the advantage (high output voltage) and disadvantages (listed in the beginning of this section) of voltage multiplier circuits, the topology of a half-wave envelope demodulator circuit is used in this work.

### 4.2.3 Modulator and Demodulator Unit - Reference Circuit

Based on the previous work from the 2nd funding period [16] a reference circuit of a modulator and demodulator unit is designed using microstrip line technology. Hereby, the layout of the circuit should be arranged in such way that both the presented antenna (see Fig. 4.12) as well as the analog front-end fits within an area of the solar cell of 10 mm × 10 mm. Since the vertical dimension of the patch antenna is already 6 mm, the layout of the analog front-end should be oriented horizontally below the antenna.

A simplified schematic of the modulator and demodulator circuit to be designed is depicted in Fig. 4.20. The four rectangular elements represent each section of a microstrip line with an impedance  $Z_x$  and a length  $l_x$ . An

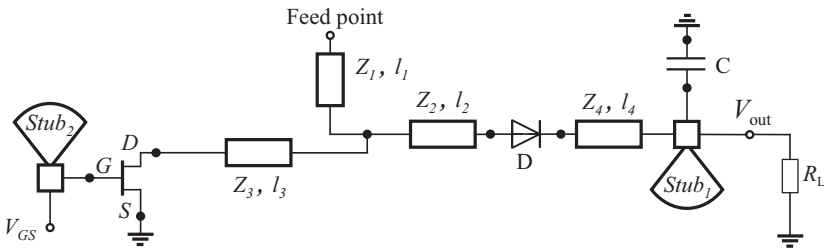


Figure 4.20 Simplified schematic of the investigated modulator and demodulator circuit. [QHD4]

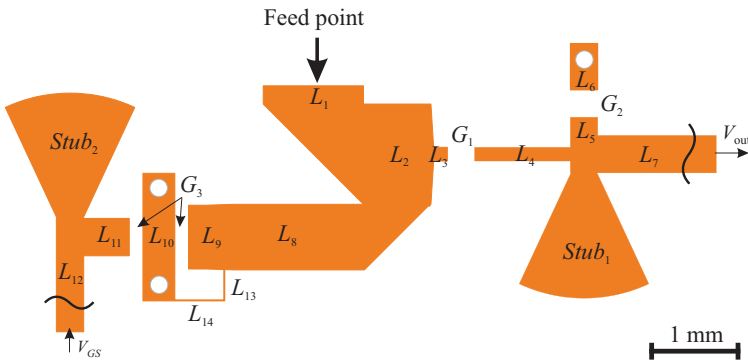


Figure 4.21 Layout of the reference circuit. An optically non-transparent modulator and demodulator circuit.

optimized layout of an optically non-transparent modulator and demodulator circuit is shown in Fig. 4.21. The geometric dimensions of each microstrip line section are listed in Table 4.4. The width of the gaps needed for an assembly of electrical components are summarized in Table 4.5.

The layout is designed for the same glass substrate as the antenna. The used dielectric constant is  $\epsilon'_r = 3.81$  and the dissipation factor is  $\tan\delta = 0.0004$ . These values are obtained by a resonator measurement method at a frequency of  $f = 24$  GHz. Since the real part of the input impedance of the half-wave

Microstrip line	Width $w$ (mm)	Length $l$ (mm)
$L_1$	1.1	0.2
$L_2$	1.1	0.74
$L_3$	1.1 $\rightarrow$ 0.15	0.18
$L_4$	0.15	1.05
$L_5$	0.3	0.61
$L_6$	0.3	0.51
$L_7$	0.41	1
$L_8$	0.72	1.43
$L_9$	0.72 $\rightarrow$ 0.7	0.5
$L_{10}$	0.35	1.4
$L_{11}$	0.41	0.5
$L_{12}$	0.3	1
$L_{13}$	0.01	0.34
$L_{14}$	0.01	0.55

Table 4.4 Geometric dimensions of the microstrip lines according to Fig. 4.21.

Gap	Width (mm)
$G_1$	0.3
$G_2$	0.3
$G_3$	0.15

Table 4.5 Geometric dimensions of the gaps according to Fig. 4.21.



envelope demodulator is approx.  $18 \Omega$  (ideal consideration without feeding lines at  $f = 24 \text{ GHz}$ ,  $P_{in} = -30 \text{ dBm}$  and  $R_L = 1 \text{ M}\Omega$ ) the impedance of the microstrip line  $L_2$  should have the same value to obtain an ideal impedance matching. A conventional  $18 \Omega$  microstrip line requires a width of  $w = 1.9 \text{ mm}$  and it would lead to a higher space consumption for the whole circuit, especially for the line section  $L_2$ . Furthermore, a wider microstrip line followed by a small mounting pad for the diode (cf. Fig. 4.21) causes higher fringing fields at the corner of the microstrip line. Therefore, a compromise between space usage and input impedance is made and the microstrip feed lines  $L_{1,2}$  are designed to provide a characteristic impedance of  $30 \Omega$  ( $w = 1.1 \text{ mm}$ ). Preliminary investigations have shown that impedance matching of the demodulator circuit to a higher reference impedance of e.g.  $50 \Omega$  leads to a more complex impedance matching network in comparison to the current design, as shown in Fig. 4.21. This in turn results in higher losses. For this reason, the design strategy is based on the concept that the matching network should be kept as simple as possible. The line  $L_4$  between the diode and the capacitor is then designed in such a way that the input impedance of the demodulator unit is matched to the characteristic impedance of the line  $L_2$ . Here, the diode and the capacitor are placed at the area of the gap  $G_1$  and  $G_2$ , respectively. The transistor is located at the gaps  $G_3$ . The three white circles each represent ground vias. The lines  $L_{13}$  and  $L_{14}$  are connected to a ground pad and it is a DC-path for the envelope demodulator. The component  $Stub_1$  and  $Stub_2$  act as an RF short for the high frequency signals and thus both decouple the connected components (DC source and microcontroller. The microstrip line sections between the  $30 \Omega$  feed line  $L_1$  up to the E-pHEMT and the diode are designed in such a manner as to achieve an optimized impedance matching at the circuit input. The used capacitor of  $0.3 \text{ pF}$  is made by the company Johanson Technology and it is previously electrically characterized within the investigated frequency band.

The simulation results obtained by the numerical simulator ADS 2009 are depicted in Fig. 4.22. These investigations are done using the method of moments (MoM) technique. The magnitudes of both reflection states  $\Gamma_{1,2}$  at the feed point are shown in Fig. 4.22a. Here, the reference impedance is  $Z_{ref} = 30 \Omega$ . The mismatched state  $|\Gamma_1| = -2.7 \text{ dB}$  at a frequency of  $f = 24.1 \text{ GHz}$  is obtained by applying a gate-source voltage of  $V_{GS} = 0.7 \text{ V}$ . At the same operating frequency the amplitude of the matched state is  $|\Gamma_2| = -21 \text{ dB}$ . It can be seen from Eq. 4.9 and Eq. 4.10 that the higher the difference between both states, the higher is the resulting communication distance. Fig. 4.22b depicts the simulated output voltage of the demodulator. Here, the desired baseband signal in the shape of

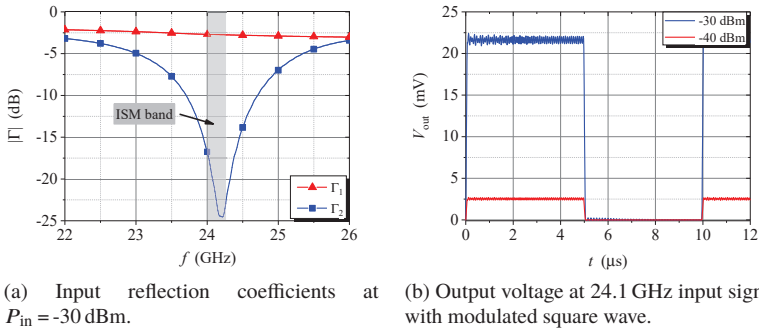


Figure 4.22 Simulation results of the developed reference circuit (reference impedance  $Z_{\text{ref}} = 30 \Omega$ ) according to Fig. 4.21.

a 100 kHz square wave can be obtained. At an input power of  $P_{\text{in}} = -30 \text{ dBm}$  and  $P_{\text{in}} = -40 \text{ dBm}$  the maximum amplitude of the square wave is 22 mV and 2.5 mV, respectively. This demodulated signal is routed to a comparator unit and a microcontroller to process the data.

Since the circuit is designed using a reference impedance of  $Z_{\text{ref}} = 30 \Omega$ , a verification of the simulation results is very time-consuming. However, comparisons between simulated and measured results were carried out in several preliminary studies [QHD9, QHD3], where a reference impedance of  $Z_{\text{ref}} = 50 \Omega$  was used. It can be stated that the simulation parameters as well as the simulation model of the used transistor, diode and capacitor were well modeled. Based on this knowledge, a circuit using any reference impedance value (e.g.  $Z_{\text{ref}} = 30 \Omega$ ) can be investigated by numerical simulations and there is no need to recheck the validity of the simulation results.

#### 4.2.4 Modulator and Demodulator Unit Based on Metal Grid Lines

In order to design an optically transparent modulator and demodulator circuit based on metal grid lines, the presented reference circuit (optically non-transparent circuit) from subsection 4.2.3 can be used as starting point for the development process. Therefore, the design rules derived from the study on the meshed microstrip lines (see Sec. 3.3.2) can be applied. Since the circuit under investigation should have an input impedance of  $Z_{\text{in}} = 30 \Omega$ , a measurement-based verification of the simulation results is more difficult due to the different

input impedance values of both the circuit and the network analyzer. It is already known from earlier works [16], [QHD9, QHD3] with non-transparent circuits that the results from the simulation software Keysight Technologies Advanced Design System (ADS 2009) correspond well to the measurement results. However, a verification for a circuit based on metal grid lines should be done previously.

### 4.2.4.1 Circuit Designed for Verification

In order to confirm the accuracy of the simulation model of a circuit based on grid lines, an optically transparent modulator and demodulator circuit with an input impedance of  $Z_{in} = 50 \Omega$  is designed. The layout is shown in Fig. 4.23. This layout has been developed according to an optically non-transparent design

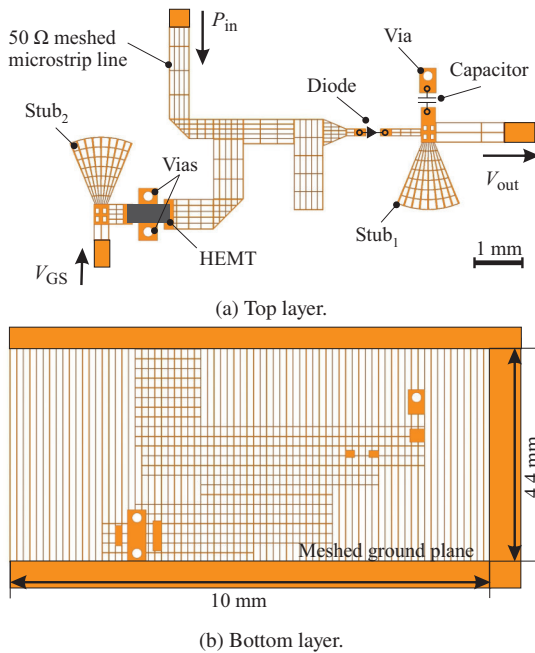


Figure 4.23 Layout of an optically transparent modulator and demodulator circuit with an input impedance of  $Z_{in} = 50 \Omega$ . This circuit is only designed to verify simulation model. [QHD4]

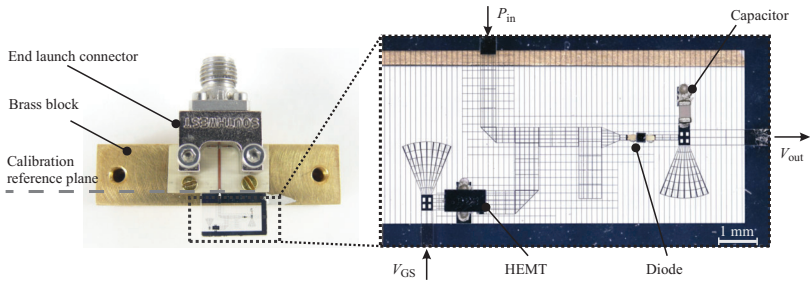
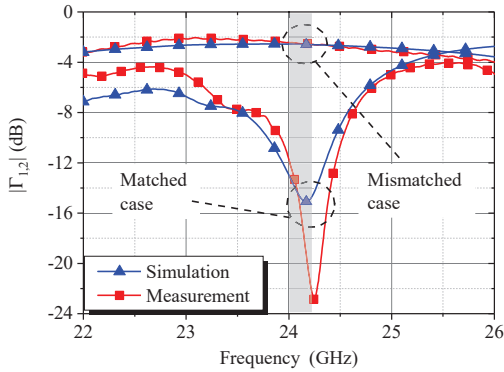


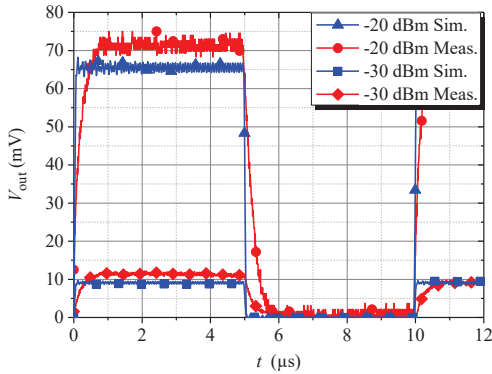
Figure 4.24 Photograph of the realized prototype on quartz glass; left: measurement setup; right: detailed view of the meshed analog front-end with electronic components bonded by two-component adhesives. [QHD4]

from an own study presented in [QHD3]. All grid line widths are about 0.01 mm. Some pads are not meshed due to the attachment of components on them as well as the realization of vias. Furthermore, the three solid pads at the input and the output of the circuit as well as the inverted c-shaped structure on the ground plane are for the assembly and for the measurement purposes. The horizontal and vertical spaces between the grid lines are designed in a manner in order to minimize the insertion losses of the meshed microstrip line. As described in the previous section, the modulator unit consists of an Avago VMMK-1225 high electron mobility transistor (HEMT) in a common source configuration. The demodulator unit is realized by a Keysight HSCH-9161 zero bias beam lead Schottky diode and a 0.3 pF capacitor from Johanson Technology. The overall transparency is about 85 % (based on an area of 10 mm  $\times$  4.4 mm) which is determined by the simulation software Zemax OpticStudio 15.5.

The optically transparent analog front-end fabricated on a quartz glass is shown in Fig. 4.24. The top and bottom side consist of three different metal layers (0.05  $\mu\text{m}$  chromium, 1  $\mu\text{m}$  copper and 0.3  $\mu\text{m}$  platinum) with an overall thickness of approx. 1.3  $\mu\text{m}$ . To obtain the ground connections for the transistor and the capacitor through glass vias are produced by laser ablation. As shown in Fig. 4.24 the fabricated glass substrate is fixed on a block made of brass for measurement purposes. A RO4003C laminate is used to bond the microstrip line of the PCB and the microstrip line of the analog front-end on glass. A TRL calibration process is utilized to de-embed the influence of the end launch connector.



(a) Input reflection coefficients at an input power of  $P_{in} = -20$  dBm.



(b) Output voltage at 24 GHz input signal with modulated square wave (100 kHz).

Figure 4.25 Simulation and measurement results of the fabricated circuit. [QHD4]

Fig. 4.25a depicts the simulated and measured input reflection coefficients of the analog front-end for two different states ( $V_{GS} = 0$  V and  $V_{GS} = 0.7$  V) at an input power of  $P_{in} = -20$  dBm. The curves marked with triangles represent the simulated data and the curves marked with squares are measurement results. There is a slight shift of about 70 MHz (corresponding to 0.29 %) concerning

the resonance frequency for the matched case. All in all, a good agreement can be obtained. At the frequency of  $f = 24$  GHz the measured magnitude of the reflection coefficients are  $\Gamma_1 = -2.4$  dB and  $\Gamma_2 = -12$  dB, respectively.

Fig. 4.25b shows the simulated output voltage of the demodulator unit for a modulated input signal at 24 GHz with square wave baseband signal and two different maximum input power values. The desired 100 kHz square wave signal can be obtained. At an input power level of  $P_{in} = -30$  dBm the simulated and measured amplitude is 9 mV and 11 mV, respectively. The mismatch concerning the slope of the envelope is caused by the measurement setup and mainly by the input capacitance of the oscilloscope. A good agreement between simulation and measurement results is achieved.

#### 4.2.4.2 Final Circuit

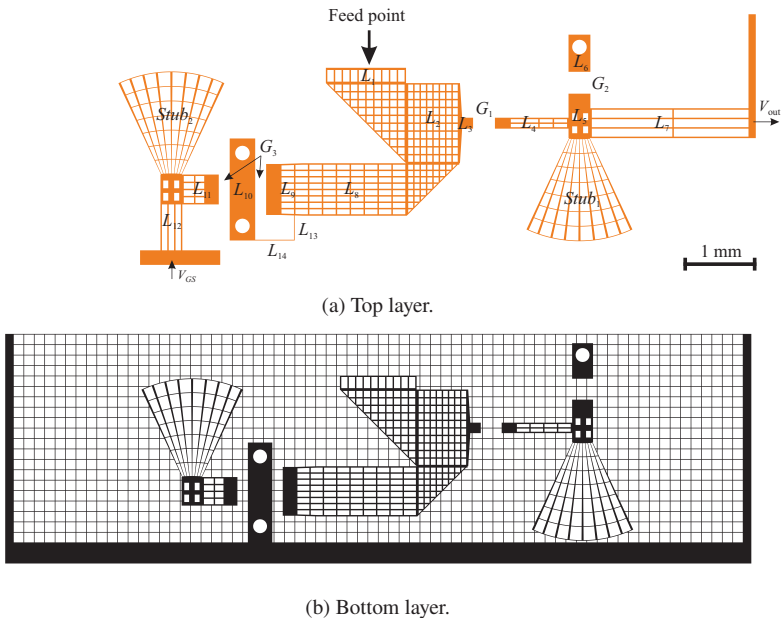


Figure 4.26 Layout of the optically transparent modulator and demodulator circuit based on the investigated circuit as shown in Fig. 4.21.

Once the verification of the simulation model has been successfully completed, the development of the final modulator and demodulator circuit is carried out. The final layout based on the design presented in subsection 4.2.3 (see Fig. 4.21) is shown in Fig. 4.26. It can be noted from the top layer that the pads for the attachment of the discrete components are solid for a reliable solder joint. Furthermore, both solid pads at the end of the line  $L_7$  and  $L_{12}$  are connected with the housing of the tag by conductive adhesive. These pads are placed above the solid u-shaped frame that is shown on the bottom layer. These areas are located outside the solar cell. On the bottom layer, the pads within the areas of the discrete components are also solid, since the pads arranged above are non-transparent. In doing so, a more reliable connection between the grid lines can be ensured. Furthermore, they have no additional negative influence on the electrical characteristics of the solar cell located below. In order to maximize the transparency of the circuit the grid line structure on the top layer is mapped to the bottom layer. Outside from this area, an equally distributed grid structure is used. The pitch of the meshed ground is 0.14 mm while the grid line width is

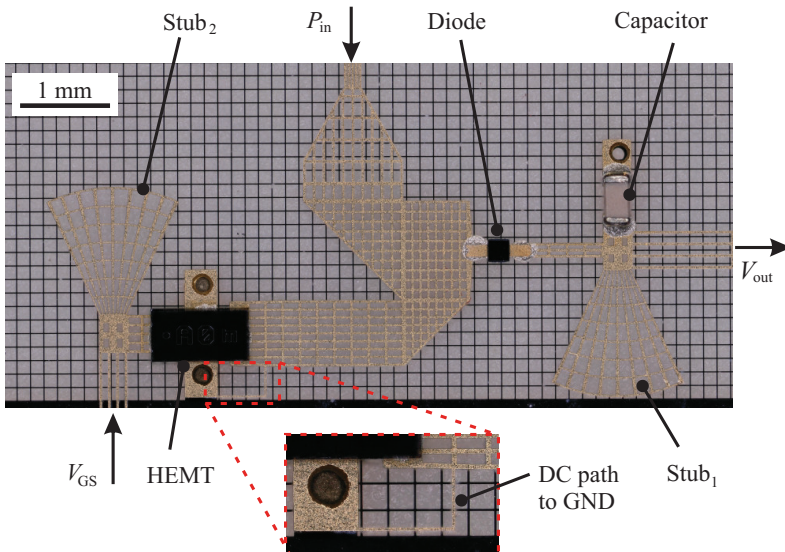


Figure 4.27 Photograph of the fabricated modulator and demodulator circuit on quartz glass (top layer: gold-colored grid lines, bottom layer: grid lines in black). [QHD1]

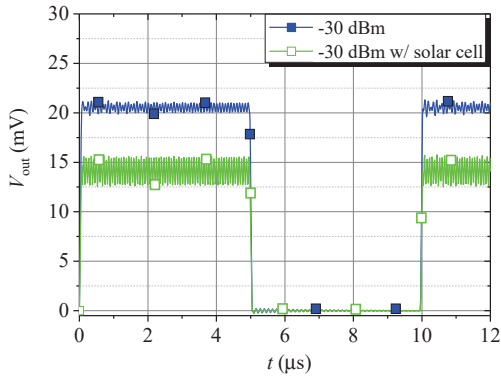
0.01 mm. On the top layer, a grid line width of 0.02 mm is used because of the compromise between optical transparency and RF properties. The geometric dimensions as well as the corresponding percentage of the non-transparent area ( $MeshFactor_A$ ) of each meshed microstrip line sections are summarized in Table 4.6. The area of each stub covered with metal is  $MeshFactor_A = 0.23$ . A comparison with the geometric dimensions of the previously designed reference (non-transparent) circuit (see Table 4.4) shows, that the outer dimensions are unchanged. This confirms that a design step from a non-transparent circuit to a transparent circuit can be done easily and efficiently by applying the given design rules on meshed microstrip lines.

Microstrip line	Width $w$ (mm)	Length $l$ (mm)	$MeshFactor_A$
$L_1$	1.1	0.2	0.39
$L_2$	1.1	0.74	0.40
$L_3$	1.1 $\rightarrow$ 0.15	0.18	1
$L_4$	0.15	1.05	0.55
$L_5$	0.3	0.61	0.86
$L_6$	0.3	0.51	1
$L_7$	0.41	2.17	0.21
$L_8$	0.72	1.43	0.33
$L_9$	0.72 $\rightarrow$ 0.7	0.5	0.59
$L_{10}$	0.35	1.4	1
$L_{11}$	0.41	0.5	0.61
$L_{12}$	0.3	1.04	0.46
$L_{13}$	0.01	0.34	1
$L_{14}$	0.01	0.55	1

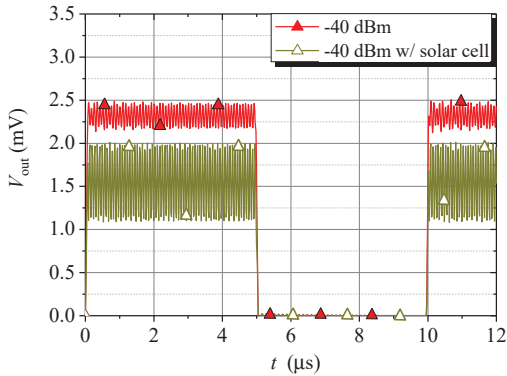
Table 4.6 Geometric dimensions of the meshed microstrip lines according to Fig. 4.26a.

A microscope image of the fabricated modulator and demodulator circuit including the discrete components is depicted in Fig. 4.27. A reflow soldering process is applied to RF components. The gold-colored grid lines are arranged on the top layer while the black-colored grid lines are on the bottom layer. A part of the feed line of the patch antenna is also shown on the upper side of the photograph.





(a) Input power of  $P_{in} = -30$  dBm.



(b) Input power of  $P_{in} = -40$  dBm.

Figure 4.28 Simulation results of the output voltage at 24 GHz input signal with modulated square wave. [QHD1]

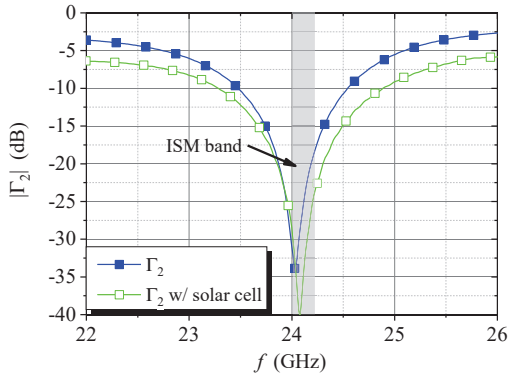
Fig. 4.28 depicts the simulated output voltage of the demodulator unit. In this case, the desired 100 kHz square wave signal can be obtained. At an input power of  $P_{in} = -30$  dBm and  $P_{in} = -40$  dBm the maximum amplitude of the square wave is 21 mV and 2.3 mV. A small amount of the carrier frequency can be observed on this low frequency signal due to the not perfect RF short caused by

	$V_{\text{out}} @ P_{\text{in}} = -36 \text{ dBm}$	$P_{\text{in}} @ V_{\text{out}} = 3.9 \text{ mV}$
Reference circuit	6.5 mV	-38.3 dBm
Meshed circuit	3.9 mV	-36 dBm

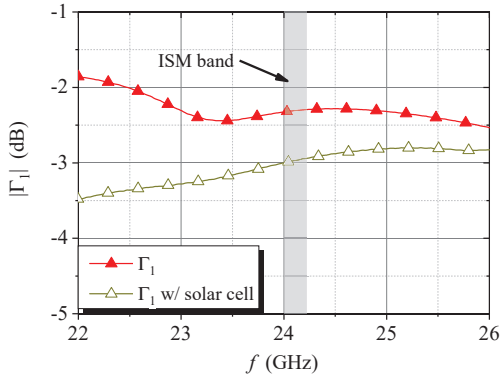
Table 4.7 Comparison of the sensitivity of the reference circuit (optically non-transparent) and the meshed (optically transparent) circuit with the same outer dimensions.

the  $Stub_1$  (see curve marked with filled squares and triangles). A comparison with the reference circuit shows that the output voltage of this circuit is up to 8 % lower (cf. Fig. 4.22b). Modeling this circuit on the used solar cell (assumed conductivity of 10 kS/m) the averaged amplitude decreases by approx. 33 % for a fixed input power value (see curve marked with unfilled squares and triangles). The presence of the fingers of the solar cell (additional grid lines) and the photovoltaic layer leads to a slightly higher amplitude of the 24 GHz signal due to detuning. Now, the sensitivity of the designed reference (optically non-transparent) circuit and the final (optically transparent) meshed circuit is to be compared. In the first column of Table 4.7 the output voltage values at an arbitrarily fixed input power are listed for each circuit. At an input power of  $P_{\text{in}} = -36 \text{ dBm}$  the output voltage of the meshed circuit is  $V_{\text{out}} = 3.9 \text{ mV}$ . In order to obtain the same voltage level the reference circuit only requires an input power of  $P_{\text{in}} = -38.3 \text{ dBm}$ . Thus, the sensitivity of the meshed demodulator unit is 2.3 dB lower than its opaque counterpart.

The magnitudes of both input reflection coefficients are shown in Fig. 4.29 for  $P_{\text{in}} = -30 \text{ dBm}$ . In the mismatched state  $\Gamma$  is  $|\Gamma_1| = -2.3 \text{ dB}$  while at the matched state  $|\Gamma_2| = -31 \text{ dB}$  at 24 GHz can be observed (see curves marked with filled squares and triangles). Taking the solar cell into account, the resonance frequency shift at the matched state is negligible and the 10 dB bandwidth is approx. 50 % larger (see curve marked with unfilled squares). This is caused by the presence of the fingers and the poorly conductive layers ( $\sigma = 10 \text{ kS/m}$ ) of the solar cell. Concerning the mismatched state the input reflection coefficient is  $|\Gamma_1| = -3 \text{ dB}$  as can be seen from the curve marked with unfilled triangles. The difference between both values is crucial for the achievable communication distance  $d$  assuming all other variables in Eq. 4.14 remain constant. The communication distance  $d$  between the reader unit and the RFID sensor tag can be calculated as follows [82]:



(a) Matched state at  $V_{GS} = 0$  V.



(b) Mismatched state at  $V_{GS} = 0.7$  V.

Figure 4.29 Simulation results of the input reflection coefficients at  $P_{in} = -30$  dBm. [QHD1]

$$d^4 = \frac{P_{tx} G_R^2 \lambda_0^4 G_{Tag}^2}{P_{rx} (4\pi)^4} |\Gamma_1 - \Gamma_2|^2. \tag{4.14}$$

Here,  $P_{tx}$  is the transmitted power of the reader,  $P_{rx}$  is the received power at the reader,  $G_R$  is the gain of the reader antenna,  $G_{Tag}$  is the gain of the tag

antenna and  $\lambda_0$  is the free space wavelength. Since the communication distance  $d$  depends on additional parameters that are not yet known, the calculation of the equation 4.14 can only be finally carried out in Sec. 5.3.

The following Table 4.8 summarizes the achieved main characteristics of the developed meshed modulator and demodulator circuit arranged on the used solar cell.

Characteristic	Value
Input reflection coefficient $ \Gamma_1 $ - mismatched state	$\sim -3$ dB
Input reflection coefficient $ \Gamma_2 $ - matched state	$\sim -31$ dB
Power consumption ( $V_{GS} = 0.7$ V)	$6.37 \mu\text{W}$

Table 4.8 Simulated main characteristics (at 24.05 GHz) of the optically transparent modulator and demodulator circuit (final circuit) arranged on the used solar cell.

## 4.2.5 Conclusion

The most important results of the study on the modulator and demodulator circuit are:

- A compact discrete circuit based on meshed microstrip lines is developed. It consists of a Schottky diode HSCH-9161, an E-pHEMT transistor VMMK-1225 and a 0.3 pF capacitor.
- The circuit is designed with a reference impedance of  $Z_{ref} = 30 \Omega$  instead of e.g.  $Z_{ref} = 50 \Omega$  in order to achieve a compact design and a simple impedance matching network of the demodulator unit.
- The sensitivity of the meshed demodulator circuit is 2.3 dB lower than its opaque counterpart.

### 4.3 Fabrication Process

In the previous sections, each component of the analog front-end and the antenna (see layout in Fig. 4.1) was studied and discussed in detail. In this section, the fabrication steps for the realization of the meshed antenna and circuit on a glass substrate are described in the following. Each single manufacturing step and the technologies used are discussed in detail with the individual project partners to ensure a problem-free production process and to obtain a functioning prototype.

A photograph of the fabricated RHCP patch antenna and the modulator and demodulator circuit based on metal grid lines are depicted in the center of Fig. 4.30. The top layer consists of the gold colored grid lines while the black colored grid lines are on the bottom layer. The whole grid structures are realized on a quartz glass. Three discrete RF components (transistor, diode and capacitor) are arranged on the top layer.

The selected quartz glass with a thickness of 0.22 mm is from the company Plan Optik AG [83]. The used dimension of the quartz wafer has a diameter of 4 inch which correspond to 10.16 cm. With this size, 44 samples of the circuit can be realized. The first step is to drill holes for vias. Each circuit has three vias and they are produced by laser ablation with a picosecond laser source ( $\lambda = 515 \text{ nm}$ ). The laser radiation is deflected with a galvanometric scanning system to irradiate the drill hole. The average laser power is set to 3 W at 50 kHz pulse repetition rate. The focal spot size was  $20 \mu\text{m}$ . Markings are also provided

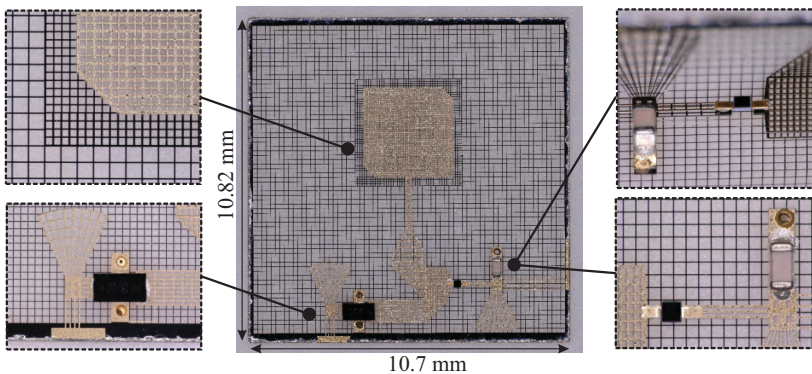


Figure 4.30 Photographs and detailed views of the fabricated meshed analog front-end. Top layer: gold colored grid lines. Bottom layer: black colored grid lines.

on the wafer for the later alignment of the pads to the holes. This production step was carried out by the project partner Laser Zentrum Hannover e.V..

The wafer is then forwarded to the project partner Institute of Micro Production Technology (IMPT) for the realization of the photolithography process. At first, the wafer is RF sputtered on both sides with three different metallization layers. The first layer is chromium with a thickness of  $0.05\ \mu\text{m}$ . It provides a good adhesion to the glass. The second layer is copper with a thickness of  $1\ \mu\text{m}$ . The third metallization layer is gold with a thickness of  $0.3\ \mu\text{m}$ . It serves as a surface finish against oxidation. After this step, a DC connection is established between the front and the back of the wafer through the vias. The photolithography process can then be applied one after the other on both sides. The process includes the application of the photoresist, the alignment of the photomask to the drilling position, the exposure, the removal of photoresist exposed to UV light, the ion beam etching and the removal of remaining photoresist. Subsequently, the desired layout is achieved. An optical and electrical inspection of the vias was carried out and a reliable connection was confirmed. The separation of each single circuit from the wafer is carried out by means of a laser.

In the last step the assembly of the discrete components can be done. Since a larger number of approx. 100 RFID sensor tags are to be manufactured, the assembly was carried out by the company Teprosa GmbH. In this case, a reflow soldering process is preferred. At first, the solder paste is dispensed on the contact pads followed by the placement of the components. These steps are done manually. Afterwards, the assembly is passed a reflow oven. An appropriate reflow soldering thermal profile is used for a reliable connection between electrical components and contact pads. In Fig. 4.30 the mounted components can be seen from different perspectives.

## 4.4 Optical Transparency

In order to give an initial estimate of the optical transparency of the designed circuit, the ratio between the area covered with metal and the total area can be calculated. Since the size of the circuit is larger than the dimensions of the used solar cell, the calculation is based on the area of the solar cell without the busbars (optical aperture:  $10\ \text{mm} \times 9.9\ \text{mm}$ ). Thus, the non-transparent frame of the ground plane that can be seen in Fig. 4.30, is excluded from the calculation. For the top layer including the three components and for the bottom layer the non-transparent area can be specified as 7.6 % and 17 %, respectively. The total opaque area can be determined by overlapping the two layers, which

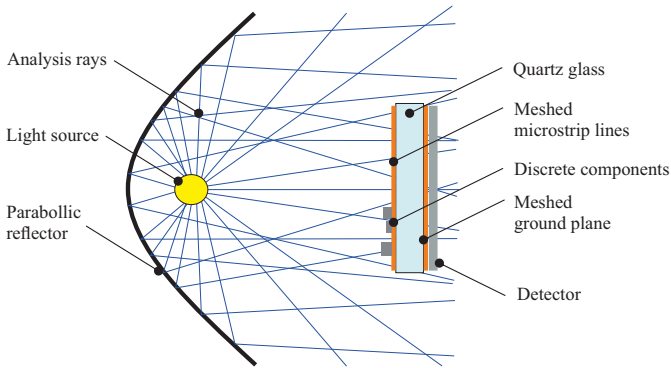


Figure 4.31 Schematic drawing of the simulation model in the ray tracing software Zemax OpticStudio 15.5.

results in a number of 24.58%. Thus, the transparency of the circuit can be given to 75.42%. In this case, the transparency of the quartz glass and physical phenomena such as reflection, diffraction, etc.. are not taken into account.

Another way to determine the transparency of the circuit more precisely is to utilize a software for optical simulation such as Zemax OpticStudio [84]. Based on a non-sequential ray tracing analysis it is possible to trace rays in systems where there are multiple optical paths. The ray hits every object in its path and can reflect, refract, diffract, scatter or split into secondary rays. A schematic drawing of the simulation model is shown in Fig. 4.31. It consists of four main components:

- A light source with an arbitrarily adjustable wavelength. In this case, a wavelength of  $\lambda = 550 \text{ nm}$  is used.
- A parabolic reflector/mirror surface to redirect the rays in different directions. In order to keep the drawing clear only a few analysis rays are shown.
- A detector which detects rays and gives quantitative data of the optical performance e.g. irradiance and radiant intensity.
- The object to be analyzed, which is positioned between the source and the detector.

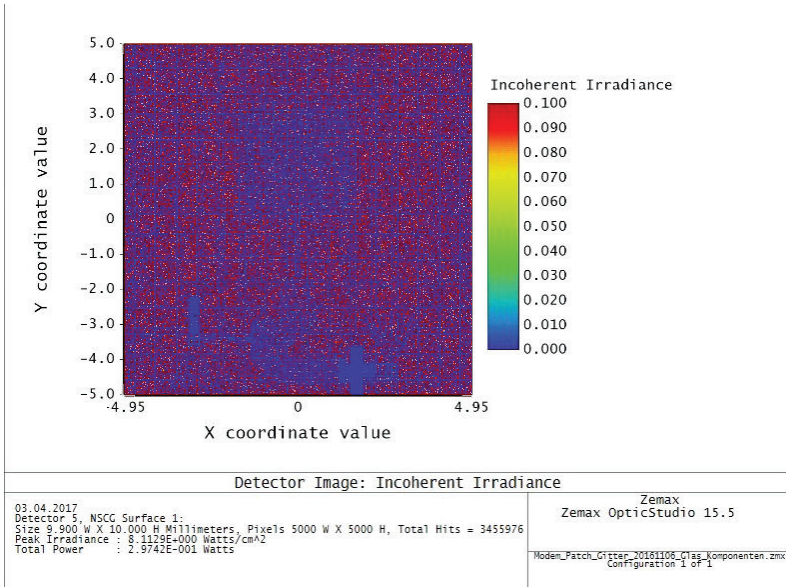


Figure 4.32 Screenshot of the detector viewer that shows the amount of rays traced on the detector.

Here, the object under test is the presented circuit as shown in Fig. 4.30. After importing the three dimensional CAD data into OpticStudio 15.5, a material assignment is done for the quartz glass, the three discrete components and the grid lines. A copper coating is added to the meshed microstrip lines. The simulation is done with 10 million analysis rays. At the detector, the incoherent irradiance can be displayed. It is incoherent power per area as a function of spatial position on the detector [85]. Fig.4.32 depicts a screenshot of the detector viewer. The power of each ray that strikes the detector is summed. In order to obtain the optical transparency of the circuit a second simulation is done without the structure. The difference between the detected power with and without the circuit is the transparency value of the whole structure. Finally, the overall transparency  $T$  can be given as  $T = 74.82\%$ , which is almost equal to the previously calculated value of  $75.42\%$ .



This chapter deals with the entire RFID system, which consists of a sensor tag and a reader unit. Apart from the optically transparent patch antenna and the analog front-end already presented in chapter 4, the tag includes further components that are described in Sec. 5.1. This comprises the digital unit with the microcontroller and the power supply unit. The microcontroller is the central control unit that manages the communication procedure between reader, tag and the complete data processing of the tag. Since the power supply is critical for a miniaturized sensor tag, a discussion on the energy harvesting concept and the power consumption of the sensor tag is given. Next follows a description of the realization of the digital unit and the used assembly process in order to obtain a well-functioning tag. In Sec. 5.2, the characterization of the RF and analog baseband components which are part of the reader unit is presented. The used communication protocol for a proper data exchange between the tag and the reader is also discussed. The last Sec. 5.3 deals with an evaluation of the developed RFID system. Here, the sensitivity of the reader and the tag is addressed. The maximum communication distance between both units are determined by a measurement setup. A short conclusion can be found at the end of each section.

## 5.1 RFID Sensor Tag

In the previous chapter, the design and realization of the antenna as well as the modulator and demodulator circuit are discussed in detail. These components are the RF part of the RFID sensor tag. As shown in Fig. 5.1 the tag consists of additional circuit components such as a microcontroller unit (MCU), a sensor, a power supply unit and an energy storage. These components are referred to as baseband unit. It is needed to evaluate and to process the data transmitted from the reader unit to the tag. Furthermore, it provides information needed by the reader. The functional scope of the tag is mainly defined by the specifications derived from the project. Hence, the tag should provide the following features:

- Unique identification number

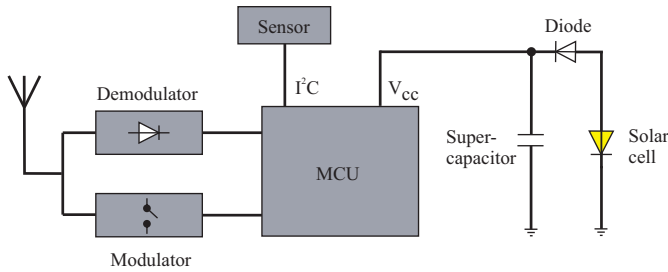


Figure 5.1 Block diagram of the 24 GHz RFID sensor tag.

- Data storage
- Sensor data e.g. temperature value

In the following sections each component of the tag are presented in detail.

### 5.1.1 Baseband Unit

The circuit diagram of the developed baseband unit is shown in Fig. 5.2. The power supply (solar cell and diode) and energy storage (supercapacitor) is depicted on the right hand side. The core unit of the circuit is a microcontroller MSP430FR5738 from the company Texas Instruments [86]. The main reasons for choosing this component are:

- Ultra-low-power consumption with different operating modes. The microcontroller needs a voltage level of at least  $V_{CC} \geq 2 \text{ V}$  for a proper operation.
- 16 kB of nonvolatile memory. A permanent storage of a unique identification number is given. Furthermore, this memory is sufficient for the storage of any other information such as production data and load parameters during the lifetime of a workpiece, which is a specification of the project.
- Integrated temperature sensor and comparator unit. This reduces the number of electrical components and the space required for the circuit.

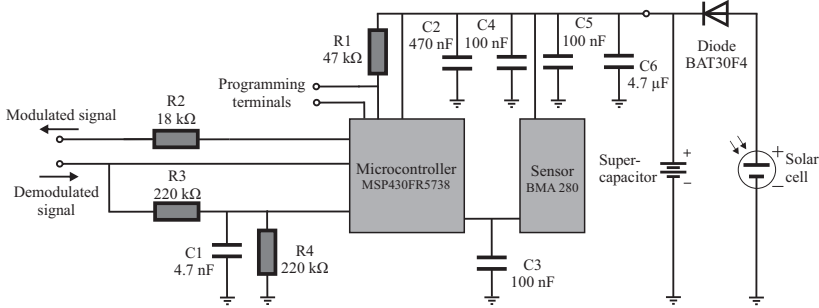


Figure 5.2 Circuit diagram of the baseband unit with power supply and energy storage.

By using this microcontroller, all previously defined functions can already be covered. In order to demonstrate the flexible extensibility of the RFID tag a triaxial acceleration sensor BMA 280 [87] from the company Bosch Sensortec GmbH is added to the baseband unit. In this way, the functionality of the tag can be extended, resulting in an RFID sensor tag. The acceleration sensor has a low current consumption and a small package. The footprint is  $2\text{ mm} \times 2\text{ mm}$ . The communication between the sensor and the microcontroller is implemented by the I<sup>2</sup>C interface. For the programming of the microcontroller a pull-up resistor  $R1 = 47\text{ k}\Omega$  is used. The capacitors  $C2 - C5$  are required for the supply voltage. The power supply concept is based on a solar cell and a supercapacitor acting as an energy storage. The characteristics of both components are presented in Sec. 5.1.2 and Sec. 5.1.3.

In order to communicate with the reader unit the microcontroller controls the gate source voltage level  $V_{GS}$  of the transistor. As stated in Table 4.2 the current consumption of the E-pHEMT depends on the voltage level. Since the logic level of the microcontroller cannot be arbitrarily adjustable and in order to keep the layout as simple as possible, the gate of the transistor is connected via the resistor  $R2$  to an output pin. The resistor limits the gate current of the transistor. In this way, the desired voltage and current characteristics are achieved in good approximation.

The communication from the reader to the tag is accomplished by amplitude shift keying (ASK). In order to process the demodulated analog signal a comparator unit is needed to convert the output voltage of the demodulator to

logic level. Therefore, the average value of the demodulated signal need to be generated e.g. by the resistors  $R3$  and  $R4$  and the capacitor  $C1$  (see Fig. 5.2). In this case, the three components are connected to an integrated comparator of the microcontroller. Since the sensitivity of the RFID sensor tag depends on the threshold level of the comparator unit, an investigation on several comparator modules was carried out. The lower the threshold value the higher the sensitivity that results in a larger communication range. In the previous project phase (2nd funding period) a low power comparator LMV7271 [88] from Texas Instrument was used [16]. The power consumption was  $16.2 \mu\text{W}$  at a supply voltage level of  $1.8 \text{ V}$ . The comparator needs a signal level change of at least  $30 \text{ mV}$  to detect the right data.

Within this work, a promising comparator TS3021 from STMicroelectronics is evaluated regarding the threshold value. The measurement results show a threshold level of  $3 \text{ mV}$  (corresponding to an incident power of  $P_{\text{in}} = -37 \text{ dBm}$ ). The obtained threshold level is 10 times lower, but in contrast the power consumption is approx. 8 times larger ( $126 \mu\text{W}$  at  $1.8 \text{ V}$ ) compared to the LMV7271. An investigation with the internal comparator of the used microcontroller indicates a further improvement regarding the threshold level. Here, the design and optimization of the value of both resistors  $R3$  and  $R4$  and the capacitor  $C1$  are carried out experimentally. A signal generator is used to generate a digital baseband signal. This signal represents a command from the reader to the tag. If the microcontroller detects a right command, it turns a defined output pin on. According to the measurements the sensitivity of this comparator unit can be given to  $P_{\text{in}} = -39 \text{ dBm}$  which is  $2 \text{ dB}$  better than the TS3021. The power consumption is  $58 \mu\text{W}$  at a voltage level of  $2 \text{ V}$  which is lower compared to the TS3021.

### 5.1.1.1 Current Consumption of the MCU

As presented in the previous section the selection of the microcontroller (MCU) must be done carefully to fulfill the specification of the project concerning low power consumption. Since it is a central management unit, its energy requirement should be well-known. With this knowledge, the energy supply can be correctly dimensioned and the energy consumption can be given for different operating states. Therefore, the power consumption during a communication procedure between the reader unit and the tag is analyzed. For this purpose, a request for the current temperature value is utilized. Fig. 5.3 shows the measured voltage signal  $V_{\text{out}}$  (curve marked with squares) at the output of the demodulator

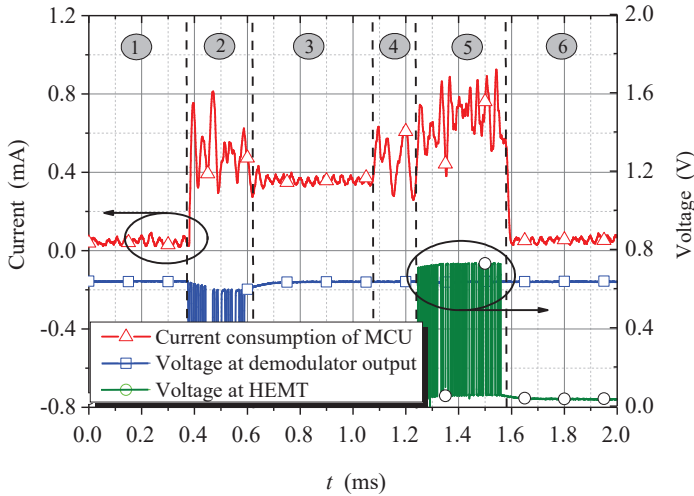


Figure 5.3 Communication sequence of a request from the reader for the current temperature value and the current consumption of the MCU. [QHD4]

unit while the voltage  $V_{GS}$  of the transistor is represented by the curve marked with circles. The corresponding current consumption is also displayed in the same graph (curve marked with triangles). During the measurement a supply voltage of  $V_{cc} = 2\text{ V}$  was applied. It can be noted that the request from the reader occurs within the first 0.22 ms. Due to the processing time of the MCU, the response of the tag has a delay of approx. 0.64 ms. It can be seen that the time varying current consumption can be divided into six states:

- State 1: The MCU is in standby mode (approx. 0.033 mA). This operation mode should be optimized to reduce the power consumption as the transponder is mostly in standby mode. The measured current is approx. 0.033 mA, which is caused by the internal comparator unit. This unit is always switched on in order to detect a command of the reader.
- State 2: The MCU changes its state of operation to active as it receives a command from the reader. In this case, a request for a temperature value. The maximum current can be measured to approx. 0.8 mA.

- State 3: In this state, the request is processed by the MCU. The maximum current is approx. 0.4 mA.
- State 4: The A/D converter is activated for measuring the temperature value and thus the current consumption is increased.
- State 5: The MCU transmits the requested data by switching the gate-source voltage  $V_{GS}$  on and off. The maximum current is approx. 0.93 mA.
- State 6: After all data is transmitted, the communication procedure ends and the MCU switches back to standby mode.

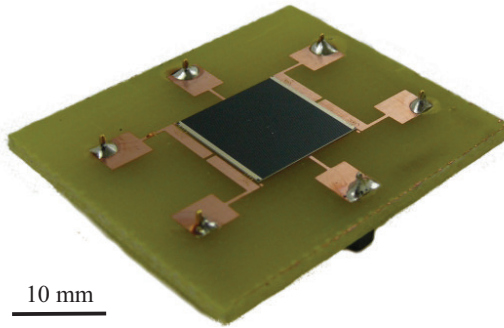
The presented results show that the power consumption of the used microcontroller varies between  $58 \mu\text{W}$  and  $1.85 \text{ mW}$ . In the following subsection, it is to be investigated whether the solar cell can supply the required electrical power.

### 5.1.2 Solar Cell

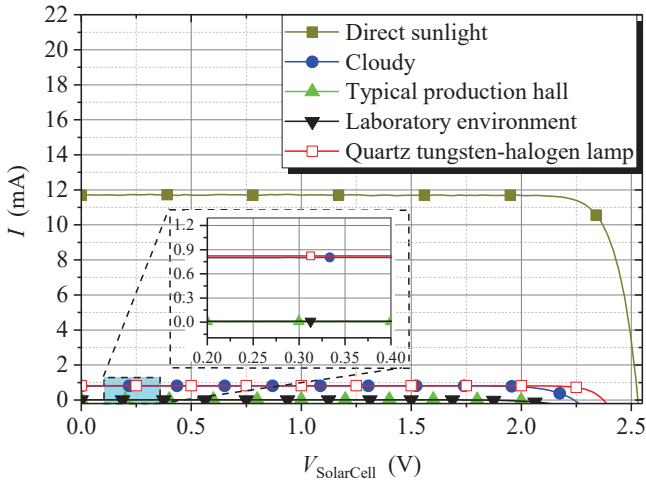
The power supply concept of the RFID sensor tag is based on a simple energy harvesting concept (see Fig. 5.2). An important component is a single metamorphic solar cell. The used multijunction III-V concentrator solar cell C3MJ+ from Spectrolab is a triple junction GaInP/GaInAs/Ge solar cell [24, 89]. According to the AM1.5D, ASTM G173-03 standard this solar cell has a typical efficiency of 39.2 % at  $50 \text{ W/cm}^2$  irradiance. The geometric dimensions of the optical aperture are  $10 \text{ mm} \times 9.9 \text{ mm}$ . The thickness is 0.2 mm. The busbars on the top side are the ground reference with a width of 0.4 mm while the whole bottom side provides the positive voltage. A photograph of the solar cell that is bonded on a PCB for measurement purposes is shown in Fig. 5.4a.

For the characterization of the solar cell, the current-voltage (IV) curves are measured by means of a precise four wire connection measurement setup with a source measure unit Keysight B2900A. Fig. 5.4b depicts the IV characteristics for different lighting scenarios. By applying direct sunlight to the solar cell the short-circuit current is  $I_{SC} = 11.7 \text{ mA}$  while the open-circuit voltage is  $V_{OC} = 2.52 \text{ V}$ . The measurement was carried out at noon on a day in summer. On a cloudy day the solar cell delivers a current of  $I_{SC} = 0.8 \text{ mA}$  and the voltage is  $V_{OC} = 2.23 \text{ V}$ . Under this condition, the sensor tag can provide itself with sufficient energy. It must be noted here that for a proper operation of the tag bypass capacitors are needed.

The IV characteristics are also evaluated within indoor scenarios. Inside a typical production hall (Hannover Centre for Production Technology PZH) as



(a) Photograph of the solar cell mounted on a PCB for measurement purposes.



(b) IV characteristics for different lighting scenarios.

Figure 5.4 Photograph and current-voltage (IV) characteristics of the used solar cell. [QHD3]

well as within a laboratory environment (Institute of Microwave and Wireless Systems) the available ambient light provides a short-circuit current of  $I_{SC} = 9 \mu A$  and the open-circuit voltage is  $V_{OC} \approx 1.8 V$ . This indoor lighting is not sufficient to power the digital circuit since the microcontroller requires at least 1.97 V to

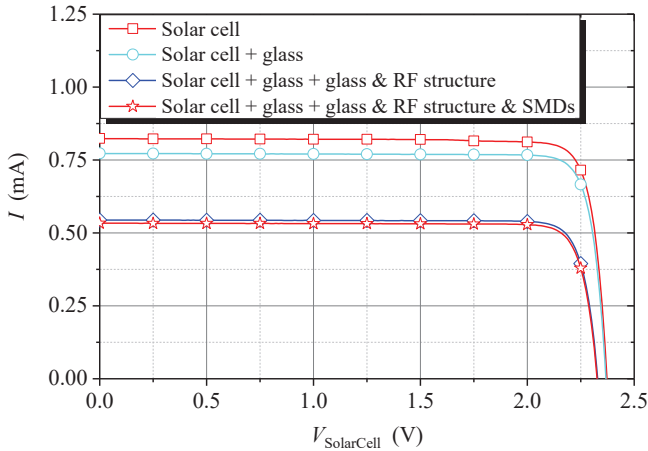


Figure 5.5 Current-voltage (IV) characteristics of the solar cell arranged below various objects. Test condition: laboratory environment with quartz tungsten-halogen lamp (Thorlabs QTH10/M) at a distance of 0.5 m (typical application scenario).

function properly. Thus, an external quartz tungsten-halogen lamp can be used as an additional light source. The selected lamp Thorlabs QTH10/M including a condensing lens offers a broadband illumination in the visible and near-IR portions of the light spectrum (400 - 2400 nm) [90]. The quartz tungsten-halogen bulb requires 10 W at a DC voltage of 12 V. To obtain the IV characteristic of the solar cell, this lamp is positioned 0.5 m away from the solar cell since the communication distance between the reader and the tag is typically in this range. Furthermore, the light spot of the lamp is aligned to the solar cell in such a way as to obtain a maximum short-circuit current. Here, the current is  $I_{\text{SC}} = 0.82$  mA and the voltage is  $V_{\text{OC}} = 2.36$  V. This lighting condition (in low ambient light) is sufficient to power the whole RFID sensor tag.

So far, the solar cell was considered individually. Since the meshed analog front-end as well as the protective glass is positioned above the solar cell, the impact of these components on the IV characteristic must be studied. The measured IV curves of each configuration are depicted in Fig. 5.5. For comparison, the curve marked with squares represents the case of the solar cell without any disturbing elements. Applying a quartz glass substrate (protective



layer of the sensor tag) above the solar cell, the short-circuit current  $I_{SC}$  decreases from 0.82 mA to 0.77 mA. This corresponds to a reduction of 6 %. Here, the transparency of the glass is higher than 90 % within the light spectrum of 450 nm - 1400 nm (see Fig. 3.2). An additional layer of the same quartz glass substrate including the RF circuit (see Fig. 4.30) leads to a further decrease of the short-circuit current to a value of  $I_{SC} = 0.54$  mA. Positioning the realized RF circuit including the three RF components on it, the current is  $I_{SC} = 0.53$  mA while the open-circuit voltage is  $V_{OC} = 2.33$  V (see curve marked with stars). In this study, the whole composition above the solar cell leads to a reduction of the short-circuit current and the open-circuit voltage of 35.2 % and 1.48 %, respectively. The comparison between the maximum required current of the microcontroller (0.93 mA, see Fig. 5.3) and the available current delivered from the solar cell (0.53 mA, laboratory environment with quartz tungsten-halogen lamp) shows a difference of 0.4 mA. Therefore, the lack of current must be provided by an energy storage e.g. a rechargeable battery or a supercapacitor.

### 5.1.3 Energy Storage and Operating Time

Usually, for the harvesting of solar energy an energy harvesting circuit such as an power management IC is used [91]. The function of this component is to optimally manage the energy requirements of a system. A suitable power management IC is for example the bq25505 from Texas Instruments. It has a quiescent current of 325 nA [92]. However, the integration of such a component requires a larger space consumption of the RFID sensor tag that cannot be fulfilled. In order to reduce the complexity of the power management concept, only one diode and one supercapacitor is used. In this work, the energy out of the solar cell is buffered in a supercapacitor DCK-3R3E204T614 from the company Elna. The rated voltage and capacitance is 3.3 V and 0.2 F, respectively. The advantages compared to e.g. rechargeable battery are a rapid charging process and unlimited charging/discharging cycles. The diode is placed between the solar cell and the supercapacitor (see Fig. 5.1.3). Here, a Schottky diode BAT30F4 [93] from STMicroelectronics is used to minimize the discharging process of the supercapacitor during a low light environment. This diode is suitable for this application because of the low forward voltage drop ( $V_F = 0.18$  V at  $I_F = 0.5$  mA) and a reverse leakage current lower than approx. 1  $\mu$ A at room temperature.

One possible method of evaluating the efficiency of the used energy harvesting concept is to measure the operating time of the RFID sensor tag. Fig. 5.6 shows

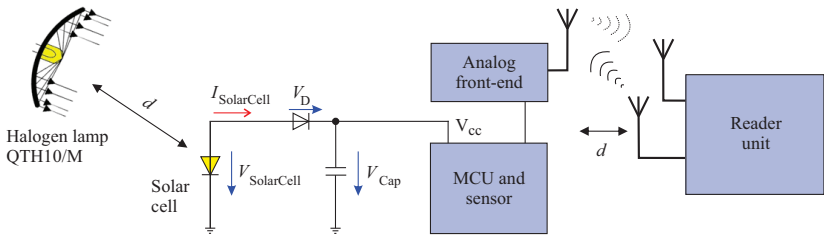


Figure 5.6 Measurement setup for the evaluation of the operating time of the RFID sensor tag. Distance  $d = 0.5\text{m}$ .

the measurement setup. The meshed antenna and analog front-end is arranged above the solar cell as in the later assembly of the tag. The reader unit and the halogen lamp are placed in a distance of  $d = 0.5\text{m}$  to the tag. This distance represents the typical communication range of the application scenarios. During the experiment, the voltage of the supercapacitor  $V_{\text{Cap}}$  and the current from the solar cell  $I_{\text{SolarCell}}$  is monitored. The time sequence is depicted in Fig. 5.7. At first, the lamp is switched on at a time of  $t = 0\text{ s}$  and the forward current of the diode changes to  $I_{\text{SolarCell}} = 0.54\text{ mA}$ . The voltage of the supercapacitor increases and reaches a level of  $V_{\text{Cap}} = 1.97\text{ V}$  at a time of  $t = 480\text{ s}$  (at bright ambient light such as outdoor environment this voltage level will be reached in approx. two seconds). At a voltage of  $V_{\text{Cap}} \geq 1.97\text{ V}$  the microcontroller wakes up and waits for a command. During this period, the internal comparator unit is always on and the current consumption is approx.  $33\text{ }\mu\text{A}$ . After a time of  $t = 1212\text{ s}$  (20.2 min.) the current delivered from the solar cell is  $I_{\text{SolarCell}} = 0.05\text{ mA}$  and the voltage is  $V_{\text{Cap}} = 2.13\text{ V}$ . In this lightning scenario the maximum voltage level of the supercapacitor is reached ( $V_{\text{Cap}} = V_{\text{SolarCell}} - V_{\text{D}}$ ). After the capacitor has been charged, the lamp is switched off to simulate a low light environment. In doing so, the maximum operating time of the tag can be determined. While the supercapacitor powers the microcontroller the current is in the range of  $I_{\text{SolarCell}} \approx -1.5\text{ }\mu\text{A}$ . This means the supercapacitor is discharged via the solar cell. During the discharging interval, no communication is occurred between the reader and the tag. At a time of  $t = 2060\text{ s}$  (34.33 min.) the voltage has dropped to a value of  $V_{\text{Cap}} = 1.91\text{ V}$ . This voltage level is not sufficient to power the microcontroller. Thus, the maximum operating time can be given to 14.13 minutes. For comparison, the same supercapacitor is discharged itself

from 2.1 V to 1.9 V in more than 4 hours.

Now the operating time for two different scenarios is investigated. In analogy to the previous test procedure, the supercapacitor is charged for approx. 20 minutes. Afterwards the light source is switched off. During the discharging time, a communication between the reader and the tag should be accomplished. Therefore, in scenario 1 the ID number of the tag is to be transmitted while in scenario 2 an exchange of the ID number and the data of the acceleration sensor should be carried out. The communication procedure was as follows: the reader unit transmits a request for the data. The microcontroller wakes up from the sleep mode, processes the request, transmits a respond to the reader and goes to sleep mode until the next incoming request. This communication procedure is repeated every second. As a result, the operating time for scenario 1 and scenario 2 is 13.3 minutes and 12.56 minutes.

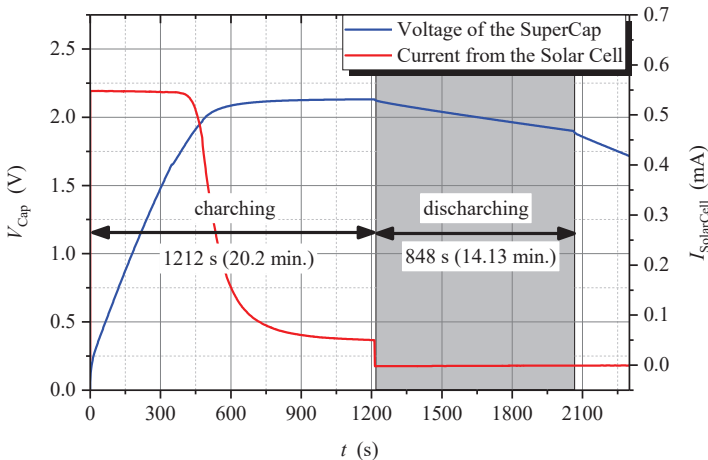


Figure 5.7 Measured voltage  $V_{Cap}$  of the supercapacitor and current  $I_{SolarCell}$  of the solar cell while a charging and discharging procedure.

### 5.1.4 Realization of the Baseband Unit on a 3D-MID

After the selection of the components the design of both the layout and the three-dimensional housing of the tag carried out. In this work, the housing is a three-dimensional molded interconnect device (3D-MID). This device simultaneously is used as a circuit carrier. Fig. 5.8 shows a 3D CAD model illustrating the 3D-MID and the placement of the components and the conductor paths on it. The overall dimensions of the housing is  $13.3\text{ mm} \times 12.9\text{ mm} \times 4.15\text{ mm}$ . It can be noted that the used components take up approx. half of the available space (inner dimensions:  $10.5\text{ mm} \times 10.9\text{ mm}$ ). The other half is mostly covered by the supercapacitor with the dimensions of  $6.8\text{ mm}$  in diameter and  $1.8\text{ mm}$  in height. The layout consists of two layers. The orange colored lines are on the component side (layer 1) while the brown colored lines are on the layer 2. The connection between both layers are realized by vias. Furthermore, there are strip lines on the side wall of the housing in order to connect the baseband unit with the analog front-end and the solar cell. These interconnections are a part of the assembly concept that will be discussed in Sec. 5.1.5.

For the realization of the circuit, a laser direct structuring (LDS) process [23]

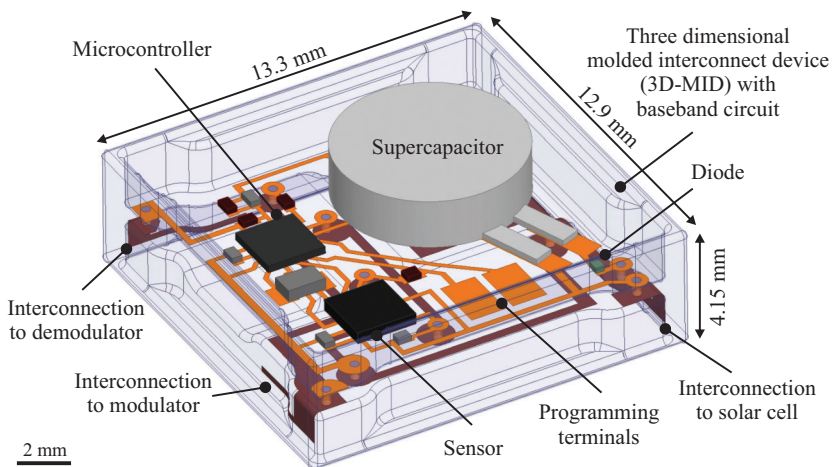


Figure 5.8 3D CAD model of the baseband unit on the housing.

is used. Each fabrication step is illustrated in Fig. 5.9. The three fabrication processes can be described as follows: First, the housing is produced from an injection molding material, which is provided with a special additive for laser activation. In this work, the material named Vectra E840i LDS is utilized. In the second step, the thermoplastic material is then activated by a laser beam. Within this production step, the laser drills through the plastic part for the realization of vias. In this case, the inner via surface is activated simultaneously. Afterward, the housing is metallized in the electroless plating process. The area roughened by the laser enables a high adhesive strength between the plastic and the metallization. Three different metallization layers are used: copper (approx. 5  $\mu\text{m}$ ), nickel (approx. 3  $\mu\text{m}$ ) and gold (approx. 0.1  $\mu\text{m}$ ). In this way, conducting paths can be realized directly on the surface of the plastic part and a reliable connection between both layers can be achieved.

Once the housing/circuit carrier has been manufactured, the subsequent assembly of the circuit with surface mounted devices (SMDs) follows. Fig. 5.10

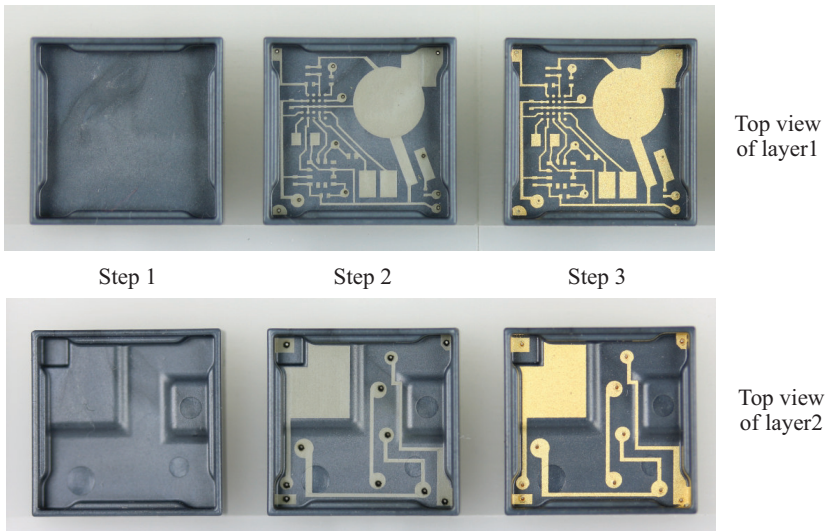


Figure 5.9 Photograph of the housing illustrating the three fabrication steps of the laser direct structuring (LDS) process.

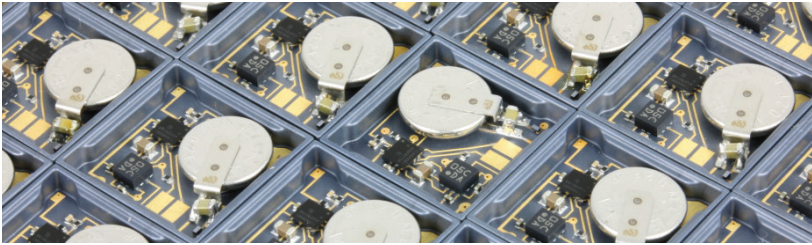


Figure 5.10 Photograph of the fabricated baseband unit on the 3D housing.

shows a photograph of the mounted components on the 3D-MID. Since the available space is limited the package size 0201 (imperial,  $0.6 \text{ mm} \times 0.3 \text{ mm}$ ) was selected for the diode, all resistors and most capacitors. The capacitors  $C_2$  and  $C_6$  have a package size 0603 (imperial,  $1.6 \text{ mm} \times 0.8 \text{ mm}$ ). The package of the triaxial acceleration sensor is called land grid array (LGA). The smallest available package of the microcontroller is the type named ball grid array (BGA). A reflow soldering process with appropriate reflow soldering thermal profile is utilized in order to obtain a reliable connection between electrical components and contact pads. All fabrication steps described in this subsection was carried out by the company Tepresa GmbH.

### 5.1.5 Assembly of the Tag

All important circuit parts have been presented in detail up to this point. The manufacturing technology used was also discussed. Finally, the parts have to be assembled according to the design concept as shown in Fig. 2.3 in order to obtain a well-functioning RFID sensor tag.

A photograph of the tag after the assembly process is depicted in Fig. 5.11 on the left-hand side. Here, the biggest challenge is a proper and reliable connection between the solar cell, the RF circuit and the housing. The starting point is the 3D housing with the baseband circuit. In the first step, the backside of the solar cell (positive terminal) is attached on the housing by conductive adhesive. A non-conductive adhesive is applied along one edge of the solar cell in order to avoid short-circuits throughout the subsequent bonding process. After a curing process, one busbar of the solar cell is electrically connected with a contacting pad on the housing (see yellow marked area in the upper half of the photograph

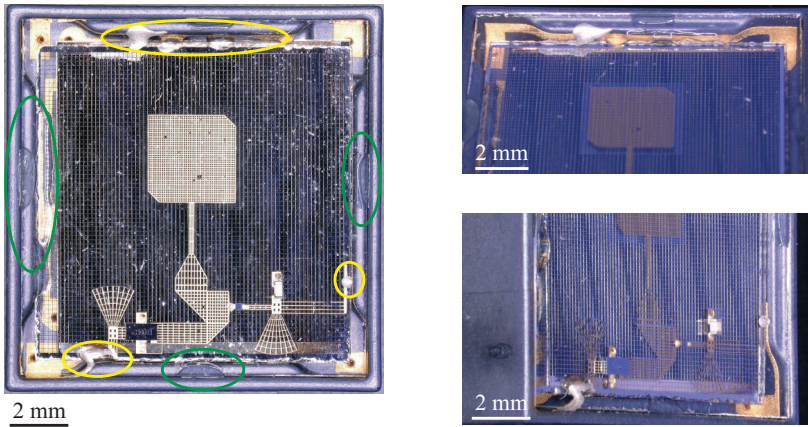


Figure 5.11 Photograph of the tag after the assembly process. Left: top view; conductive adhesive used within yellow marked areas and non-conductive adhesive used within green marked areas. Upper right: 3D view of the adhesive area of the solar cell. Lower right: 3D view of the adhesive areas of the modulator and demodulator unit.

and upper right photograph in Fig. 5.11). Within this step, conductive adhesive is applied on the second busbar. Subsequently, the quartz glass with the RF circuit is placed on the solar cell. After a curing process of the conductive adhesive an electrical connection between the ground plane of the RF circuit, the busbars/fingers of the solar cell and the ground terminal of the baseband unit is obtained. Afterwards, a bonding step is applied to the connecting pads on the top layer of the RF circuit and the pads on the side wall of the housing (see yellow marked areas in the lower half of the photograph and lower right photograph in Fig. 5.11). Finally, a quartz glass is attached on the supporting areas of the housing by non-conductive adhesive (see green marked areas on the photograph). The use of a protective layer on both sides of the housing prevents the tag from being damaged by environmental influences.

### 5.1.6 Conclusion

The most important results of this section are:

- The use of an ultra-low-power microcontroller (MCU) MSP430FR5738 from Texas Instruments as the core unit of the baseband circuit reduces the number of the electrical components and the space required for the

circuit. The MCU includes a nonvolatile memory, a temperature sensor and a comparator unit.

- The power consumption of the MCU varies between 58  $\mu\text{W}$  and 1.85 mW at a supply voltage of  $V_{\text{cc}} = 2 \text{ V}$ .
- A single multijunction solar cell C3MJ+ from Spectrolab is used as the power supply, which has a good characteristic to power the tag in daylight in an outdoor environment. In an indoor environment an additional light source, e.g. a halogen lamp is needed to operate the tag properly.
- The components (meshed analog circuit including the RF components and the protective glass) positioned above the solar cell leads to a reduction of the short-circuit current and the open-circuit voltage of 35.2 % and 1.48 %, respectively.
- By using a supercapacitor as an energy storage, the operating time of the tag in low light environments is approx. 13 minutes. During this time, a communication between the reader and the tag is periodically carried out.
- The use of the 3D-MID technology results in a compact tag design with a high degree of integration.

## 5.2 Reader Unit

So far, all components of the RFID sensor tag have been studied. For a communication and data exchange with the tag a reader unit is required. Since an operating frequency is defined within the 24 GHz ISM band and commercially available RFID reader units operate at much lower frequencies, a reader must be developed within this work. There are no special requirements on this unit regarding the overall dimensions or the use of low power components. Thus, the unit can be realized by utilizing commercially available components. A block diagram of a reader unit is shown in Fig. 5.12. This unit can be divided into two parts: analog unit and digital unit. The analog unit is responsible for the modulation of the baseband signal and the demodulation of the backscattered signal from the tag. The digital unit generates the data to be transmitted and process the received information.

Commercially available radar transceivers such as the K-MC1 from RFbeam Microwave GmbH [94] have a similar topology to the presented block diagram of



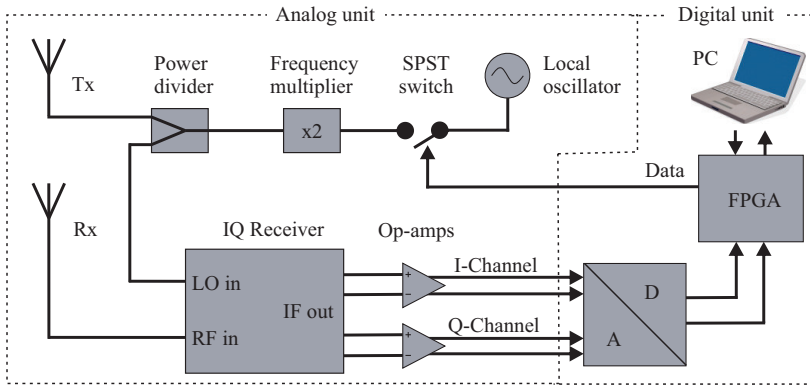


Figure 5.12 Block diagram of the developed 24 GHz reader unit.

the analog unit and basically it is suitable for the use within this project. However, the Tx and Rx antenna have a narrow field of view, which leads to a shorter communication distance with larger angular ranges. The 3 dB beamwidth in the E-plane and H-plane is  $12^\circ$  and  $25^\circ$ , respectively. Furthermore, the antennas are linear polarized, and they cannot be replaced by other antennas. Therefore, the analogue unit shall consist of an assembly of individual, self-developed and commercially available components. In doing so, a flexible configuration of the RF properties can be implemented. In the following individual components are discussed in detail.

### 5.2.1 Analog unit

As shown in Fig. 5.12 the analog unit consists of a local oscillator, a Single Pole Single Throw (SPST) switch, a frequency multiplier, a power divider, a power amplifier, a transmitting antenna, a receiving antenna, an IQ receiver and an operational amplifier circuit. Apart from the antennas and the operational amplifier circuit, all components used are commercially available. These parts can be connected modularly with each other. A cost-effective solution is to use a local oscillator with an output frequency of  $f = 12.024$  GHz and a frequency doubler to achieve a carrier frequency within the 24 GHz ISM band. The SPST switch is used to turn the signal on and off in accordance with the data cycle. Since the upper frequency limit of this switch is  $f = 16$  GHz, it is positioned

after the source. On the one hand, a power divider routes the signal to the transmitting antenna via a power amplifier and on the other hand to the LO input of an IQ receiver. The backscattered signal from the tag is transmitted from the receiving antenna to the RF input of the IQ receiver. The down converted baseband signal is amplified by an additional op-amp before being processed by the digital unit. The characteristics of individual components is presented below.

### 5.2.1.1 Local Oscillator

In this work a local oscillator unit MKU LO 12 PLL from the company Kuhne electronic GmbH is utilized. This unit has a phase lock loop (PLL) stabilized crystal oscillator. The output frequency of  $f = 12.024$  GHz is fixed and the rated output power is  $P_{\text{out}} = 15.4$  dBm. The module requires a DC voltage supply of 12 V and a current of 260 mA. The key parameters specified in the data sheet have been verified by measurements.

### 5.2.1.2 Absorptive SPST Switch

The task of the switch is to turn the generated signal of the local oscillator on and off. The selected component is an absorptive Single Pole Single Throw (SPST) switch SW1AD-16 from Pulsar Microwave Corporation. By using a transistor-transistor logic (TTL) the switch can be changed between two states. The switching time is specified as 100 nsec, which is sufficient for the application of this work. With logic "0", the input signal is transmitted to the output. In this case, the measured insertion loss is 2.3 dB and the amplitude of the input reflection coefficient is lower than -15 dB at a frequency of  $f = 12$  GHz. In state "1" the switch is switched off and the RF signal is absorbed. The isolation between the input terminal and output terminal is higher than 90 dB at  $f = 12$  GHz. The module requires a DC voltage supply of  $\pm 5$  V and a current of  $\pm 30$  mA.

### 5.2.1.3 Frequency Multiplier

Since the operating frequency of the local oscillator is  $f = 12.024$  GHz, a frequency multiplier is needed. A frequency doubler MKU X2 1224 from Kuhne electronic GmbH is selected. The frequency spectrum and the output power of this device are verified by a measurement using a spectrum analyzer. The output power is  $P_{\text{out}} = 19$  dBm at a frequency of  $f = 24.048$  GHz. A DC

voltage supply of 12 V is required for operation and the current consumption is 400 mA.

### 5.2.1.4 Power Divider

In this work, a two-way power divider from the company Pulsar Microwave Corporation with the designation PS2-50-450/8S is used. The input signal is divided into two signals with the same power and phase. The return loss at all ports is better than 15 dB. At a frequency of  $f = 24$  GHz the insertion loss between the input terminal and one output terminal is 3.5 dB. Here, the isolation between both outputs is lower than -25 dB.

### 5.2.1.5 Antennas

One patch antenna each is used for the transmitting and receiving antenna. This type of antenna was chosen because of the simple manufacturing process as it can be manufactured in-house. As with the patch antenna of the tag, both antennas should have a right hand circular polarization. Therefore, the design is similar to the patch antenna of the tag (see Fig. 4.12). In this case, the antenna is opaque and the used RF laminate is RT/duroid 5880 from Rogers Corporation. The thickness of the laminate is chosen to 0.254 mm. A dielectric constant of  $\epsilon'_r = 2.2$  and a dissipation factor of  $\tan \delta = 0.0009$  is used in the simulation

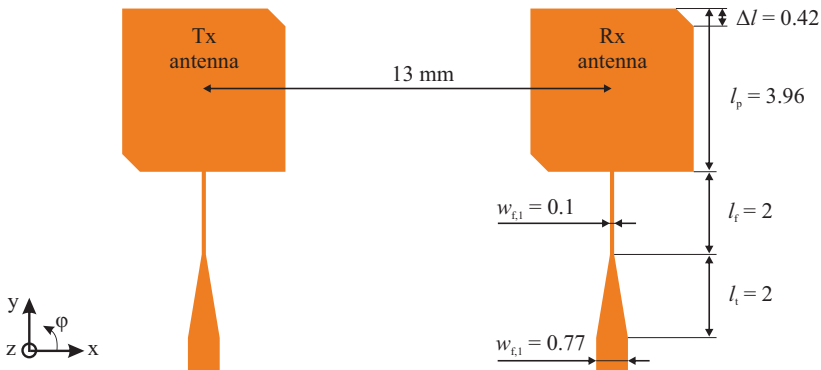
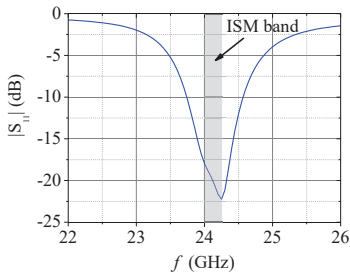


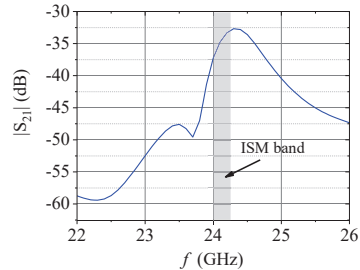
Figure 5.13 Layout of the transmitting antenna and receiving antenna of the reader unit. All dimensions in mm.

model. The layout of both antennas having the same geometric dimensions is depicted in Fig. 5.13. The Tx antenna is arranged at a distance of 13 mm from the Rx antenna because of, among other things, the geometric dimensions of the used end launch connectors. Both square patch antennas are fed by a microstrip line. The first section of the feed line has a width of  $w_{f,1} = 0.77$  mm, which corresponds to a characteristic impedance of  $Z = 50 \Omega$ . The sections with the length  $l_t$  and  $l_f$  is designed in such a way to achieve a good input impedance matching.

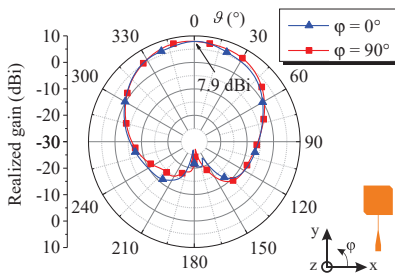
Fig. 5.14 shows the simulation results of the patch antenna. The input reflection coefficient is depicted in Fig. 5.14a. At the frequency of  $f = 24.05$  GHz the magnitude of the input reflection coefficient is  $|S_{11}| = -19$  dB. The -10 dB



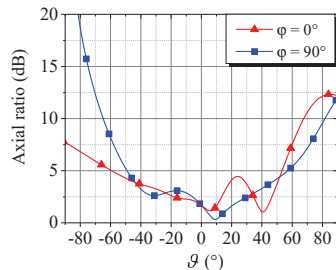
(a) Input reflection coefficient.



(b) Coupling between both antennas.



(c) Radiation pattern at the frequency  $f = 24.05$  GHz.



(d) Axial ratio at the frequency  $f = 24.05$  GHz.

Figure 5.14 Simulation results of the circularly polarized square patch antennas on the RT/duroid 5880 laminate.

bandwidth is 3.4 %. Since both antennas are positioned next to each other, the coupling is analyzed and it is shown in Fig. 5.14b. At the operating frequency the magnitude is  $|S_{21}| = -35$  dB. This characteristic ensures that the input of the receiver will not be damaged by the maximum transmitted power level in the range of 20 dBm EIRP. The radiation pattern for the horizontal and vertical plane are shown in Fig. 5.14c. A maximum realized gain value of 7.9 dBi is achieved at the main direction. Since the antenna is circularly polarized another key parameter that must be evaluated is the axial ratio. Fig. 5.14d depicts the axial ratio as a function of the angle  $\vartheta$  at a frequency of  $f = 24.05$  GHz. It can be noted that the axial ratio is lower than 5 dB for an angle range of  $-40^\circ \leq \vartheta \leq 53^\circ$ , which is adequate for the RFID application within this work.

### 5.2.1.6 IQ Receiver

For the down conversion of the RF signal to baseband an IQ mixer/receiver is required. In this way, the data exchange can be carried out regardless of the distance between the reader and the tag. When using only one mixer, the problem arises that with a phase offset of odd-numbered multiples of  $90^\circ$  between the

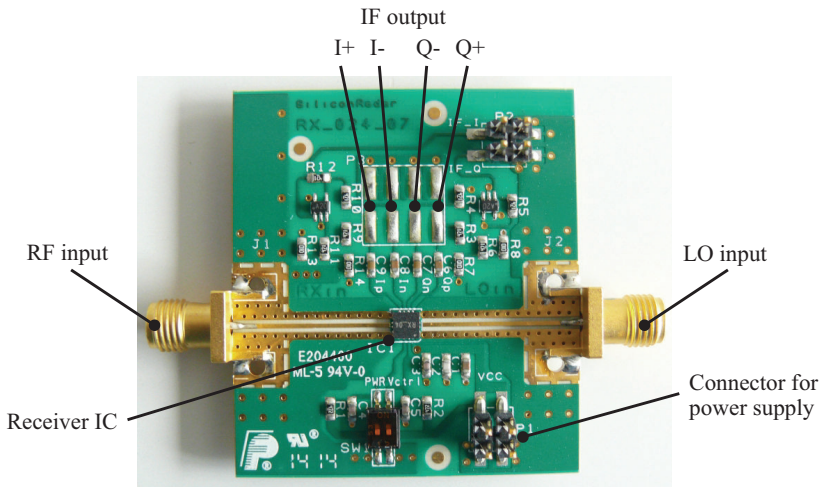


Figure 5.15 Photograph of the used evaluation board equipped with an IQ receiver IC from Silicon Radar GmbH.

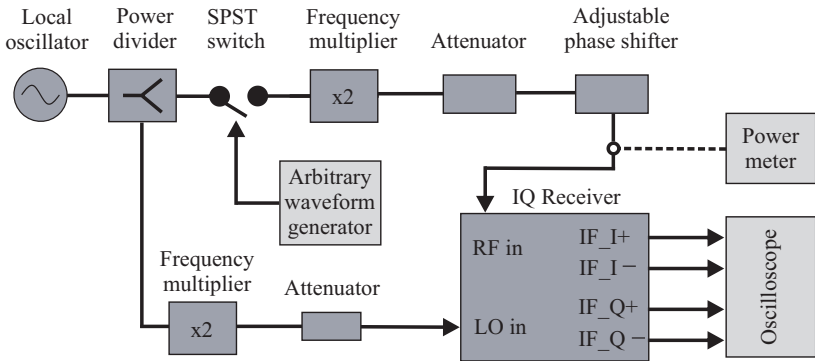


Figure 5.16 Block diagram of the measurement setup for the evaluation of the IQ receiver.

backscattered and the transmitted signal, the output signal of the frequency mixer is zero. In this work, an IQ receiver IC from Silicon Radar GmbH [95] is utilized. A photograph of an evaluation board equipped with the receiver IC and external circuit is shown in Fig. 5.15. This commercially available board is utilized as part of the reader unit. The receiver IC is an integrated IQ receiver circuit including a low noise amplifier (LNA). It operates in the 24 GHz ISM band and requires a supply voltage of  $V_{cc} = 2.5$  V and a supply current of  $I_{cc} = 13.5$  mA.

For the evaluation of the IQ receiver, a measurement setup according to Fig. 5.16 is utilized. Some components such as local oscillator, SPST switch, frequency multiplier and power divider are already presented in the previous subsections. Since the amplitude of the RF signal is fixed attenuators are used to adjust the output power. The function of the adjustable phase shifter is to emulate the location dependency in a wireless communication channel. In order to generate a modulated signal an arbitrary waveform generator AM300 from Rohde & Schwarz is used. The down converted signal is monitored on an oscilloscope. The measured output signals of the in-phase (I-channel) and quadrature (Q-channel) channel are depicted in Fig. 5.17. In this case, a square wave signal with a frequency of  $f = 100$  kHz is at the output of the signal generator. The input power at the RF input terminal of the IQ receiver is  $P_{in} = -44$  dBm. This value is determined by a power meter. Additionally, the phase of the modulated input signal is adjusted by means of the phase shifter in such a way that the signal amplitudes on the two output channels are

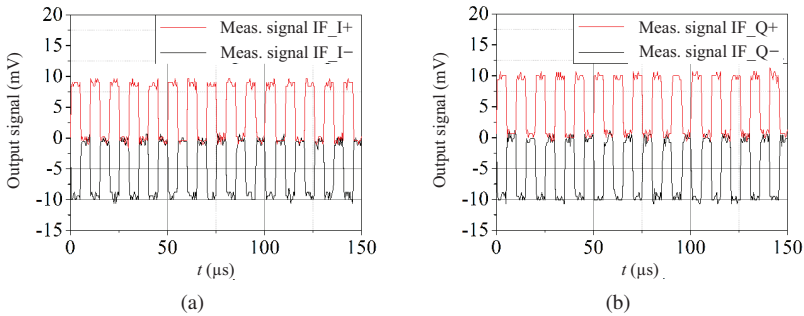


Figure 5.17 Measured output signal of (a) the in-phase (I-channel) and (b) quadrature (Q-channel) channel. Input power level at the RF input of the receiver is  $P_{in} = -44$  dBm.

approximately the same. The obtained results agree well with the expected values calculated by using characteristic parameters of each component that are either specified in the data sheet or determined by own measurements. In this case, the difference is 4 mV.

### 5.2.1.7 Operational Amplifier

A goal of this work is to develop a reader unit with the highest possible sensitivity value that leads to a long communication distance. Therefore, the demodulated low frequency signal must be amplified by an operational amplifier before it is routed to an analog digital converter. Since the analog digital converter has a differential input for the I and Q channel, the amplifier circuit should also provide a differential output. A suitable IC component is the THS4503 from Texas Instruments. It has a high slew rate and a low input voltage noise compared to other IC devices.

A circuit diagram of the designed amplifier circuit is shown in Fig. 5.18. The development of the circuit is carried out using the SPICE-based simulation software TINA-TI from Texas Instruments. The source signals are modelled according to the demodulated signal of the IQ receiver. In this case, a square wave signal with a frequency of  $f = 100$  kHz. The capacitors at the input and the output of the circuit represent a high pass filter (HPF). The high-pass filtering reduces the influence of static reflections, which occur as DC voltage at the output of the IQ receiver. By dimensioning the resistors R1, R2, R3 and R4,

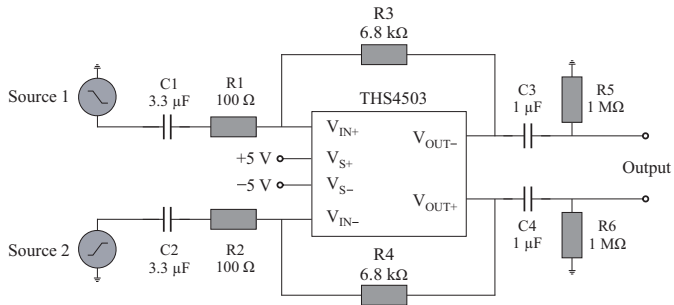


Figure 5.18 Circuit diagram of the fully differential amplifier with external circuitry obtained by a SPICE-based analog simulation software TINA-TI from Texas Instruments.

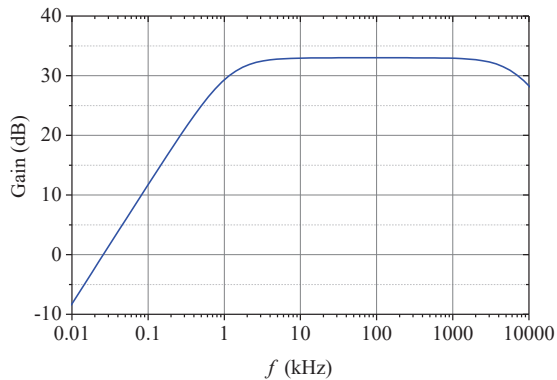


Figure 5.19 Simulated gain as a function of the frequency of the amplifier circuit according to Fig. 5.18.

the gain of the circuit can be changed. The resistors R5 and R6 simulate a high input impedance of the ADC.

The simulated gain (ratio of output voltage to the difference of the input voltages) as a function of the frequency of the amplifier circuit is depicted in Fig. 5.19. A high-pass characteristic can be observed up to a frequency of approx. 2 MHz. At the desired frequency of  $f = 100$  kHz a gain value of 33 dB



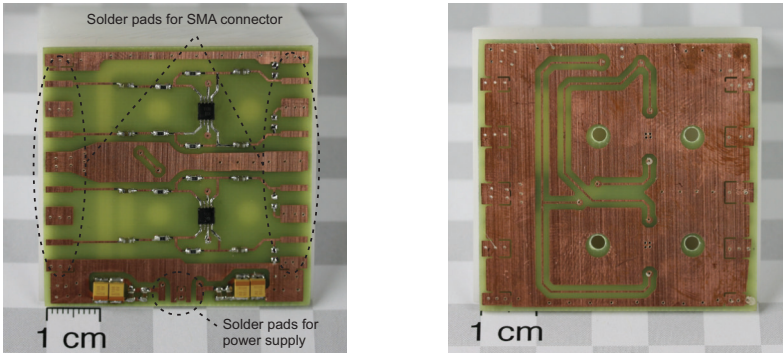


Figure 5.20 Realized amplifier circuit on a FR4 substrate. Left: top layer. Right: bottom layer.

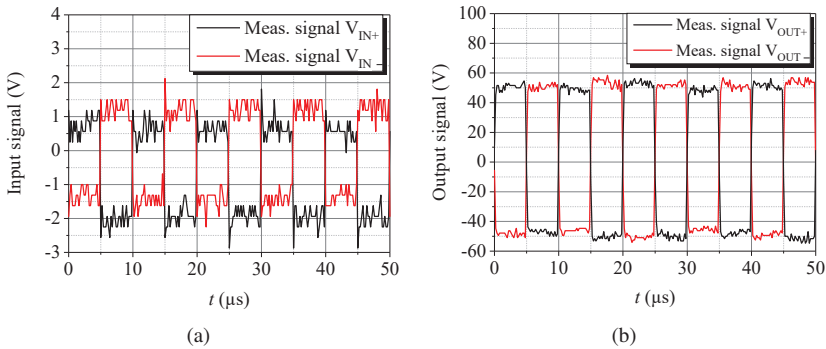


Figure 5.21 Measured (a) input signal and (b) output signal of the realized amplifier circuit.

is achieved. This corresponds to a ratio of 44.7 between the output voltage and the input voltage.

Fig. 5.20 shows the realized amplifier circuit fabricated on a FR4 substrate. There are two identical amplifier circuits. One for the I channel and one for the Q channel. Several capacitors are placed on the lower region of the board for the power supply. In order to verify the simulated results a measurement setup including an arbitrary signal generator AM300 from Rohde & Schwarz and an oscilloscope is used. The signal generator is configured to provide a

square wave signal with a frequency of  $f = 100$  kHz. The signal at the input of the amplifier circuit is depicted in Fig. 5.21a. The curves contain a certain noise component that is generated by the measurement instruments. The output signals are plotted in Fig. 5.21b. It can be concluded that the simulated gain factor of approx. 45 can be verified by the measurements.

### 5.2.1.8 Realization of the Analog Unit

So far, all important components of the analog unit of the reader are presented. The modules are now placed in a housing and interconnected according to the block diagram of the reader (see Fig. 5.12). Fig. 5.22 shows the realized analog unit of the reader from the front view and the top view. Each RF unit is integrated in a metal housing that acts as a shielding against possible electromagnetic interference. The RF units are connected via appropriate coax cables. A power supply and several voltage regulators complete the whole reader unit.

When operating the reader, it must be ensured that the transmitted power including the antenna gain does not exceed the regulation prescribed by the

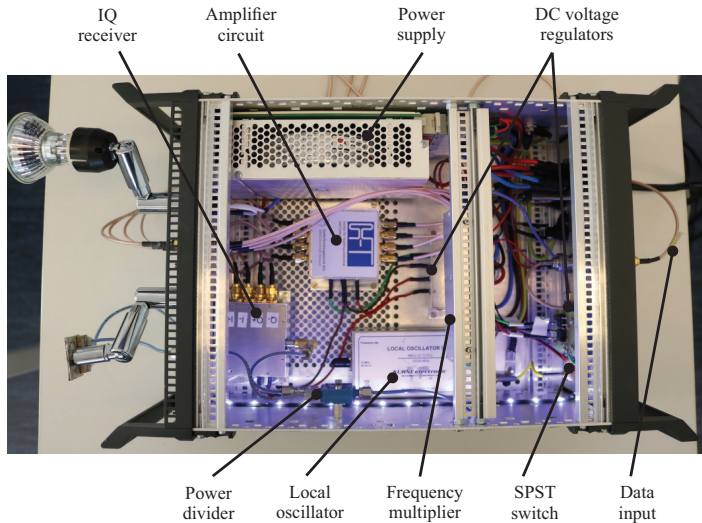


Figure 5.22 Photographs of the realized reader unit.

Bundesnetzagentur for the 24 GHz ISM band. For this reason, the power level of the reader should be limited to  $P_{\max} = 20$  dBm (EIRP) (see Sec. 2.2). In this case, the limitation is realized by discrete attenuators and the maximum transmit power of the reader is  $P_{\max} = 14.5$  dBm.

### 5.2.2 Digital unit

The digital unit of the reader is shown on the right side of the Fig. 5.12 (see Section 5.2). It consists of three main components:

- An analog-to-digital converter (ADC)
- A Field Programmable Gate Array (FPGA) unit
- A personal computer (PC) that controls the connected devices and provides a graphical user interface (GUI).

In this work, a PXI (PCI eXtensions for Instrumentation) system from National Instruments is used. In this way, suitable components such as a FPGA module (NIPXIE-7965R) and a baseband transceiver adapter module (NI 5781) is connected to the system using the PCI (Peripheral Component Interconnect) data bus. When receiving the data from the tag the demodulated analog signal at the output of the IQ receiver is digitized by the baseband transceiver. The data is routed to the FPGA module. This unit processes the received data and the payloads are forwarded to the PC for further evaluation. Fig. 5.23 shows a screenshot of the developed graphical user interface (GUI) implemented using the graphical programming software LabVIEW from National Instruments. This LabVIEW GUI is used for displaying the information and executing commands (e.g. request for sensor data) by the user. In the latter case, the data is transferred to the FPGA and the digital output terminal of the baseband transceiver controls the SPST switch of the analog unit. The GUI provides the following functionalities:

- Request and display of the tag ID number
- Request and display of the tag temperature
- Request and display of the current data of the triaxial acceleration sensor
- Request for the stored data on the memory of the tag and write user-defined data on the tag.

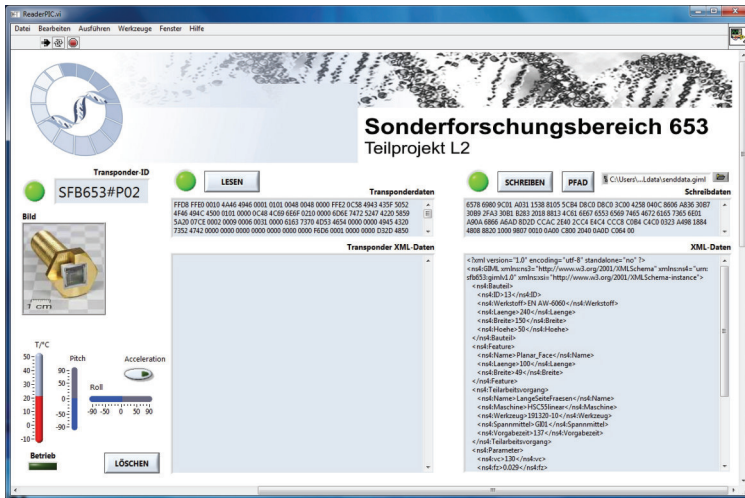


Figure 5.23 Screenshot of the developed graphical user interface (GUI) implemented with LabVIEW.

### 5.2.3 Communication Protocol

A proprietary communication protocol and a definition of the data frame of a data block to be transmitted between the reader and the tag were implemented and tested in the previous funding period [16]. Within the scope of this work, the communication procedure as well as the data frame have basically been maintained. However, an adaptation to the current hardware is carried out. The procedure can be described using an example. Fig. 5.24 shows a possible communication sequence for a transmission of the sensor data. The reader unit is depicted on the left-hand side while the sensor tag is on the right-hand side. First, the reader transmits a request for the sensor data. Meanwhile, the tag is in the idle status and is waiting for a command. If the command is correctly received and decoded, the tag transmits the requested data back to the reader. Once the procedure is successfully completed, the tag changes its status from active to idle and waits for the next command. However, errors may occur during each transmission sequence caused by the operating environment, for example in a manufacturing area. Therefore, the procedure must be repeated in the following cases:

- The command from the reader is not received by the tag.
- The response from the tag is not received by the reader.
- The command/response is received incorrectly by the tag/reader.

For the first two cases, a parameter *time out* is defined. After a certain time the reader transmits the command once again. To avoid an endless loop, a stop criterion is provided. Furthermore, a checksum is implemented at the end of the data frame to determine the correctness of the command/data. Thus, possible packet errors can be detected. These two methods ensure that the communication process can be carried out successfully.

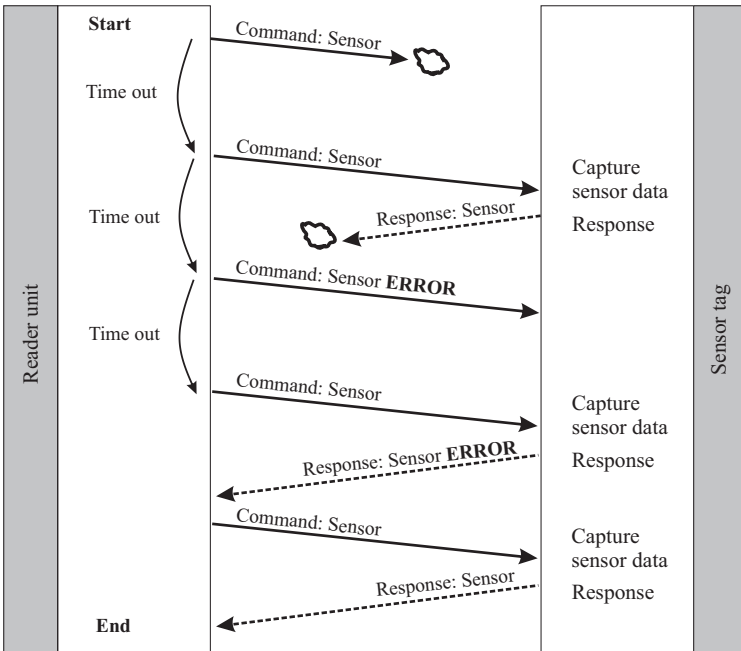


Figure 5.24 Communication procedure of a request for the sensor data.

### 5.2.4 Conclusion

The most important findings of the reader unit are:

- The analog unit consists mainly of commercially available components in order to flexibly dimension the system. Each component is characterized in details.
- The circularly polarized patch antennas and the operational amplifier circuit are self-developed units.
- The realized amplifier circuit has a gain value of 33 dB at a frequency of  $f = 100$  kHz.
- The maximum transmitted power of the reader is adjusted to be  $P_{\max} = 14.5$  dBm.
- The proprietary communication protocol from the previous funding period is adapted to the current system functionality.
- A graphical user interface (GUI) is implemented with LabVIEW in order to control and evaluate the data exchange between reader and tag.

### 5.3 Evaluation of the RFID System

A block diagram of the whole RFID system is depicted in Fig. 5.25 in order to provide an overview. The developed system consists of an RFID sensor tag and a reader unit. The main components of each unit are already discussed in details in previous sections. In the following, the overall system is evaluated with regard to its sensitivity and thus the maximum communication range between the tag and the reader.

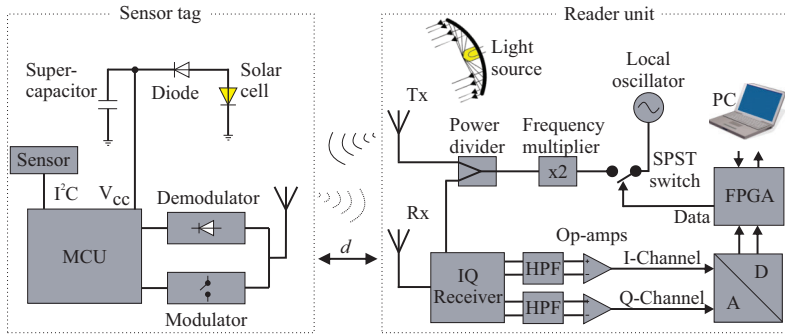


Figure 5.25 Block diagram of the 24 GHz communication system. [QHD1]

#### 5.3.1 Sensitivity of the Reader

The sensitivity of the reader is an important parameter in order to determine the maximum achievable communication distance of the RFID system. For this reason, a measurement setup according to Fig. 5.26 is used for an evaluation. A similar structure has already been utilized for the evaluation of the IQ receiver (see Fig. 5.16). The RF components are already discussed in Sec. 5.2. An arbitrary waveform generator is used to generate an appropriate data signal that emulates the tag response. Different attenuators placed in the receiver path represent the path loss and the adjustable phase shifter emulates the location dependency in a wireless communication channel. By means of a power meter, the amplitude of the received signal can be accurately determined. The down converted signal is amplified and routed to the digital unit. If the data is received correctly, the graphical user interface reports a positive message. In order to determine the minimum detectable signal level, attenuators are gradually

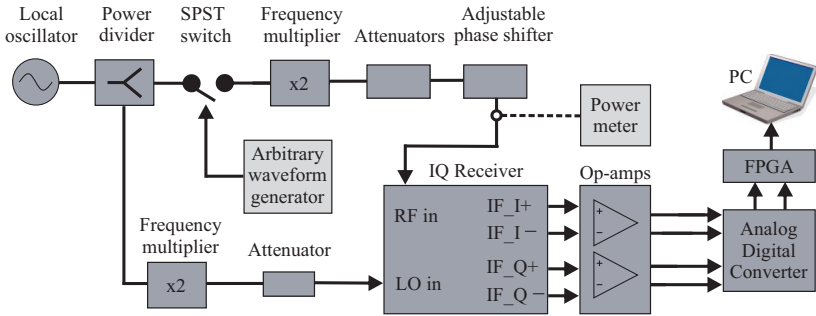


Figure 5.26 Block diagram of the measurement setup for the evaluation of the sensitivity of the reader.

added to the IQ receiver input. At a power level of  $P_{in} = -90$  dBm a response signal is still detectable. A proper demodulation is no longer possible below  $P_{in} = -91$  dBm. Hence, the achieved sensitivity of the reader unit can be given to  $P_{Reader, min} = -91$  dBm.

By rewriting the Eq. 4.14 to Eq. 5.1 the maximum achievable communication distance can be given to  $d_{R, max} = 1.3$  m (assumption: no multipath propagation):

$$d_{R, max} = \sqrt[4]{\frac{P_{tx} G_R^2 \lambda_0^4 G_{Tag}^2}{P_{rx} (4\pi)^4} |\Gamma_1 - \Gamma_2|^2}. \quad (5.1)$$

The following values are used for the calculation: transmitted power of the reader  $P_{tx} = 14.5$  dBm, antenna gain of the reader  $G_R = 7$  dBi, antenna gain of the tag  $G_{Tag} = 4.4$  dBi, received power at the reader  $P_{rx} = -91$  dBm, input reflection coefficient of the mismatched state  $|\Gamma_1| = -3$  dB and input reflection coefficient of the matched state  $|\Gamma_2| = -31$  dB. This calculation assumes that the tag always transmits a response to the reader. Since the maximum communication range can be limited by the sensitivity of the tag, this will be examined in the following.

### 5.3.2 Sensitivity of the Tag

In order to evaluate the sensitivity (minimal detectable signal level) of the realized RFID sensor tag, a measurement setup according to Fig. 5.27 is used and the following steps are carried out. The reader transmits a command periodically to the sensor tag while both units are aligned to each other (line



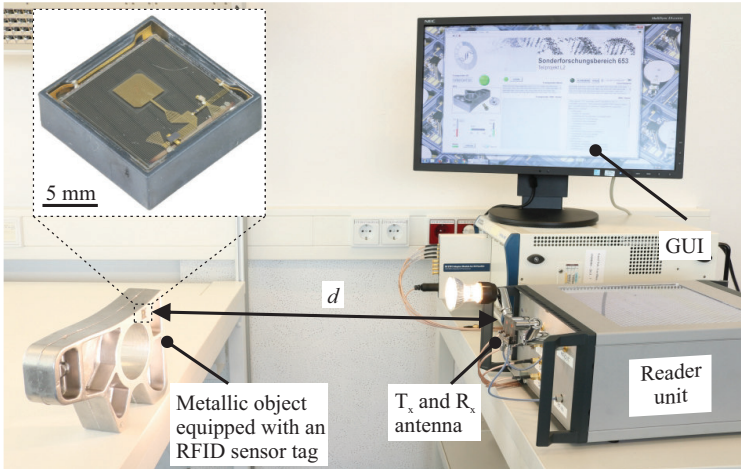


Figure 5.27 Photograph of the measurement setup for the determination of the maximum communication distance  $d$ . [QHD1]

of sight). Then these units are moved away from each other gradually. If the command is detected correctly by the MCU it generates a response signal which is monitored by an oscilloscope. In doing so the received command can be proved. The measurements are carried out with ten fabricated RFID sensor tags (within a laboratory environment) and it is observed that at a distance greater than  $d_{T, \max} = 1.26 \text{ m} (\pm 0.1 \text{ m or } \pm 8 \%)$  the sensor tag is not able to detect the command correctly. By knowing the maximum distance  $d_{T, \max}$ , the transmitted power (EIRP) of the reader  $P_{\text{tx}} \cdot G_{\text{R}} = 21.5 \text{ dBm}$ , the antenna gain of the sensor tag  $G_{\text{Tag}} = 4.4 \text{ dBi}$ , the free space wavelength  $\lambda_0 = 12.5 \text{ mm}$  and the input reflection coefficient  $|\Gamma_2| = -31 \text{ dB}$  the minimum detectable input power of the sensor tag can be determined approximately using the Friis transmission formula [15] (assumption: no multipath propagation):

$$P_{\text{Tag, min}} = P_{\text{tx}} G_{\text{R}} G_{\text{Tag}} \left( \frac{\lambda_0}{4\pi d_{\max}} \right)^2 (1 - |\Gamma_2|^2). \quad (5.2)$$

Hence, the sensitivity of the RFID sensor tag is  $P_{\text{Tag, min}} \approx -36 \text{ dBm}$ .

### 5.3.3 Conclusion

The main results of the measurement-based evaluation of the developed RFID system are:

- The sensitivity of the reader unit can be specified to  $P_{\text{Reader, min}} = -91$  dBm.
- The sensitivity of the tag is  $P_{\text{Tag, min}} \approx -36$  dBm.
- A comparison of the calculated maximum achievable communication distance of the reader unit  $d_{\text{R, max}} = 1.3$  m and the experimentally determined maximum communication range of the tag  $d_{\text{T, max}} = 1.26$  m ( $\pm 8\%$ ) shows that the maximum communication distance of the whole developed system can be given to  $d_{\text{max}} \approx 1.3$  m.

This work is a subproject of the Collaborative Research Centre 653 (CRC 653) entitled *Gentelligent Components in their Lifecycle - Utilization of inheritable component information in product engineering*. The CRC 653 has developed a fundamental approach for "Industry 4.0" compliant cross-linked production. One vision is to eliminate the separation between mechanical parts and their related information carrier. The requirements for a wireless communication module are such as: identifiability, integrability on/in objects and capability to collect, process and store data during the lifecycle of a mechanical part. There are no commercial RFID tags that can fulfill these criteria. For this reason, a miniaturized self-sufficient RFID sensor tag was developed which can be integrated in metallic components. Research and technological challenges were the development and realization of the optically transparent antenna and analog front-end, the minimization of the power consumption as well as the assembly and interconnection technology. The realized RFID sensor tag, which is freely configurable via software, is able to store sensor data as well as component related data and to transmit them back to a reader unit.

In order to develop an RFID sensor tag, its design concept was first presented. The design approach considered the miniaturization aspect and the fusion of optical and electrical components. A three-dimensional molded interconnect device (3D-MID) was used as a housing and circuit carrier simultaneously. In this way, the number of parts can be reduced. For an efficient use of the mounting volume the patch antenna and the analog front-end is arranged on top of a solar cell. Thus, one of the most challenging tasks was to design these RF components with the highest possible optical transparency. However, the RF properties were always considered.

Investigations on optically transparent and electrically conductive materials such as Indium Tin Oxide (ITO) and silver nanowires (AgNWs) were carried out by simulations and measurements. Their electrical conductivity is too poor, meaning that a patch antenna consisting of AgNWs only has a radiation efficiency of less than 10 % at 50 % transparency [QHD2]. Therefore, grid line structures made of metal were studied, as they can provide both high optical transparency and good conductivity. Different grid line width and spacing

between the grid structure were investigated regarding the RF properties. The knowledge obtained was used to simplify the design step from a conventional discrete circuit to a circuit with grid structures.

The influence of the grid lines on the antenna characteristics was also studied using a 3D electromagnetic simulation software. Compared to a conventional, non-transparent patch antenna, meshing the patch antenna results in a decrease of the resonance frequency, the gain, the radiation efficiency, the front-to-back ratio and the antenna impedance. Furthermore, the utilized solar cell arranged underneath also causes an impact on the antenna properties. By means of a measurement setup the solar cell has been characterized and a corresponding simulation model has been derived. This allows the previously defined antenna characteristics to be configured. The peak realized gain is 4.4 dBi, the axial ratio is lower than 2 dB and the radiation efficiency can be given with a value of 49 %.

For a bidirectional communication between a reader and a sensor tag, the need of an analog front-end is essential. Because of the operating frequency of 24 GHz and due to the fact that the power supply is restricted, only a small number of components is commercially available. Therefore, suitable RF components were initially chosen. A transistor was used as a switch in a common source configuration in order to generate a backscattered amplitude modulated signal. For a demodulation of the received signal, a half-wave envelope demodulator based on a Schottky diode was utilized. In order to verify the simulated results, an analog front-end made of grid line structure was fabricated and characterized. A good agreement was achieved. In the second step, the analog front-end was designed with a reference impedance of  $Z_{\text{ref}} = 30 \Omega$  to achieve a simple and compact impedance matching network. Therefore, a non-transparent modulator and demodulator circuit was designed and optimized. Afterwards, the design rules derived from the investigation of meshed microstrip lines were applied to this circuit in order to obtain an optically transparent analog front-end. This unit requires an average power consumption of 3.2  $\mu\text{W}$ .

Both the meshed antenna and analog front-end were interconnected and realized on a quartz glass with a dimension of 10.7 mm  $\times$  10.82 mm. This total area was mainly determined by the size of the solar cell. The overall optical transparency of the RF units can be specified as approx. 75 %.

A further part of the tag is the baseband unit with the data processing unit. The criteria of component size, functional scope and power consumption were taken into account when selecting the components. The chosen microcontroller (MCU) includes a nonvolatile memory, a temperature sensor and a comparator unit. Due to the limited power supply, a detailed analysis of the power consumption of the

MCU was carried out. Depending on the operating mode of the MCU the power consumption varies between  $58 \mu\text{W}$  and  $1.85 \text{mW}$  at a supply voltage of  $V_{cc} = 2 \text{V}$ . The tag's energy harvesting concept is based on a highly efficient solar cell combined with an energy storage that guarantees an autonomous functionality. In daylight, the solar cell provides sufficient energy to supply the sensor tag. The portion of the non-consumed energy is stored in a supercapacitor. In this way, an operation of the sensor tag in low light environments is still possible for approx. 13 minutes (periodic data transmission, every second). All components of the digital unit were soldered on a three-dimensional interconnect device (3D-MID) with an overall size of  $13.3 \text{mm} \times 12.9 \text{mm} \times 4.15 \text{mm}$ .

In addition to the developed RFID sensor tag, a reader unit was needed for the evaluation of the tag and the use within the Collaborative Research Centre. Since no commercial 24 GHz RFID reader were available, a reader unit was developed within this work. For the realization of the analog unit, both commercial and self-developed components were used. Thus, a flexible configuration of the RF properties was possible. Furthermore, a graphical user interface (GUI) based on LabVIEW was implemented in order to control and evaluate the data exchange between reader and tag. The sensitivity of the reader unit and the sensor tag was determined to  $P_{\text{Reader, min}} = -91 \text{dBm}$  and  $P_{\text{Tag, min}} \approx -36 \text{dBm}$ , respectively. The achieved maximum communication range between the tag and the reader is approximately  $d_{\text{max}} \approx 1.3 \text{m}$ . The key characteristics of the tag are summarized in Table 6.1.

Within this work, a small series of approx. 100 RFID sensor tags was fabricated. These sensor tags can be flexibly used in numerous applications e.g. in the field of "Industry 4.0" [96].

Antenna	Condition	Value
Input reflection coefficient	24 GHz	< -20 dB
Peak realized gain	24 GHz	4.4 dBi
Half power beam width	24 GHz E-plane, H-plane	78°
Axial ratio	24 GHz	< 2 dB
Radiation efficiency	24 GHz	49 %

RF Circuit	Condition	Value
Input reflection coefficient $ \Gamma_1 $	Mismatched state	$\sim -3$ dB
Input reflection coefficient $ \Gamma_2 $	Matched state	$\sim -31$ dB
Power consumption	$V_{GS} = 0.7$ V	6.37 $\mu$ W

RFID Sensor Tag	Condition	Value
Communication range $d_{max}$	Maximum	$\sim 1.3$ m
Sensitivity $P_{Tag, min}$	Minimum	-36 dBm
Data rate	3 MHz MCU clock	80 kbit/s
Power consumption	$V_{cc} = 2$ V	min. 58 $\mu$ W max 1.85 mW
Operation time in low light environments	Periodic data transmission, every second	$\sim 13$ minutes
Optical transparency	Antenna and analog front-end	75 %
Overall size	Length	13.3 mm
	Width	12.9 mm
	Height	4.15 mm

Table 6.1 Main characteristics of the developed 24 GHz RFID sensor tag.

## Bibliography

- [1] A. Zanella, N. Bui, A. Castellani, L. Vangelista, and M. Zorzi, “Internet of things for smart cities,” *IEEE Internet of Things Journal*, vol. 1, no. 1, pp. 22–32, 2014.
- [2] M. Wollschlaeger, T. Sauter, and J. Jasperneite, “The future of industrial communication: Automation networks in the era of the internet of things and industry 4.0,” *IEEE Internet of Things Journal*, vol. 11, no. 1, pp. 17–27, 2017.
- [3] K. Finkenzerler, *RFID Handbook*, 3rd ed. John Wiley & Sons, Ltd, 2010.
- [4] “Digitalization of castings,” Fraunhofer IFAM, accessed Mar. 2020. [Online]. Available: [https://www.ifam.fraunhofer.de/en/Profile/Locations/Bremen/Shaping\\_Functional\\_Materials/Casting\\_Technology/castronics-digitalization-castings.html](https://www.ifam.fraunhofer.de/en/Profile/Locations/Bremen/Shaping_Functional_Materials/Casting_Technology/castronics-digitalization-castings.html)
- [5] C. Swedberg, “Rfid-reading drone tracks structural steel products in storage yard,” online, Sept. 2014, accessed Mar. 2020. [Online]. Available: <https://www.rfidjournal.com/articles/view?12209>
- [6] —, “Thyssenkrupp steel europe tracks its tools,” online, June 2012, accessed Mar. 2020. [Online]. Available: <https://www.rfidjournal.com/articles/view?9620>
- [7] M. Gillmann, “Rfid for medical device and surgical instrument tracking,” online, Sept. 2018, accessed Mar. 2020. [Online]. Available: <https://www.medicaldesignbriefs.com/component/content/article/mdb/features/articles/32814>
- [8] Omni-id.com, Aug. 2019, accessed Aug. 2019. [Online]. Available: [https://www.omni-id.com/pdfs/Omni-ID\\_Featured\\_Comparison\\_Guide.pdf](https://www.omni-id.com/pdfs/Omni-ID_Featured_Comparison_Guide.pdf)
- [9] Neosid.de, accessed Apr. 2020. [Online]. Available: <https://neosid.de/produkte/rfid-tags/>

- [10] xerafy.com, accessed Aug. 2019. [Online]. Available: <https://www.xerafy.com/userfiles/uploads/brochures/xerafy-tags-labels-product-guide-en-20190220.pdf>
- [11] B. Denkena, T. Mörke, M. Krüger, J. Schmidt, H. Boujnah, J. Meyer, P. Gottwald, B. Spitschan, and M. Winkens, “Development and first applications of gentelligent components over their lifecycle,” *CIRP Journal of Manufacturing Science and Technology*, vol. 7, no. 2, pp. 139–150, 2014. [Online]. Available: <http://www.sciencedirect.com/science/article/pii/S1755581713000850>
- [12] B. Denkena, *Die vernetzte Produktion: Forschungsergebnisse für die Praxis*, 1st ed. TEWISS, 2015.
- [13] “Collaborative research centre 653,” online, accessed Apr. 2020. [Online]. Available: <https://www.sfb653.uni-hannover.de/sfb653.html?&L=1>
- [14] E. B. Kaldjob, “Design and analysis of field-powered transponders integrated in metallic objects,” Ph.D. dissertation, University of Hannover, Hannover, Juni 2010.
- [15] H. T. Friis, “A note on a simple transmission formula,” *Proceedings of the IRE*, vol. 34, no. 5, pp. 254–256, 1946.
- [16] J. Meyer, “Ein optisch versorgter rfid-transponder für die integration in metall,” Ph.D. dissertation, Leibniz Universität Hannover, 2015.
- [17] H. Dagan, A. Shapira, A. Teman, A. Mordakhay, S. Jameson, E. Pikhay, V. Dayan, Y. Roizin, E. Socher, and A. Fish, “A low-power low-cost 24 GHz RFID tag with a c-flash based embedded memory,” *IEEE Journal of Solid-State Circuits*, vol. 49, no. 9, pp. 1942–1957, 2014.
- [18] S. Lischer, M. Heiss, M. Landwehr, and W. J. Fischer, “A 24 GHz RFID system-on-a-chip with on-chip antenna, compatible to ISO 18000-6c / EPC c1g2,” in *2015 IEEE International Conference on Microwaves, Communications, Antennas and Electronic Systems (COMCAS)*, 2015, pp. 1–4.
- [19] SMARTRAC TECHNOLOGY GmbH, “Abschlussbericht zum teilvorhaben 24-ghz-rfid-label / tag im verbundprojekt innoprofile-transferverbundprojekt 24 ghz millimeter wave identifikation (mmid) hf- und



- mikrowellentransponder : Projektlaufzeit: 01.10.2012-30.09.2015,” 2016. [Online]. Available: <https://doi.org/10.2314/GBV:870120719>
- [20] Bundesnetzagentur. [Online]. Available: <https://www.bundesnetzagentur.de/EN/Areas/Telecommunications/telecommunications-node.html>
- [21] —, “Frequenzplan gemäss § 54 tkg über die aufteilung des frequenzbereichs von 0 khz bis 3000 ghz auf die frequenznutzungen sowie über die festlegungen für diese frequenznutzungen,” accessed Mar. 2019. [Online]. Available: <https://www.bundesnetzagentur.de/>
- [22] C. A. Balanis, *Antenna Theory*, 3rd ed. John Wiley & Sons, 2005.
- [23] J. Franke, “Three-dimensional molded interconnect devices (3d-MID).” Hanser, 2014, DOI: 10.3139/9781569905524.fm.
- [24] Spectrolab, “C3mj+ improved third generation cpv technology,” Data sheet, 2011.
- [25] D. S. Ginley, *Handbook of Transparent Conductors*. Springer, Boston, MA, 2011.
- [26] Z. L. Wang, Ed., *Nanowires and Nanobelts: Materials, Properties and Devices*. Springer, 2003, vol. Volume 1: Metal and Semiconductor Nanowires.
- [27] D. Langley, G. Giusti, C. Mayousse, C. Celle, D. Bellet, and J.-P. Simonato, “Flexible transparent conductive materials based on silver nanowire networks: a review,” *Nanotechnology*, vol. 24, no. 45, p. 452001, 2013. [Online]. Available: <http://stacks.iop.org/0957-4484/24/i=45/a=452001>
- [28] I. V. Anoshkin, I. I. Nefedova, I. S. Nefedov, D. V. Lioubtchenko, A. G. Nasibulin, and A. V. Räsänen, “Resistivity and optical transmittance dependence on length and diameter of nanowires in silver nanowire layers in application to transparent conductive coatings,” *IET Micro Nano Letters*, vol. 11, no. 7, pp. 343–347, 2016.
- [29] J. A. Spechler, “Laser Processed Silver Nanowire Network Transparent Electrodes for Novel Electronic Devices,” 2016. [Online]. Available: <http://dataspace.princeton.edu/jspui/handle/88435/dsp013x816q020>

- [30] “Ras ag materials + technologies ECOS HC,” Data sheet, accessed Sep. 2017. [Online]. Available: <http://ras-ag.com/ecos-hc/3/>
- [31] F. M. Smits, “Measurement of sheet resistivities with the four-point probe,” *The Bell System Technical Journal*, vol. 37, no. 3, pp. 711–718, May 1958.
- [32] D. F. Williams, J. C. M. Wang, and U. Arz, “An optimal vector-network-analyzer calibration algorithm,” *IEEE Transactions on Microwave Theory and Techniques*, vol. 51, no. 12, pp. 2391–2401, 2003.
- [33] J. Hautcoeur, X. Castel, F. Colombel, R. Benzerga, M. Himdi, G. Legeay, and E. Motta-Cruz, “Transparency and electrical properties of meshed metal films,” *Thin Solid Films*, vol. 519, no. 11, pp. 3851–3858, 2011. [Online]. Available: <http://www.sciencedirect.com/science/article/pii/S0040609011003257>
- [34] G. Clasen and R. Langley, “Meshed patch antennas,” *IEEE Transactions on Antennas and Propagation*, vol. 52, no. 6, pp. 1412–1416, 2004.
- [35] J. Hautcoeur, L. Talbi, K. Hettak, and M. Nedil, “60 GHz optically transparent microstrip antenna made of meshed AuGL material,” *Antennas Propagation IET Microwaves*, vol. 8, no. 13, pp. 1091–1096, 2014.
- [36] T. Yasin and R. Baktur, “Circularly polarized meshed patch antenna for small satellite application,” *IEEE Antennas and Wireless Propagation Letters*, vol. 12, pp. 1057–1060, 2013.
- [37] B. J. Rubin and H. L. Bertoni, “Waves guided by conductive strips above a periodically perforated ground plane,” *IEEE Transactions on Microwave Theory and Techniques*, vol. 31, no. 7, pp. 541–549, 1983.
- [38] A. C. Cangellaris, M. Gribbons, and J. L. Prince, “Electrical characteristics of multichip module interconnects with perforated reference planes,” *IEEE Transactions on Components, Hybrids, and Manufacturing Technology*, vol. 16, no. 1, pp. 113–118, 1993.
- [39] P. Bernardi, R. Cicchetti, and A. Faraone, “A full-wave characterization of an interconnecting line printed on a dielectric slab backed by a gridded ground plane,” *IEEE Transactions on Electromagnetic Compatibility*, vol. 38, no. 3, pp. 237–243, 1996.

- [40] Y. L. Li, D. G. Figueroa, S. Zhong, L. M. Nguyen, T. Nguyen, L. A. Polka, and J. C. Liao, "Theoretical and experimental approach for model extraction of multiconductor interconnects with multiple meshed planes on an APCB," in *1998 Proceedings. 48th Electronic Components and Technology Conference (Cat. No.98CH36206)*, 1998, pp. 1061–1067.
- [41] A. W. Mathis and A. F. Peterson, "Full-wave electromagnetic modeling of interconnects with meshed ground planes," in *IEEE 7th Topical Meeting on Electrical Performance of Electronic Packaging (Cat. No.98TH8370)*, 1998, pp. 136–139.
- [42] S. Wu, H. Shi, M. Herndon, B. Cornelius, M. Halligan, and J. Fan, "Modeling and analysis of a trace referenced to a meshed ground plane," in *2011 IEEE International Symposium on Electromagnetic Compatibility*, 2011, pp. 137–141.
- [43] M. Kahrizi, T. K. Sarkar, and Z. A. Maricevic, "Dynamic analysis of a microstrip line over a perforated ground plane," *IEEE Transactions on Microwave Theory and Techniques*, vol. 42, no. 5, pp. 820–825, 1994.
- [44] W. Y. Tam and Y. Chen, "Analysis of microstrip lines on a perforated ground using reciprocity method," in *Proceedings of 1997 Asia-Pacific Microwave Conference*, vol. 1, 1997, pp. 425–428 vol.1.
- [45] Y. L. Chow, T. K. Sarkar, and K. L. Wan, "CAD formulas of microstrip line with perforated ground plane by synthetic asymptote," in *2000 Asia-Pacific Microwave Conference. Proceedings (Cat. No.00TH8522)*, 2000, pp. 286–289.
- [46] T. Maleszka, M. Preisner, and P. Kabacik, "Meshed ground plane structures for textile antennas," in *2009 3rd European Conference on Antennas and Propagation*, 2009, pp. 713–717.
- [47] O. Shimada, K. Ito, T. Miyagi, S. Kimijima, and T. Sudo, "Electrical properties of a multilayer thin film substrate for multichip packages," in *Proceedings. Japan IEMT Symposium, Sixth IEEE/CHMT International Electronic Manufacturing Technology Symposium*, 1989, pp. 121–127.
- [48] R. Senthinathan, W. E. Pence, N. Raver, and J. L. Prince, "Signal propagation over perforated reference planes in stripline interconnect structures,"

- in *1992 Proceedings 42nd Electronic Components Technology Conference*, 1992, pp. 717–724.
- [49] C.-P. Chien, A. F. Burnett, J. M. Cech, and M. H. Tanielian, “The signal transmission characteristics of embedded microstrip transmission lines over a meshed ground plane in copper/polyimide multichip module,” *IEEE Transactions on Components, Packaging, and Manufacturing Technology: Part B*, vol. 17, no. 4, pp. 578–583, 1994.
- [50] L. Zhu and K. L. Melde, “Characterization of microstrip interconnects over gridded ground planes,” in *IEEE 14th Topical Meeting on Electrical Performance of Electronic Packaging, 2005.*, 2005, pp. 75–78.
- [51] Y. Yun, K. S. Lee, C. R. Kim, K. M. Kim, and J. W. Jung, “Basic RF characteristics of the microstrip line employing periodically perforated ground metal and its application to highly miniaturized on-chip passive components on GaAs MMIC,” *IEEE Transactions on Microwave Theory and Techniques*, vol. 54, no. 10, pp. 3805–3817, 2006.
- [52] D. Packiaraj, M. Ramesh, A. T. Kalghatgi, and K. J. Vinoy, “Analysis of modified microstrip line and its application,” in *2012 National Conference on Communications (NCC)*, 2012, pp. 1–4.
- [53] G.-A. Lee, H.-Y. Lee, and F. D. Flaviis, “Perforated microstrip structure for miniaturising microwave devices,” *Electronics Letters*, vol. 38, no. 15, pp. 800–801, 2002.
- [54] J. Hautcoeur, L. Talbi, and K. Hettak, “Feasibility study of optically transparent CPW-fed monopole antenna at 60-GHz ISM bands,” *IEEE Transactions on Antennas and Propagation*, vol. 61, no. 4, pp. 1651–1657, 2013.
- [55] Q. Weng, X. Li, C. Lu, C. K. C. Tzuang, and H. S. Wu, “The complex mode formation in propagating microstrip of two-dimensional perforation,” in *2015 International Workshop on Electromagnetics: Applications and Student Innovation Competition (iWEM)*, 2015, pp. 1–2.
- [56] T. C. Edwards and M. B. Steer, *Foundations for Microstrip Circuit Design*, 4th ed. Wiley, 2016.

- [57] I. J. Bahl and R. Garg, "Simple and accurate formulas for a microstrip with finite strip thickness," *Proceedings of the IEEE*, vol. 65, no. 11, pp. 1611–1612, Nov. 1977.
- [58] G. L. Ragan, Ed., *Microwave Transmission Circuits*. Dover Publications Inc., 1965, pp. 32-33.
- [59] J. A. Reynoso-Hernandez, "Unified method for determining the complex propagation constant of reflecting and nonreflecting transmission lines," *IEEE Microwave and Wireless Components Letters*, vol. 13, no. 8, pp. 351–353, Aug. 2003.
- [60] J. E. Zuniga-Juarez, J. A. Reynoso-Hernandez, M. d. C. Maya-Sanchez, and R. S. Murphy-Arteaga, "A New Analytical Method to Calculate the Characteristic Impedance  $Z_c$  of Uniform Transmission Lines," *Computacion y Sistemas*, vol. 16, no. 3, pp. 277–285, 2012.
- [61] Damaskos, accessed Jan. 2019. [Online]. Available: <http://www.damaskosinc.com/cavity.htm>
- [62] R. Caso, A. D'Alessandro, A. Michel, and P. Nepa, "Integration of slot antennas in commercial photovoltaic panels for stand-alone communication systems," *Antennas and Propagation, IEEE Transactions on*, vol. 61, no. 1, pp. 62–69, 2013.
- [63] S. Vaccaro, P. Torres, J. Mosig, A. Shah, J.-F. Ziȳrcher, A. Skrivervik, F. Gardiol, P. de Maagt, and L. Gerlach, "Integrated solar panel antennas," *Electronics Letters*, vol. 36, no. 5, pp. 390–391, 2000.
- [64] S. Vaccaro, J. Mosig, and P. de Maagt, "Two advanced solar antenna solant designs for satellite and terrestrial communications," *Antennas and Propagation, IEEE Transactions on*, vol. 51, no. 8, pp. 2028–2034, 2003.
- [65] S. V. Shynu, M.-J. Roo Ons, M. Ammann, S. McCormack, and B. Norton, "Dual band a-si:h solar-slot antenna for 2.4/5.2ghz wlan applications," in *Antennas and Propagation, 2009. EuCAP 2009. 3rd European Conference on*, 2009, pp. 408–410.
- [66] N. Henze, A. Giere, H. Fruchting, and P. Hofmann, "Gps patch antenna with photovoltaic solar cells for vehicular applications," in *Vehicular Technology Conference, 2003. VTC 2003-Fall. 2003 IEEE 58th*, vol. 1, 2003, pp. 50–54 Vol.1.

- [67] T. W. Turpin and R. Baktur, "Meshed patch antennas integrated on solar cells," *IEEE Antennas and Wireless Propagation Letters*, vol. 8, pp. 693–696, 2009.
- [68] M. J. Roo-Ons, S. V. Shynu, M. J. Ammann, S. J. McCormack, and B. Norton, "Transparent patch antenna on a-si thin-film glass solar module," vol. 47, no. 2, pp. 85–86, 2011.
- [69] T. Yasin, "Transparent antennas for solar cell integration," Ph.D. dissertation, Utah State University, Logan, Utah, 2013.
- [70] G. Clasen and R. J. Langley, "Patch antennas constructed from meshes," in *IEEE Antennas and Propagation Society International Symposium. 1999 Digest. Held in conjunction with: USNC/URSI National Radio Science Meeting (Cat. No.99CH37010)*, vol. 4, July 1999, pp. 2638–2641 vol.4.
- [71] C. A. Balanis, *Advanced Engineering Electromagnetics*, 2nd ed. John Wiley & Sons, 2012.
- [72] P. Sharma and K. Gupta, "Analysis and optimized design of single feed circularly polarized microstrip antennas," *IEEE Transactions on Antennas and Propagation*, vol. 31, no. 6, pp. 949–955, 1983.
- [73] T. Shahvirdi and R. Baktur, "Analysis of the effect of solar cells on the antenna integrated on top of their cover glass," in *2015 IEEE International Symposium on Antennas and Propagation USNC/URSI National Radio Science Meeting*, 2015, pp. 2429–2430.
- [74] H. Lehpamer, *RFID Design Principles*. Artech House, 2008.
- [75] P. Pursula, T. Vähä-Heikkilä, A. Müller, D. Neculoiu, G. Konstantinidis, A. Oja, and J. Tuovinen, "Millimeter-wave identification - a new short-range radio system for low-power high data-rate applications," *Microwave Theory and Techniques, IEEE Transactions on*, vol. 56, no. 10, pp. 2221–2228, 2008.
- [76] "VMMK-1225," Avago Technologies, accessed Feb. 2012. [Online]. Available: <http://www.avagotech.com/>
- [77] J. Dickson, "On-chip high-voltage generation in mnos integrated circuits using an improved voltage multiplier technique," *Solid-State Circuits, IEEE Journal of*, vol. 11, no. 3, pp. 374–378, 1976.

- [78] J. Cockroft and T. Walton, "Production of high velocity positive ions," *Proceedings of the Royal Society*, vol. 136, pp. 619–630, 1932.
- [79] "HSMS-285x series," Avago Technologies, accessed Apr. 2020. [Online]. Available: <https://docs.broadcom.com/doc/AV02-1377EN>
- [80] "HSCH-9161," Avago Technologies, Nov. 2013, accessed Apr. 2020. [Online]. Available: <https://www.keysight.com/en/pd-1066301-pn-HSCH-9161/millimeter-wave-zero-bias-gaas-schottky-diode?cc=DE&lc=ger>
- [81] "Skd-vdi-f1ch-002," Virginia Diodes Inc., 2012. [Online]. Available: [www.modelithics.com](http://www.modelithics.com)
- [82] P. V. Nikitin, K. V. S. Rao, and R. D. Martinez, "Differential RCS of RFID tag," *Electronics Letters*, vol. 43, no. 8, pp. 431–432, 2007.
- [83] "Quartz wafer," Plan Optik AG, accessed Aug. 2019. [Online]. Available: <https://www.planoptik.com/en/products/quartz-wafers.html>
- [84] "Opticstudio," Zemax, accessed Aug. 2019. [Online]. Available: <https://www.zemax.com/products/opticstudio>
- [85] "Opticstudio knowledgebase," Zemax, accessed Aug. 2019. [Online]. Available: <https://customers.zemax.com/os/resources/learn/knowledgebase>
- [86] "Msp430fr5738," Data sheet, Texas Instruments, accessed Aug. 2019. [Online]. Available: <http://www.ti.com/product/MSP430FR5738>
- [87] "Bma280," Data sheet, Bosch Sensortec, accessed Aug. 2019. [Online]. Available: [https://ae-bst.resource.bosch.com/media/{\}\\_tech/media/datasheets/BST-BMA280-DS000.pdf](https://ae-bst.resource.bosch.com/media/{\}_tech/media/datasheets/BST-BMA280-DS000.pdf)
- [88] "LMV7271," Texas Instruments, Februar 2013. [Online]. Available: <http://www.ti.com/>
- [89] J. H. Ermer, R. K. Jones, P. Hebert, P. Pien, R. R. King, D. Bhusari, R. Brandt, O. Al-Taher, C. Fetzer, G. S. Kinsey, and N. Karam, "Status of c3mj+ and c4mj production concentrator solar cells at spectrolab," *Electronics Letters*, vol. 2, no. 2, pp. 209–213, 2012.
- [90] "Qth10(/m) quartz tungsten-halogen lamp," Data sheet, Thorlabs, Aug. 2015, rev C.

- [91] A. H. Himanshu Sharma and Z. A. Jaffery, "Solar energy harvesting wireless sensor network nodes: A survey," *Journal of Renewable and Sustainable Energy*, vol. 10, no. 2, Feb. 2018. [Online]. Available: <https://aip.scitation.org/doi/10.1063/1.5006619>
- [92] "bq25505," Data sheet, Texas Instruments, accessed Mar. 2019. [Online]. Available: <http://www.ti.com/lit/ds/symlink/bq25505.pdf>
- [93] "bat30f4," Data sheet, STMicroelectronics, accessed Sep. 2018. [Online]. Available: <https://www.st.com/resource/en/datasheet/bat30f4.pdf>
- [94] "K-MC1 Radar Transceiver," RFbeam Microwave GmbH, accessed Jan. 2013. [Online]. Available: <http://www.rfbeam.ch/>
- [95] "24 ghz mmic iq receiver rx-024-04," Data sheet, SiliconRadar, 2013.
- [96] B. Denkena and T. Mörke, Eds., *Cyber-Physical and Intelligent Systems in Manufacturing and Life Cycle*. Elsevier, 2017. [Online]. Available: <https://linkinghub.elsevier.com/retrieve/pii/C20160003741>



# Curriculum Vitae

## Personal Details

Name	Đào, Quang Huy
Date of Birth	27 <sup>th</sup> November, 1984 in Thái Nguyên, Vietnam
Nationality	German

## Education

2006	<i>Abitur</i> at Bismarckschule Hannover, Germany
2006–2011	Study of electrical engineering at the Leibniz Universität Hannover, Germany graduating as <i>Dipl.-Ing.</i>
2012–2017	Research assistant and Ph.D. student at Institute of Microwave and Wireless Systems, Leibniz Universität Hannover, Germany
2018–2021	Ph.D. student at Institute of Microwave and Wireless Systems, Leibniz Universität Hannover, Germany